Fast-Ion Transport and Acceleration Induced by Edge Localized Modes in MAST Upgrade and ASDEX Upgrade

Author

Juan Francisco Rivero Rodríguez

Supervisors

Daniel García Vallejo
Manuel García Muñoz

A thesis presented for the degree of
Doctor of Philosophy

Departamento de Ingeniería Mecánica y Fabricación
Universidad de Sevilla
Spain

June 22, 2021

Declaration of Authorship

I, Juan Francisco Rivero Rodríguez, declare that this thesis titled, *Fast-Ion Transport and Acceleration Induced by Edge Localized Modes in MAST Upgrade and ASDEX Upgrade* and the work presented in it are my own. I confirm that:

- This work was done wholly or mainly while in candidature for a research degree at this University.
- Where any part of this thesis has previously been submitted for a degree or any other qualification at this University or any other institution, this has been clearly stated.
- Where I have consulted the published work of others, this is always clearly attributed.
- Where I have quoted from the work of others, the source is always given. With the exception of such quotations, this thesis is entirely my own work.
- I have acknowledged all main sources of help.
- Where the thesis is based on work done by myself jointly with others, I have made clear exactly what was done by others and what I have contributed myself.

A mi madre,
que me ha dado la vida
y la fuerza.

Abstract

Fusion energy promises sustainable, low-emission, baseload power to the grid. The tokamak is the most advanced device to achieve fusion energy and it is approaching operation under power-plant conditions. Nowadays tokamaks aim to resolve the scientific and technical challenges of future power plants. In tokamaks, fast ions, – i.e., ions above the bulk plasma energy –, are employed to raise the plasma temperature up to fusion relevant energies. Fast ions may lose confinement due to the interaction with electromagnetic perturbations of different nature, posing a risk to the plasma performance and endangering the tokamak integrity. In the tokamak high confinement operation mode, known as H-mode, an explosive and repetitive magneto-hydro dynamic (MHD) instability is driven in the plasma edge, known as Edge Localized Mode (ELM). ELMs release a great amount of energy and particles to the tokamak wall that are believed to be intolerable in future devices. Besides, recent experiments in the ASDEX Upgrade tokamak have observed an increase of fast-ion losses above their injection energy, correlated with the ELM activity. The observations suggest an interaction between the ELMs and the fast ions that results in the acceleration and loss of the latter.

This work aims to study the fast-ion losses induced by ELMs. The thesis have covered the development of numerical tools and design of diagnostics to achieve this goal. Numerically, the implementation of time-evolving 3D electromagnetic perturbations in full-orbit codes, like ASCOT5, have made it possible to investigate the main transport and acceleration mechanisms suggested by the ELM-induced fast-ion losses. Experimentally, the first FILD for the MAST-U spherical tokamak was designed and installed in this thesis. The design includes a rotary and reciprocating mechanism that enables the adaptation of the FILD probe to different orientations [0°, 90°] and radial positions [1.40 m, 1.60 m]. The first MAST-U FILD data was expected during this thesis. However, due to several delays in the MAST-U experiments, the diagnostic has not been put in operation yet. For this reason, the experimental and the numerical plans have followed different paths. The experiments, carried out in the ASDEX Upgrade tokamak, have aimed to

expand the scope of the observations of ELM-induced fast-ion losses, performing new scans that would reveal the dominant parameters that affect the interaction between the fast ions and the ELMs. The modelling seeks to understand the transport and acceleration mechanism by first principle modelling and to reproduce the main experimental observations in ASDEX Upgrade. The modelling in MAST-U has also made it possible to reproduce the foreseen FILD signal and enabled comparisons between MAST-U and ASDEX Upgrade.

Resumen

La fusión nuclear se esboza como una fuente de energía sostenible, de bajas emisiones y que aportará potencia de base al mix eléctrico. Los tokamaks son los dispositivos más avanzados para la obtención de energía mediante fusión nuclear y operan en condiciones cercanas a las de las futuras centrales nucleares. Hoy en día, los tokamaks existentes tienen como objetivo resolver los desafíos científicos y técnicos que plantean las futuras plantas de fusión nuclear. En los tokamaks, los iones rápidos, – aquellos iones cuya energía es superior a la del resto del volumen de plasma –, se emplean para aumentar la temperatura del plasma hasta energías donde la fusión se hace patente. Los iones rápidos pueden perder el confinamiento debido a interacciones con perturbaciones electromagnéticas de diversa naturaleza, siendo esto un riesgo para el rendimiento del plasma y para la integridad del reactor. En el modo de operación de alto confinamiento, conocido por H-mode, aparecen de forma repetitiva inestabilidades magnetohidrodinámicas (MHD) explosivas localizadas en el borde, conocidas como Edge Localized Modes (ELMs). Los ELMs liberan una gran cantidad de energía y momento hacia las paredes del plasma, cuyo efecto se estima intolerable en futuros tokamaks. Además, investigaciones recientes en el tokamak ASDEX Upgrade han observado un aumento en las pérdidas de iones rápidos a energías por encima de su energía de inyección, que aparecen relacionadas con la actividad de los ELMs. Estas observaciones sugieren que existe una interacción entre los ELMs y los iones rápidos, que resulta en la aceleración y pérdida de estos últimos.

Este trabajo tiene como objetivo de estudio las pérdidas de iones rápidos inducidos por ELMs. Para conseguir este objetivo, la tesis ha abarcado el desarrollo de herramientas numéricas y el diseño de diagnósticos experimentales. En el aspecto numérico, se han utilizado códigos de seguimiento de órbitas como ASCOT5 y se han implementado perturbaciones electromagnéticas 3D que evolucionan en el tiempo. Esto ha permitido investigar los principales mecanismos de transporte y aceleración planteados para esclarecer la pérdida de iones rápidos inducida por ELMs. En el ámbito ex-

perimental, durante esta tesis se ha diseñado el primer detector de pérdidas de iones rápidos (FILD) en el tokamak esférico MAST-U. El diagnóstico está montado sobre un mecanismo de rotación y traslación que permite adaptar la sonda a diferentes orientaciones [0°, 90°] y posiciones radiales [1.40 m, 1.60 m]. Los primeros datos experimentales del FILD de MAST-U se esperaban obtener a lo largo de esta tesis. Sin embargo, distintos retrasos en el comienzo de la campaña experimental de MAST-U han impedido poner el diagnóstico en funcionamiento. Por este motivo, los planes experimentales y numéricos han tenido que seguir distintos planteamientos. Los experimentos, que se han realizado en ASDEX Upgrade, han tenido como objetivo expandir el alcance de las observaciones de pérdida de iones rápidos inducidas por ELMs, llevando a cabo nuevos rastreos para detectar los parámetros que más afectan en la interacción entre los iones rápidos y los ELMs. Con respecto al modelado, se busca realizar un modelado que permita reproducir las principales observaciones experimentales en ASDEX Upgrade y revele los mecanismos básicos de transporte y aceleración de iones rápidos durante los ELMs. Además, el modelado en MAST-U ha permitido preveer la señal de FILD, que se ha podido comparar con la señal en ASDEX Upgrade.

Contents

Chapter 1

Introduction

1.1 The Energy Transition

Over the last century, the energy consumption has raised dramatically to supply the needs of the modern society. No wonder, the human well-being has scaled up with the energy consumption, as it can be observed in figure 1.1. Nowadays, the world's main energy sources are based on burning fossil fuels – i.e., oil, gas and coal – due to their easy transformation into heat. However, this process adds greenhouse gases to the atmosphere, which is causing the Global Warming ($+1.5^\circ$ C since the preindustrial era [1]) and are related to more than 2 million premature human deaths each year [2]. For this reason, the transition to alternative energy sources with a reduced environmental footprint has become a major global issue in the past decades.

Although strong effort is being put in the development of clean renewable energies, like solar or wind, they are intermittent energy sources, meaning that the energy production cannot be controlled. This causes an imbalance in the consumed and produced energy, that needs to be solved by storing the excess and supply the deficiency with storage technologies, like batteries. Nonetheless, when the storage capacity is exceeded, solar and wind need the support of mass-producible energy sources or the energy supply will face shut-offs. Biomass is also considered a renewable energy source because it balances the emitted and collected CO_2, as it burns the trees that are previously growth. It solves the intermittence of solar and wind, but it does not eliminate all the harmful emissions and it poses an important risk to the Earth's biodiversity.

These days commercial nuclear energy (based on the fission of heavy atoms) is presented as a mass-producible energy source with no greenhouse

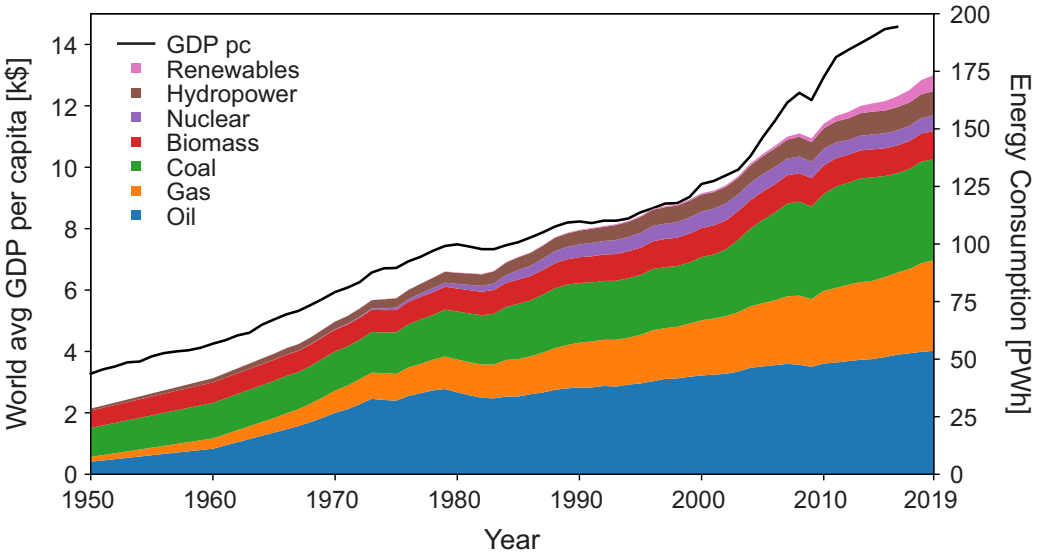

Figure 1.1: World's average Gross Domestic Product (GDP) per capita [3] and annual energy consumption, stacked by energy sources [4].

gas emissions. Nonetheless, the generation of long-lived radioactive wastes, the intrinsic instability of the fission chain reaction and the ill-famed accidents of Chernobyl [5] and Fukushima [6] have acquainted this energy source with a strong rejection over the population.

Even though the existing technologies are helping to mitigate the effects of Global Warming, it is clear that the society must come up with a safe, inexhaustible, mass-producible and clean energy source. Nuclear fusion is considered a key candidate to meet the needs.

1.2 Thermonuclear Fusion

Nuclear fusion is one of the most promising future energy sources. It is based on the energy released when two light atoms combine, producing a heavier element with a lower binding energy than those of the nuclei involved. Nuclear fusion naturally occurs in stars, such as the Sun. On Earth, the most plausible fusion reaction, due to its high cross-section [7], is:

$$D + T \rightarrow {}^{4}\mathrm{He} + n + 17.6\,\mathrm{MeV} \tag{1.1}$$

So-called D-T reaction, where two isotopes of hydrogen – i.e., deuterium (^{2}H, D) and tritium (^{3}H, T)[1] –, react releasing energy in the form of kinetic energy

[1]Hydrogen, ^{1}H, is also designated as H.

of the produced α-particle (3.5 MeV ^{4}He) and neutron (14.1 MeV n). Both deuterium and tritium are plentiful on Earth. The former can be extracted from the oceans water. The latter can be obtained with nuclear reactions from lithium, an abundant metal in the Earth's crust. Thus, nuclear fusion is considered a mass-producible inexhaustible energy source that would not produce greenhouse gases or long-lived radioactive waste.

To achieve fusion reactions, high energy is needed to overcome Coulomb repulsion against the nuclei taking part in it. This requirement can be illustrated by the Lawson criterion [8], which states that the triple product of temperature, energy confinement time and density must be higher than $5 \times 10^{21}\,\mathrm{keV\,s\,m^{-3}}$ to reach ignition, condition above which fusion reactions would be self-sustained. In the Sun, the Lawson criterion is achieved with the gravitational force due to its large mass. On Earth, the compliance of such criterion is sought by two different approaches:

Inertial confinement It aims to maximize the density inside a small D-T pellet. The pellet is shot with lasers or particle beams, leading to removal of material from the outer layers, causing the pellet implosion due to momentum conservation. Energy confinement time is very short in these experiments.

Magnetic confinement It confines a hot ionized gas (plasma) using strong magnetic fields that tie the charged particles in the plasma to the magnetic field lines by the Lorentz force. This method achieves longer energy confinement times but lower densities.

Since the decade of the 1950s, many experimental reactors have been built to investigate the different configurations of these two approaches. While the main principles of fusion energy have been proven and a maximum fusion power of 16 MW have been achieved [9], the ignition criteria has not been achieved yet and more energy is employed in the experiment than produced by fusion reactions. Thus, the fusion research community is focused on investigating the physical and technological challenges of building a fusion reactor capable of reaching ignition.

While the D-T reaction is aimed to be the main fusion reaction in future power plants, most of the experiments nowadays are carried out using only deuterium as fuel. This makes it possible to study the same physical phenomena while reducing the costs due to tritium handling – which is unstable and non-existent in nature –. Besides, since the D-D fusion reaction occurs in a shorter scale, leading to a lower neutron emission, the conditioning of equipment and diagnostics results somewhat easier.

1.3 Tokamaks

In magnetically confined fusion, the charged particles that make up the plasma are confined by means of the Lorentz force. Thus, the magnetic field lines must be shaped so that particles trace closed orbits along the field lines, following the gyromotion described in section 2.1. Depending on how the magnetic field lines are shaped, there are two main configurations of magnetically confined fusion reactors: stellarators and tokamaks. Stellarators [10] use complex shapes of the coils to produce a magnetic field were the orbit drifts are counterbalanced and therefore the plasma is confined. Tokamaks [7] use a simpler toroidal shape, as it is shown in figure 1.2, where the toroidal coils induce a toroidal magnetic field (blue) in the plasma, while an inner poloidal coil induce a current to the plasma, working as a transformer circuit (green). In turn, the plasma current produces a poloidal magnetic field, by means of the Ampere's law. The combination of a toroidal and a poloidal magnetic field produces helical magnetic field lines that ensure the plasma confinement.

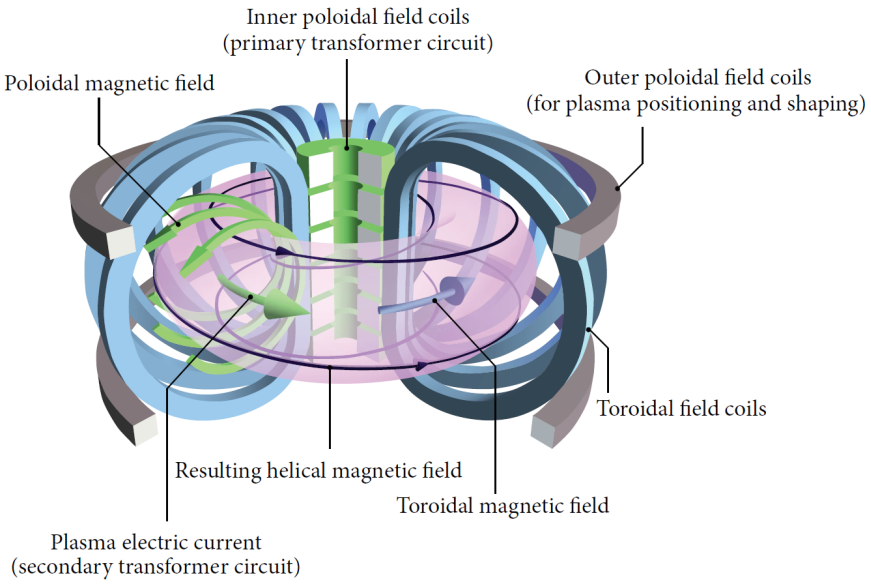

Figure 1.2: Schematic of the tokamak plasma and magnetic coils [11].

The resulting helical magnetic lines lie on magnetic field surfaces around a toroidal magnetic axis, as it can be observed in figure 1.3. The magnetic field surfaces can be defined as the contours of the poloidal flux, ψ.

$$\psi = \int_S \boldsymbol{B} \cdot \boldsymbol{n}\, dS \tag{1.2}$$

where S is a circle centred in the tokamak centre whose perimeter crosses the poloidal position where ψ is being evaluated. The helical shape of the magnetic field lines is crucial for plasma confinement, as we will see in chapter 2, and is described by the safety factor:

$$q = \frac{m}{n} = \frac{\text{number of toroidal circulations}}{\text{number of poloidal circulations}} \tag{1.3}$$

When the safety factor is rational, it can be easily illustrated as the number of toroidal turns that a field line makes to close into itself. The plasma q value must always be greater than 1 to keep stability.

Due to the high temperature of the plasma ($\approx 10\,\text{keV}$), any material in contact with it would degrade, becoming a risk to the tokamak integrity. For this reason, poloidal coils (grey in figure 1.2) are employed to shape the poloidal cross section of the plasma and localize the contact with the tokamak wall to a reinforced region (limiters), as it can be observed in figure 1.3(a). However, material limiters transfer a large amount of impurities to the plasma, diluting the fuel and increasing radiation losses. Therefore, the use of magnetic divertors (figure 1.3(b)) is widespread, since they avoid the direct contact between the outer boundary of the plasma (separatrix) and the vessel wall, reducing the amount of impurities that enter into the plasma. Poloidal coils are also employed to shape the plasma separatrix, as it has a strong impact on the plasma performance [12]. The region between the plasma boundary and the wall is called scrape-off layer (SOL).

Spherical Tokamaks (ST) [14, 15] are tokamaks with a more compact layout, by means of reducing the centre column to a minimum, retaining only the indispensable components. A very low aspect ratio is achieved, – $A = \frac{R}{a}$ in figure 1.4 –, being $A \sim 1.5$ in spherical tokamaks, whereas $A \sim 2.5$ in conventional tokamaks. The drastic aspect ratio reduction, in addition to the D-shape of the plasma poloidal section, give the plasma its characteristic spherical shape. Spherical tokamaks offer several advantages:

- Higher relative pressures can be achieved. This is translated in a cost reduction, since, for similar plasma pressures, it requires lower magnetic fields and thus lower currents through the coils.

$$\beta = \frac{p}{B^2/2\mu_0} \tag{1.4}$$

- The maximum relative pressure at which severe plasma instabilities appear impeding the operation, β_{crit}, is higher in spherical tokamaks due to its significantly lower aspect ratio [16], which increases the magnetic field convexity.

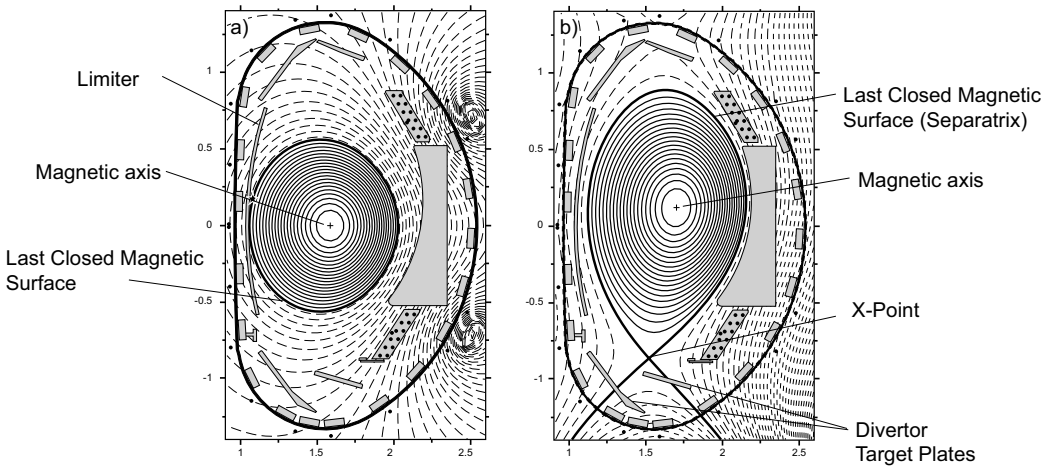

Figure 1.3: Poloidal cross section of a material limited plasma (a) and a divertor limited plasma (b) [13].

- Smaller plasma inductance facilitates current drive and makes possible to investigate non-inductive current drive technologies, which will allow continuous operation in fusion reactors.

However, the compactness of the spherical tokamak leads to minimum space in the centre column, complicating the power dissipation and preventing it from using superconductor magnets. Besides, due to the higher curvature in the spherical tokamaks, higher magnetic gradients are present, thus reducing the maximum operative magnetic field. Consequently, the total pressure in spherical tokamaks is lower than in conventional tokamaks.

Tokamaks are the most extended fusion devices, having achieved D-T experiments in TFTR [17] and JET [18] and the highest fusion power gain in history [9]. There are many operating tokamaks worldwide, such as, EAST [19] (China), ASDEX Upgrade [20] (Germany) or DIII-D [21] (USA), among many others. It will also be the first configuration to aim for ignition, in ITER [22], where the international effort of a number of countries that comprise more than half the global population is put on building what is considered the ultimate experimental fusion reactor. After ITER, a first demonstration power plant, DEMO [23], is envisaged. With regards to spherical tokamaks, devices like NSTX-U [24] or MAST-U [25] explore this alternative with the aim to construct the first prototype of a ST fusion power plant in STEP [26].

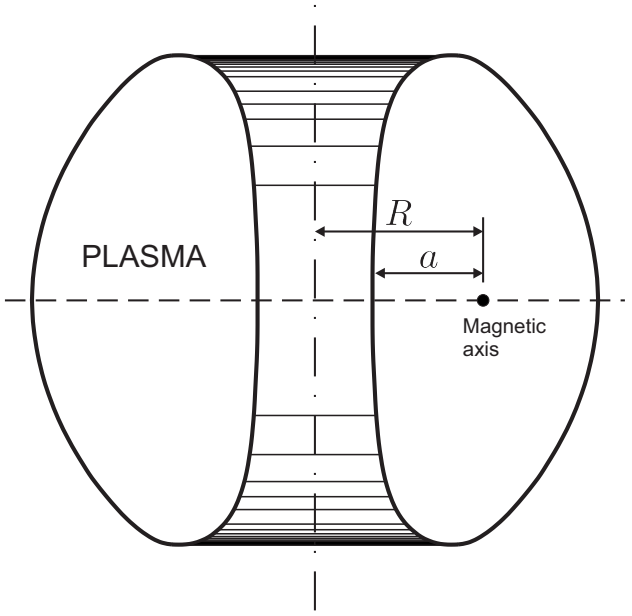

Figure 1.4: Poloidal cross section of a spherical tokamak [14].

1.4 Plasma Heating and Fast Ions

In addition to field line bending, current drive also contributes to plasma heating, following Ohm's law [27]. But ohmic heating does not suffice to reach fusion relevant temperatures in the plasma. Therefore, external heating is required in tokamaks to reach higher temperatures. The main heating systems are:

Neutral Beam Injection. The neutral beam injectors (NBI) [28] are high-current, high-power particle accelerators that inject a beam of neutral fuel (H, D or T) at an injection energy higher than the plasma temperature. Because they are neutrals, they are not affected by the magnetic fields and thus penetrate into the plasma, where they exchange charges with it. Once they are ionized, they get magnetically confined inside the plasma. The injected ions gradually transfer their energy to the plasma due to Coulomb collisions with other particles, thus increasing the plasma temperature.

Radio frequency heating. Radio frequency (RF) heating uses the resonant interaction between the gyromotion frequency of charged particles in a magnetic field and externally applied high-power electromagnetic waves [29]. Thus, the RF heating accelerates the particle population that is resonant with the external waves. Two main heating systems

are derived from this principle, depending on whether the external wave is resonant with the ions (Ion-Cyclotron Resonant Heating, ICRH) or the electrons (Electron-Cyclotron Resonant Heating, ECRH) in the plasma.

Fusion reactions Fusion reactions release energy in the form of kinetic energy of the products. The charged particle products remain magnetically confined inside the plasma and therefore contribute to increasing the plasma temperature.

These heating mechanisms produce a population of ions whose energy is significantly larger than the bulk thermal plasma, known as fast ions [30]. Due to their high energy, fast ions are characterized by a low collisionality, long mean free path, large gyroradius and large drift orbits [31]. The fast-ion distribution function is strongly correlated with the birth mechanism:

- NBI produce fast ions at the injection energy and with an anisotropic spatial and angular distribution defined by the beam geometry and the plasma shape and density. Since the NBI ion source is not purely formed by detached ions but also molecules, (e.g., D^+ or D_3^+ and D_3^+), fast ions with a half and a third the main injection energy are also found.

- ICRH produce fast ions at the resonant layer (radially localized). The energy distribution is broad and their angular distribution strongly perpendicular to the magnetic field lines, as the acceleration occurs in the ion gyromotion direction.

- Fast ions created in fusion reactions have a spatial distribution peaked at the magnetic axis (highest plasma density and temperature). Their angular distribution is nearly isotropic and their birth energy is defined by the fusion reactions.

$$D + D \rightarrow \mathbf{0.8\,MeV\ ^3He} + 2.5\,\text{MeV n} \quad (1.5)$$

$$D + D \rightarrow \mathbf{1.0\,MeV\ T} + \mathbf{3.0\,MeV\ p} \quad (1.6)$$

$$D + {}^3\text{He} \rightarrow \mathbf{3.7\,MeV}\ \boldsymbol{\alpha} + \mathbf{14.6\,MeV\ p} \quad (1.7)$$

$$D + T \rightarrow \mathbf{3.5\,MeV}\ \boldsymbol{\alpha} + 14.1\,\text{MeV n} \quad (1.8)$$

Fast ions are of paramount importance in tokamaks. They are responsible for achieving fusion relevant temperatures in the plasma. Besides, fusion-product fast ions will be responsible for sustaining an ignited state in future power plants [32]. Fast ions not only contribute to plasma heating but also

to current drive and momentum. Conversely, due to their high momentum and energy, their losses can produce a great damage onto the tokamak wall [33]. For this reason, fast-ion confinement and their loss mechanisms are extensively studied in conventional and spherical tokamaks [34, 35, 36].

1.5 Motivation and Goal

The goal of this thesis is to develop the numerical tools and to design the diagnostic that would enable the investigation of fast-ion losses induced by edge perturbations in ASDEX Upgrade and MAST Upgrade. ASDEX Upgrade [20] is a medium size tokamak, renowned for discovering the H-mode regime [37]. It is one of the tokamaks in the world with the most active research nowadays and it is equipped with a large amount of state-of-the-art diagnostics [38]. MAST Upgrade is a spherical tokamak that stopped its operation in 2013 to undergo a mayor upgrade that would enable new physics, like the super-X divertor, which aims to improve the exhaust capabilities of tokamaks. During this upgrade it has been equipped with a wide variety of diagnostics, such as the FILD detector, designed in the scope of this thesis.

Innumerable codes are available to model the many different aspects of fusion research. The fast-ion distributions are generally modelled as minority species inside the plasma, solving the Fokker-Planck equation [39] with a Monte-Carlo approach [40]. This is the case of ASCOT5 [41], LOCUST [42] or TRANSP [43]. The bulk plasma is frequently modelled as a fluid using the magneto-hydro dynamic (MHD) equations [44]. Two main families can be distinguished inside the MHD codes: the ideal and the non-ideal MHD codes. The ideal MHD models, like VMEC [45], do not account for magnetic reconnection events, whereas the non-ideal MHD codes, such as JOREK [46] or MARS-F [47], may solve the magnetic reconnection, including resistive effects. Ultimately, some hybrid codes, like MEGA [48], integrate the MHD equations and the fast-ion kinetic equation simultaneously, accounting for the wave-particle interaction. Some MHD codes like JOREK are including kinetic solvers [49] to account for the effect of the MHD perturbations on the minority species, like Tungsten impurity [50] or fast ions.

The fast ions can be experimentally observed with several techniques that can be classified depending on whether they aim to measure the confined or the lost fast ions. Among other techniques, the confined fast ions are measured using the Fast-Ion Deuterium-α (FIDA) [51] or the Beam-Emission Spectroscopy (BES) [52]. They infer the fast-ion content and energy based on charge exchange spectroscopy, using the intensity and the Doppler shift of the light emitted when a fast ion exchange charges with a neutral from the

NBI beam. The Neutral Particle Analyser (NPA) [53] is based on the same charge exchange reaction, although the NPA measures the neutralized fast ions that escape from the plasma confinement, colliding with the NPA probe. With regards to the lost fast ions, they can be directly measured with Faraday cups [54], which produce a current when the fast ions collide with them. The ubiquitous diagnostic to measure fast-ion losses is the scintillator-based Fast-Ion Loss Detector (FILD) [55], which infers the fast-ion loss velocity space working as a magnetic spectrometer.

In this thesis, the first FILD for MAST-U has been designed as part of the main scope of the upgrade. The data of the MAST-U FILD was aimed to be analysed during this thesis to study the fast-ion losses induced by Edge Localized Modes (ELMs). However, due to several delays in the MAST-U restart, the diagnostic has not been put in operation yet. To overcome the lack of experimental data in MAST-U, different approaches have been followed on the experimental and the numerical areas of this thesis. The experiments have been carried out in ASDEX Upgrade, where ELM-induced fast-ion losses were previously reported [56, 57, 58]. Thus, the experiments of this thesis aim to augment the scope of the reported observations, seeking the plasma parameters that mostly affect the fast-ion interaction. With regards to the numerical results, first principle modelling of fast-ion transport and acceleration during ELMs is carried out with ASCOT5, to reproduce the reported observations in ASDEX Upgrade and characterize the transport and acceleration mechanism of the ELM-induced fast-ion losses. Additionally, the fast-ion modelling in MAST-U makes it possible to compare the expected FILD signals in ASDEX Upgrade and MAST Upgrade.

1.6 Content of this Thesis

The content of this thesis is summarized here, with especial emphasis on the original work. The chapters are structured as follows:

Chapter 1 reviews the context and state of the art of nuclear fusion research.

Chapter 2 presents the charged particle equation of motion in an electromagnetic field, together with the resulting drifts and particle orbits in a tokamak. The Edge Localized Modes and the observation of ELM-induced accelerated fast-ion losses in AUG are introduced.

Chapter 3 describes the numerical tools employed in this thesis. An orbit following code (FIOS) is developed to account for 3D electric perturbations, with the aim to study fast-ion acceleration. Besides, a

time-evolving electromagnetic perturbation module is coded up in the Monte-Carlo full-orbit code ASCOT5. The multi-dimensional spline interpolation of the time-evolving module was also developed in the scope of this thesis.

Chapter 4 describes the two tokamaks covered in this thesis. The first MAST-U FILD is designed, accounting for the probe design, optical system, signal resolution, mechanical design and structural analysis of the diagnostic.

Chapter 5 shows the most recent experiments in ASDEX Upgrade dedicated to ELM-induced fast-ion losses, designed and analysed in this thesis. A dataset of AUG shots with similar plasma parameters has been constructed and the statistical analysis of the ELM-induced fast-ion losses is carried out.

Chapter 6 presents the fast-ion modelling during an ELM with ASCOT5. The observed transport and acceleration mechanism is described and the ELM-induced fast-ion losses in AUG are estimated. The fast-ion modelling in MAST-U makes it possible to estimate the FILD signal in a MHD-quiescent scenario and during an ELM crash.

Chapter 7 discusses and compares the presented experimental and numerical results. The future experiments and modelling plans are also described.

Chapter 2

Theoretical Background

2.1 Charged Particle Motion in Electromagnetic Fields

As it was mentioned in the previous chapter, tokamaks make use of magnetic fields to confine a plasma, – i.e., a ionized gas with quasi-neutral global behaviour –. Thus, it is of paramount importance to understand the charged-particle motion in a magnetic field, which is the basis of magnetic confinement. Consequently, this section will describe the fast-ion orbits and their main attributes in a tokamak plasma.

2.1.1 Motion in an Homogeneous Magnetic Field

The motion of charged particles in a magnetic field is governed by the Lorentz law [59]:

$$m\frac{d\boldsymbol{v}}{dt} = q(\boldsymbol{v} \times \boldsymbol{B}) \tag{2.1}$$

where m, q and $\boldsymbol{v}$ are the mass, charge and velocity of the particle, respectively, and $\boldsymbol{B}$ is the magnetic field. This equation can be decomposed as follows:

$$m\frac{d\boldsymbol{v}_{\parallel}}{dt} = 0 \tag{2.2}$$

$$m\frac{d\boldsymbol{v}_{\perp}}{dt} = q(\boldsymbol{v}_{\perp} \times \boldsymbol{B}) \tag{2.3}$$

where $\boldsymbol{v}_{\parallel}$ is the velocity component parallel to the magnetic field and $\boldsymbol{v}_{\perp}$ is the velocity component perpendicular to the magnetic field. In a uniform magnetic field, – constant in space and time –, the particle follows an uniform line motion along the direction of the magnetic field and a circular motion

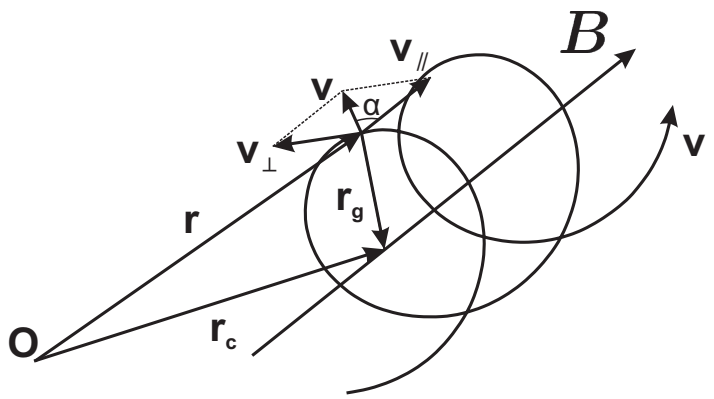

Figure 2.1: Helical motion of a charged particle in a homogeneous magnetic field.

around the magnetic field line. The result is an helical motion in the direction of $\boldsymbol{B}$, as it can be seen in figure 2.1. This helical motion may be described by three key parameters:

Gyroradius or Larmor radius Radius of the circular motion.

$$\rho = \frac{mv_\perp}{qB} \tag{2.4}$$

Cyclotron frequency Gyration frequency of the particle.

$$\omega_c = \frac{qB}{m} \tag{2.5}$$

Pitch angle Relative angle between the particle velocity and the magnetic field.

$$\Lambda = \cos\alpha = \frac{v_\parallel}{v} \tag{2.6}$$

The guiding centre motion can be defined as the motion of the helix axis as the particle circles around it [60, 61]:

$$\boldsymbol{r}_c = \boldsymbol{r} + \boldsymbol{r}_g \tag{2.7}$$

where $\boldsymbol{r}$ is the particle motion and $\boldsymbol{r_g}$ is the vector pointing towards the helix axis, as it is shown in figure 2.1:

$$\boldsymbol{r}_g = \frac{m}{qB^2}\boldsymbol{v} \times \boldsymbol{B} \tag{2.8}$$

The guiding centre motion is generally employed to reduce the computing effort of solving the entire particle gyromotion. This approach may be used in inhomogeneous magnetic fields, when $\nabla B/B \ll \rho$ and $\frac{dB/dt}{B} \ll \omega_c$.

2.1.2 Drift due to Additional Forces

If a conservative external force, $\boldsymbol{F}$, acts on the charged particle, the equation of motion becomes:

$$m\frac{d\boldsymbol{v}}{dt} = q(\boldsymbol{v}\times\boldsymbol{B}) + \boldsymbol{F} \tag{2.9}$$

Considering the guiding centre equation of motion [62]:

$$\begin{aligned}\boldsymbol{v}_c &= \boldsymbol{v} + \frac{m}{qB^2}\frac{d\boldsymbol{v}}{dt}\times\boldsymbol{B} \\ &= \boldsymbol{v} + \frac{1}{qB^2}\left(q(\boldsymbol{v}\times\boldsymbol{B}) + \boldsymbol{F}\right)\times\boldsymbol{B}\end{aligned} \tag{2.10}$$

and using the vector relation:

$$(\boldsymbol{v}\times\boldsymbol{B})\times\boldsymbol{B} = -\boldsymbol{v}_\perp B^2 \tag{2.11}$$

The guiding centre motion follows:

$$\boldsymbol{v}_c = \boldsymbol{v}_\parallel + \frac{\boldsymbol{F}\times\boldsymbol{B}}{qB^2} \tag{2.12}$$

Hence, the perpendicular component of the external force, $\boldsymbol{F}_\perp$, provokes a constant drift in the guiding centre motion. From the particle orbit perspective, the drift is due to a cyclic variation of the particle kinetic energy during its gyromotion. When the particle velocity points in the direction of the force, the Larmor radius increases, and when the velocity points in the opposite direction, the Larmor radius decreases. As a consequence, the oscillation of the particle Larmor radius produces the drift motion perpendicular to the force and the magnetic field, as it can be observed in figure 2.2(a). The drift occurs in opposite directions for the different charge signs. The net energy gain is zero during this process. Conversely, the parallel component, $\boldsymbol{F}_\parallel$, provokes an acceleration in the direction of $\boldsymbol{B}$:

$$\frac{d\boldsymbol{v}_{c,\parallel}}{dt} = \frac{\boldsymbol{F}_\parallel}{m} \tag{2.13}$$

2.1.3 Drift in an Inhomogeneous Magnetic Fields

In tokamaks, the magnetic field is curved toroidally, producing a magnetic field gradient along the radial coordinate, as it can be observed in figure 2.2(b):

$$\nabla\boldsymbol{b} = -\frac{\boldsymbol{R}}{R^2} \tag{2.14}$$

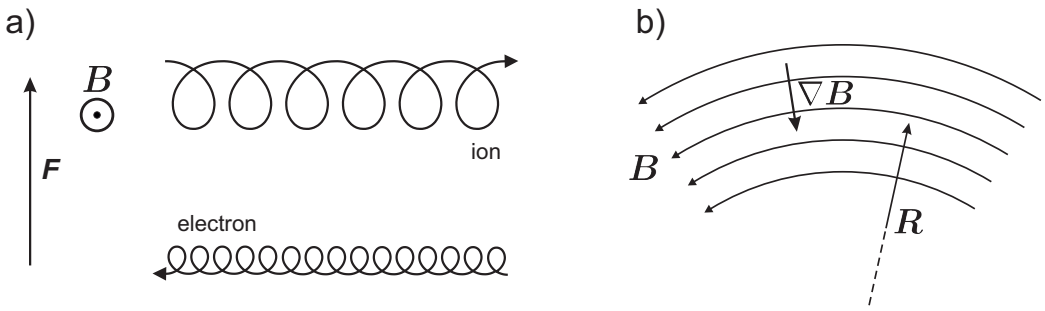

Figure 2.2: (a) Orbit drift due to a force perpendicular to the magnetic field. (b) Magnetic field gradient due to the field line curvature.

where $\boldsymbol{b} = \frac{\boldsymbol{B}}{B}$, and $\boldsymbol{R}$ is the tokamak radial coordinate. The force on a dipole caused by a magnetic field gradient is given by:

$$\boldsymbol{F} = -\mu \nabla \boldsymbol{B} \tag{2.15}$$

where $\mu = \frac{mv_\perp^2}{2B}$ is the magnetic moment associated to the gyromotion. Then, the resulting drift velocity is:

$$\boldsymbol{v}_{\nabla \boldsymbol{B}} = \frac{mv_\perp^2}{2qB^2} \boldsymbol{B} \times \nabla \boldsymbol{b} \tag{2.16}$$

Besides, the particle following a curved field line experiences a centrifugal force:

$$\boldsymbol{F}_{cent} = mv_\parallel^2 \frac{\boldsymbol{R}}{R^2} \tag{2.17}$$

Such a centrifugal force leads to a drift velocity:

$$\boldsymbol{v}_{cent} = \frac{mv_\parallel^2}{qB^2} \boldsymbol{B} \times \nabla \boldsymbol{b} \tag{2.18}$$

These two effects can be summed up:

$$\boldsymbol{v}_{cent} + \boldsymbol{v}_{\nabla \boldsymbol{B}} = \frac{m}{qB^2} \boldsymbol{B} \times \nabla \boldsymbol{b} \left(v_\parallel^2 + \frac{1}{2} v_\perp^2 \right) \tag{2.19}$$

In a very rough approximation, the resulting drift can be considered proportional to the particle energy, thus affecting the fast ions more severely. Now, let us consider a toroidal fusion device using a pure toroidal magnetic field. Equation (2.19) shows that the centrifugal force and the magnetic field gradient would lead to a vertical drift in opposite directions for ions and electrons. This would cause a lost of confinement and a charge separation that,

in turn, would produce an electric field. To avoid this, field lines are bent in the poloidal plane around a magnetic axis. Thus, an ion with a downward drift is pushed to outer magnetic field surfaces along half of its orbit while it is pushed to inner surfaces along the other half, resulting in a net lateral drift. This makes it possible to balance the $\nabla \boldsymbol{B}$ and curvature drifts, avoiding the lost of confinement. As a result, particles oscillate around different magnetic field surfaces along their orbits.

2.1.4 E × B Drift

In the presence of an electric field, the electric force $\boldsymbol{F} = q\boldsymbol{E}$ can be treated as an additional external force, giving rise to a drift, independent of the particle properties:

$$\boldsymbol{v}_E = \frac{\boldsymbol{E} \times \boldsymbol{B}}{B^2} \tag{2.20}$$

The $\boldsymbol{E} \times \boldsymbol{B}$ drift is responsible for macroscopic movements of the plasma which is believed to be fundamental for turbulence supression in the plasma edge [63]. Besides a parallel electric field could produce an acceleration in direction of the magnetic field:

$$\frac{d\boldsymbol{v}_\parallel}{dt} = \frac{q\boldsymbol{E}_\parallel}{m} \tag{2.21}$$

2.1.5 Constants of Motion and Adiabatic Invariants

A particle orbit is generally characterized by its conserved quantities, which can be separated into two groups due to their different nature: the constants of motion and the adiabatic invariants.

The constants of motion are quantities associated to a conservation law. The kinetic energy is a fundamental constant of motion. In the absence of external forces, the Lorentz force is always perpendicular to the particle velocity and therefore the kinetic energy is conserved:

$$T = \frac{1}{2} m v^2 \tag{2.22}$$

In classical mechanics, each symmetry in the motion of a system entails a conservation law, meaning that an action integral exists [64]. Consequently, the canonical momentum associated to the toroidal coordinate, φ, is a constant of motion in axisymmetric fields. The variation in the toroidal canonical momentum can be associated with the orbit radial transport [65].

$$P_\varphi = m v_\varphi R - q\psi \tag{2.23}$$

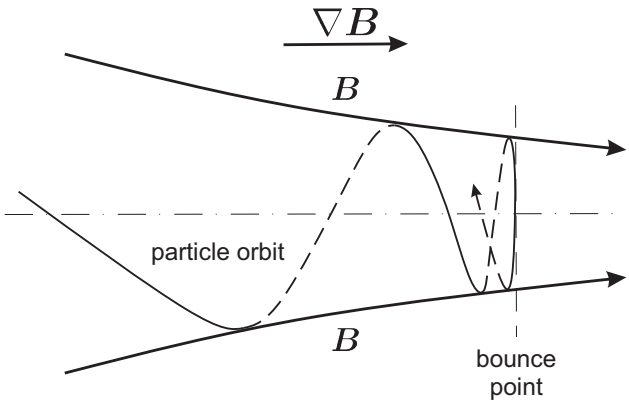

Figure 2.3: Schematic drawing of a linear magnetic mirror caused by the magnetic field gradient in the direction of the field line [13].

In the adiabatic approximation, the action integral is not constant due to the inhomogeneity of the magnetic field, but the variation is sufficiently small to be considered invariant:

$$\Delta I \approx e^{-\omega\tau} \tag{2.24}$$

where I is the adiabatic invariant, ω is the frequency of the periodic motion and τ is the time scale of the system change. The adiabatic invariant associated to the Larmor gyration is the magnetic moment:

$$\mu = \frac{mv_\perp^2}{2B} \tag{2.25}$$

The conservation of the kinetic energy and the invariance of the magnetic moment are the cause of magnetic mirrors. Consider a charged particle following a magnetic field line whose magnitude is gradually increasing along it, as it is illustrated in figure 2.3. Since both the magnetic moment and the kinetic energy are constant, the increase in B implies an increase in $v_\perp$ and, thus, a decrease in $v_\parallel$. If B continues to increase along the particle orbit, a point where $v_\parallel = 0$ will be reached and the particle will be reflected back (bounce point). A magnetic mirror can be also observed in tokamak plasmas, where the magnetic field is inversely proportional to R. As the particle moves around the magnetic axis, it explores regions of low R (High Field Side, HFS) and high R (Low Field Side, LFS). Therefore, the particle experiences a change in the magnetic field along its orbit. Whether the particle reaches a bounce point or not mainly depends on the particle initial conditions (B_0, Λ_0) and denotes the main difference between the two most frequent types of particle orbits in a tokamak, – i.e., passing and trapped –,

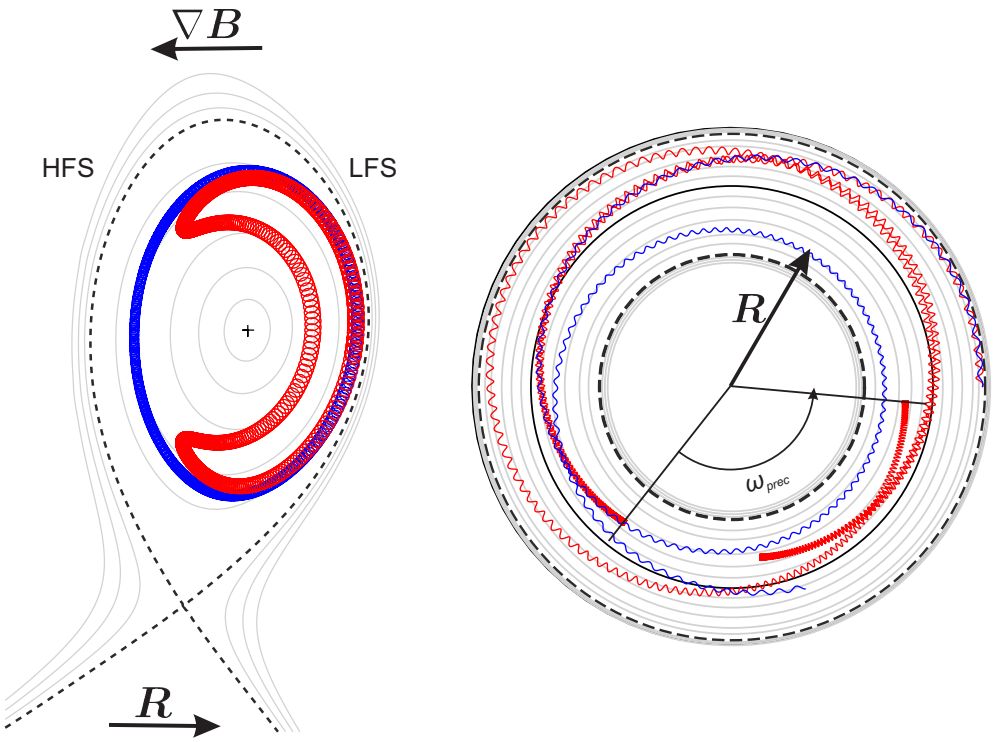

Figure 2.4: Poloidal (a) and top (b) view of a passing (blue) and a trapped orbit (red) [67].

which can be seen in figures 2.4(a) and 2.4(b). In a more detailed description, a broader range of particle orbits can be distinguished, whose transition from one type to another leads to high radial transport [66].

Passing Orbits

Passing orbits are those that do not find a bounce point and, hence, follow an helical trajectory along the torus, similarly to the magnetic field lines. However, as it was previously discussed, passing orbits do not lie on magnetic field surfaces because they are affected by the $\nabla \boldsymbol{B}$ and curvature drifts. Thus, the orbits are displaced radially from the magnetic surfaces.

Trapped Orbits

Trapped orbits reach two bounce points and therefore are trapped in the LFS, bouncing between the magnetic mirrors. They are also called banana

orbits due their characteristic shape in the poloidal plane (figure 2.4(a)). The bounce is a periodic event of frequency ω_b, called bounce frequency. Since the q profile normally grows at outer magnetic surfaces, the outer leg of the banana orbit covers a higher toroidal angle than the inner leg in a bounce period. This provokes a toroidal precession of the orbit, described by a bounce-averaged toroidal precession frequency, ω_{prec}, that is illustrated in figure 2.4(b). Trapped orbits are also called *banana orbits*, for their characteristic poloidal projection.

2.2 The Edge Localized Modes

A high confinement operating state, known as H-mode [37], spontaneously arises in divertor-limited plasmas above a certain power threshold. It is characterized by the formation of an edge transport barrier (ETB) that drastically reduces the energy and particle transport in a narrow region near the edge. Due to the profile stiffness [68], the transport in the core of the plasma is similar to the low confinement mode (L-mode), but the ETB enables steeper pressure gradients near the edge. This leads to high edge temperature and density, known as pedestal, that hoists the entire profile, thus increasing the stored energy by a factor greater than 2. The H-mode improves the fusion performance so it is the foreseen scenario for future fusion reactors [69].

In a H-mode regime, if the edge pressure gradient exceeds a certain limit, an explosive magneto-hydro dynamic (MHD) instability is driven, known as edge localized mode (ELM) [70, 71, 72, 73, 74, 75]. ELMs are fast (0.3 - 1 ms) filamentary plasma eruptions that expel particles and energy from the plasma leading to the collapse of the pedestal. ELMs decrease the plasma energy and particle content by a 5 - 10 %, leading to a high energy load on the divertor targets [76] and the plasma facing components (PFC) [77]. ELMs also lead to a contraction of the plasma volume. After the crash, the ETB and the pedestal slowly recover until the pressure gradient limit is exceeded again, triggering a new ELM [78]. Thus, ELMs are short repetitive MHD instabilities whose repetition frequency typically ranges between $\upsilon_{ELM} = 10 - 200\,\mathrm{Hz}$. An ELM is generally detected by the spikes in the Dα light emitted from the divertor target and the divertor shunt currents. The spikes are produced by the electrons ejected from the core plasma during the ELM. ELMs are also observed in the magnetic pick-up coils, depicting the high level of magnetic fluctuations during the ELM [79, 80]. Different types of ELMs can be distinguished based on a phenomenological classification. The two main type of ELM are distinguished by how the ELM repetition frequency

varies with the energy flux through the separatrix, P_{sep}[1], which are described as follows:

Type I ELMs The ELM repetition frequency increases with the energy flux:

$$\frac{d\nu_{ELM}}{dP_{sep}} > 0 \tag{2.26}$$

They are the largest and most common ELMs, since they are associated with high power H-mode regimes, desirable for high fusion performance.

Type III ELMs The ELM repetition frequency decreases with the energy flux:

$$\frac{d\nu_{ELM}}{dP_{sep}} < 0 \tag{2.27}$$

They are usually observed close to the L-H transition power as very small ELMs with repetition frequencies above 1 kHz. Gradually, they become bigger and more easily distinguishable with increasing heating power. Eventually, the type-III ELMs give way to the larger type-I ELMs.

Beside, other ELM types can be distinguished, generally smaller, associated to less common plasma conditions and without a clear correlation between ELM repetition frequency and the energy flux through the separatrix. These are the Type II ELMs [81], the grassy ELMs [82] or the type V ELMs [83], among others.

The peeling-ballooning (PB) model [71, 84, 85, 86] is the most accepted theoretical framework that explains the onset of type I ELMs. The PB model sets an stability boundary which is a combination of the ballooning mode and the peeling mode. The ballooning mode is a pressure-gradient driven mode with medium to high toroidal mode number (n), whose perturbation is localized at the LFS of the plasma (referred to as *ballooning* structure). The kink-peeling mode is driven by the pedestal current, low n and extremely localized at the plasma edge. The coupled peeling-ballooning mode, with intermediate toroidal mode numbers ($n \approx 10$), is destabilized whenever the PB stability boundary is crossed by a combination of steep pressure gradients and large edge currents. When the PB mode is triggered, the edge pressure and current crashes. This returns the plasma to a stable condition, starting the ELM cycle again. The PB model may also provide an explanation for smaller ELMs, although more qualitatively.

[1] This is generally depicted as a variation in the heating power as $P_{sep} = P_{tot} - \frac{dW}{dt} - P_{rad}$

ELMs are beneficial to reduce the impurity content in the plasma [87]. However, it is predicted that the peak heat load on future fusion reactors will exceed the tolerable material limit of $10\,\mathrm{MWm^{-2}}$ [88, 89, 90], causing a rapid erosion of the divertor target plates. Even though, the H-mode is the foremost regime to achieve a good fusion performance in future reactors. Therefore, ELM control techniques have been developed to mitigate or suppress ELMs in H-mode regimes, such as externally applied magnetic perturbations (RMP) [91], ELM pacing with pellets [92] or vertical kicks [93], among others. Additionally, alternative operational regimes that keep the high confinement and performance of the H-mode while supressing or mitigating the ELMs are also investigated [94], such as the QH-mode [95], the I-mode [96] and other small-ELM regimes [97].

2.2.1 Observation of accelerated fast-ion losses induced by ELMs

Recent experiments in ASDEX-Upgrade have reported a grow of the fast-ion losses correlated with the ELM bursts [98, 56, 57, 58]. The losses are measured with two scintillator-based Fast-Ion Loss Detector (FILD) located in different toroidal angles. Figure 2.5(a), shows the edge density, the magnetic loop voltage and the divertor current, typically employed to detect ELMs. Each peak in the signal corresponds to an ELM crash. An increase in the FILD signals (figure 2.5(b)) is seen to be correlated with the ELM activity. Figures 2.5(c) and 2.5(d) show a close-up of a single ELM crash, revealing that the peaks in the toroidally displaced FILDs are time-shifted. This suggests a 3D nature of the fast-ion losses during an ELM crash. Even though, Fast-Ion Deuterium-α (FIDA) measurements have shown that less than 0.3% of the total fast-ion population is lost in an ELM [99].

The intra-ELM velocity-space measurements of the fast-ion losses, which can be observed in figure 2.6(a), depict a population at energies tens of keV above the main NBI energy. A tomographic inversion of the measurement shows that this accelerated population is very localized, as it can be observed in figure 2.6(b). The accelerated population is observed during mitigated and non-mitigated ELMs but it is not seen in ELM-supressed regimes. This suggests a fast-ion acceleration induced by the ELM perturbation. Measurements of soft X-ray (SXR) and electron-cyclotron emission (ECE) depict bursts at the ELM onset, indicating electron acceleration, which further support this hypothesis [57, 100]. In the referenced works, the proposed acceleration mechanism is the parallel electric field arising during the ELM crash, when magnetic reconnection is believed to take place [101]. Observation of

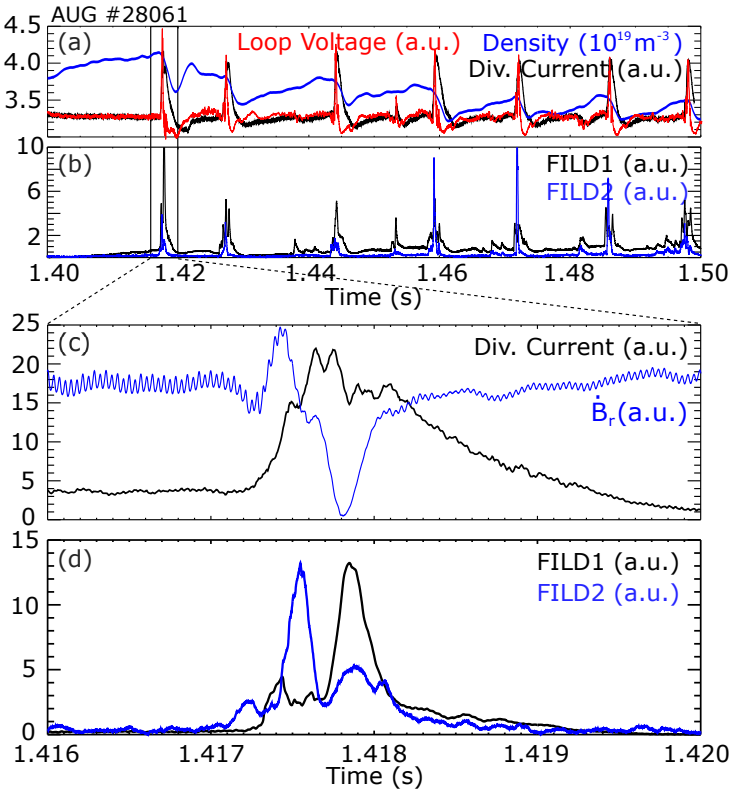

Figure 2.5: (a) Timetraces of the electron density (blue), the loop voltage (red) and the divertor current (black). (b) Timetraces of the two toroidally displaced FILDs. (c,d) Close-up of a single ELM for figure (a) and (b), respectively [56].

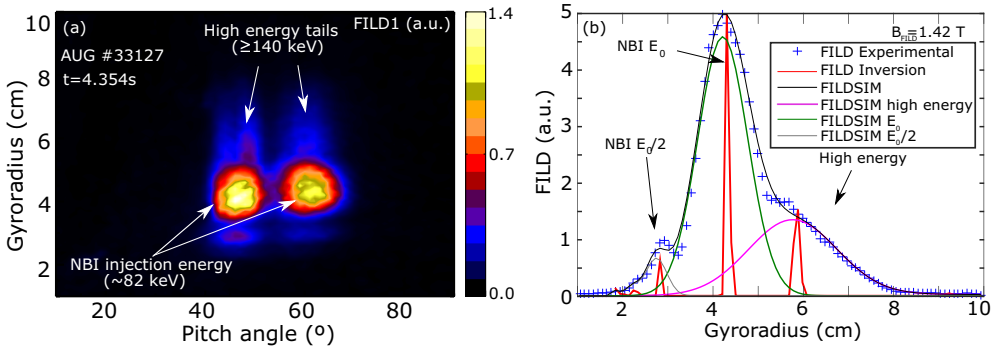

Figure 2.6: (a) Intra-ELM velocity-space measurements of the fast-ion losses [56]. (b) Gyroradius profile of the intra-ELM measurements between $\Lambda = [58°, 65°]$. The blue crosses are the experimental data, the red curves correspond to the tomographic inversion and the black curve is the reconstructed signal [56].

particle acceleration during magnetic reconnection events in MAST would support this hypothesis [102, 103]. However, this implies a pitch angle variation of the accelerated population, which is not observed in the experiments. For this reason, a recent work proposed a gyrotron acceleration induced by the vertical polarization of outwards-propagating ELM filaments with sizes smaller than the fast-ion gyroradius [104]. This mechanism would complement the parallel acceleration, thus keeping a constant pitch-angle structure.

Chapter 3

Simulation Models

This thesis employs state-of-the-art codes together with the development of new numerical tools that helps to understand the fast-ion transport and acceleration in MAST-U and AUG. The existing and developed codes used in this thesis are described in this chapter.

3.1 Numerical Tools

3.1.1 The ASCOT Code

ASCOT [105, 106, 107, 40] is a Monte Carlo particle-following code that solves the distribution function of minority species in magnetically-confined fusion plasmas. It has been developed since the 1990s within the research groups of Aalto University and the VTT technological Research Center in Finland. ASCOT solves the distribution function of a minority species described by the Fokker-Planck equation [39]:

$$\frac{\delta f}{\delta t} + \boldsymbol{v} \cdot \nabla f + \boldsymbol{a} \nabla_v f = C(f) \tag{3.1}$$

where $f = f(\boldsymbol{r}, \boldsymbol{v}, t)$ is the distribution function in the particle phase space; $\boldsymbol{a} = \frac{q}{m}(\boldsymbol{E} + \boldsymbol{v} \times \boldsymbol{B})$ is the acceleration, given by the Lorentz law; and C is the collision operator. The test particles equation of motion is resolved using the Boris leap frog integration method [108]. ASCOT may also solve the Fokker-Planck equation in the guiding centre phase space. However, the guiding centre approximation is not used in this thesis, since the large fast-ion gyroradius and large magnetic field gradient in spherical tokamaks produce large variations along the gyromotion that are no accounted for by the guiding centre equations.

To solve the particles orbits, some plasma parameters must be provided. ASCOT uses an axisymmetric magnetic field, where the toroidal magnetic field and the poloidal flux is given in 2D (R, z) matrices. The poloidal components of the magnetic fields are derived from the poloidal flux:

$$B_R = -\frac{\partial \psi}{R \partial z} \tag{3.2}$$

$$B_z = \frac{\partial \psi}{R \partial R} \tag{3.3}$$

In addition to this, a 3D magnetic perturbation in each component (δB_R, δB_φ, δB_z) can be included in 3D (R, φ, z) matrices. A one-dimensional electric field, radial to the plasma surface, is derived from the plasma potential. In ASCOT, the coupled effect of the fast ions on the electromagnetic perturbation, due to wave-particle interaction is not considered. The Monte Carlo algorithm resides in the collision operator, which aims to statistically model the Coulomb collisions between the test particles and the plasma. To evaluate the Coulomb collisions, the plasma kinetic profiles are needed. The standard set consists of one-dimensional temperature and density profiles as a function of the normalized poloidal flux:

$$\rho_{pol} = \sqrt{\frac{\psi - \psi_a}{\psi_s - \psi_a}} \tag{3.4}$$

where ψ_a and ψ_s are the poloidal flux values at the magnetic axis and the separatrix, respectively. 2D (R, z) profiles may also be given, but they are not generally necessary. Optionally, the plasma rotation can be taken into account in the evaluation of the collisions. This is essential for the impurity studies, but it is not important for fast particles studies and it is generally neglected. Due to the short orbital times and the low collisionality of the fast ions, the collision operator is neglected in this thesis, thus avoiding the stochastic term in the orbit following simulations. One of the crucial features of the ASCOT code is the detection of the orbit intersection with the tokamak wall, that enables to estimate the fast-ion losses. ASCOT works with both 2D (R, z) and 3D (R, φ, z) wall geometries. The code uses a modified computer-graphics ray-tracing implementation [109] to find an intersection of a line (orbit) and a planar element (wall). The 3D description of the wall makes it possible to study the wall loading in a realistic geometry with sharp elements. Additionally, this algorithm enables the development of synthetic diagnostics based on the estimation of the fast-ion loss velocity-space. ASCOT includes external tools to model the initial distribution of markers, such as BBNBI [110], a beamlet-based neutral beam ionization model that takes into account

the fine structure of the injector and the plasma kinetic profiles to produce a birth distribution of a given number of markers. BBNBI includes the beam geometries of the most relevant tokamaks, like AUG, ITER, JET or MAST-U. The inputs in ASCOT follows the COCOS3 sign convention [111]. The data is numerically interpolated using splines [112] in cylindrical coordinates (R, φ, z).

The ASCOT latest version, ASCOT5 [41], has undergone a full rewrite in C, using OpenMP + MPI to leverage the capabilities of Single-Instruction Multiple-Data Central Processing Units (SIMD-enabled CPUs). In comparison to its older version, ASCOT5 enables simulations with nearly an order of magnitude more markers with the same computational effort. Moreover, due to the large number of followed test particles, the parallelization of particles tracking becomes natural and thus a good scalability is foreseen. An ideal scalability would follow the curve $t_n = \frac{t_1}{n}$, where t_1 is the time consumed by a simulation run in a single node and n is the number of employed nodes. The scalability of the ASCOT5 code is tested in the Marconi High Performance Computer, based on Intel Xeon 8160 (Skylake) nodes. A test with 400000 markers, followed in ITER for 60 ms were performed for different numbers of CPUs. Figure 3.1 shows that ASCOT5 scales near-ideally with the number of cores. The inputs in ASCOT5 are implemented via interfaces, thus allowing to add new features to the code without affecting the codebase. Different implementations for the inputs will be added as the need arises, such as analytical models of the kinetic profiles or Fourier decomposed magnetic perturbation. In turn, the interfaces improve the long-term maintenance of the code.

ASCOT has enabled a wide variety of studies in fast-particle physics. The power load on the plasma facing components provoked by fast-ion losses have been estimated in tokamaks [113] and stellarators [114]. Besides, ASCOT has been employed to investigate the fast-ion transport due to externally applied resonant magnetic perturbations (RMP) [115, 65] and MHD modes [116, 117, 118], and it even has made it possible to create a loss map that connect losses to the underlying transport mechanisms. The code has modelled fast ions from different sources, such as NBI [119], fusion products [120] and ICRH [121]. ASCOT has also been used in runaway electrons [122] and impurity studies [123].

3.1.2 The FILDSIM Code

The FILDSIM code [124, 58] resolves the instrument function of a scintillator-based fast-ion loss detector (FILD). The FILD diagnostic [55] provides direct measurements of the fast-ion losses and gives information of their velocity

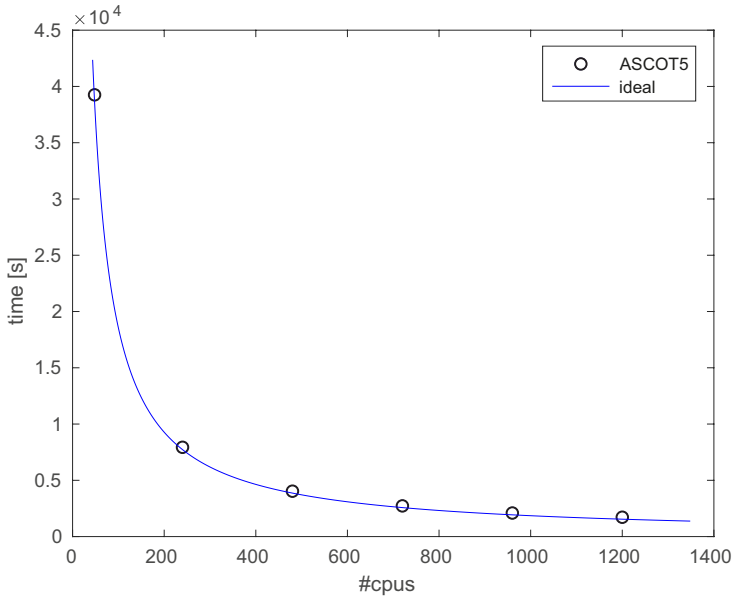

Figure 3.1: ASCOT5 scalability diagram in MARCONI SkyLake.

space. It works as a magnetic spectrometer, as it is illustrated in figure 3.2: Using the tokamak magnetic field, it collimates the escaping fast ions from the plasma that reaches the probe head following their gyromotion, until they strike a scintillator plate. The fast-ion velocity space, – i.e., gyroradius and pitch angle –, is inferred by the strike point on the scintillator plate, using a strike map that translates the plate coordinates into velocity space coordinates. FILDSIM uses the 3D geometry of the FILD main components and performs orbit tracing from the FILD pinhole to the scintillator plate to estimate the strike map and the signal intensity, coverage and resolution. The FILD main components are:

Protective shield Its distinctive D-shape enhances the pitch-angle detection range, avoiding self-obstruction of the measurements.

Collimator Its inner geometry is responsible for the diagnostic resolution and collimator factor (number of ions reaching the scintillator plate per ions on the collimator aperture).

Scintillator plate It is the active component of the detector. It consists of a plate coated with an ionoluminescent material, whose properties (scintillator yield, decay time, etc.) determine the detector capabilities [67].

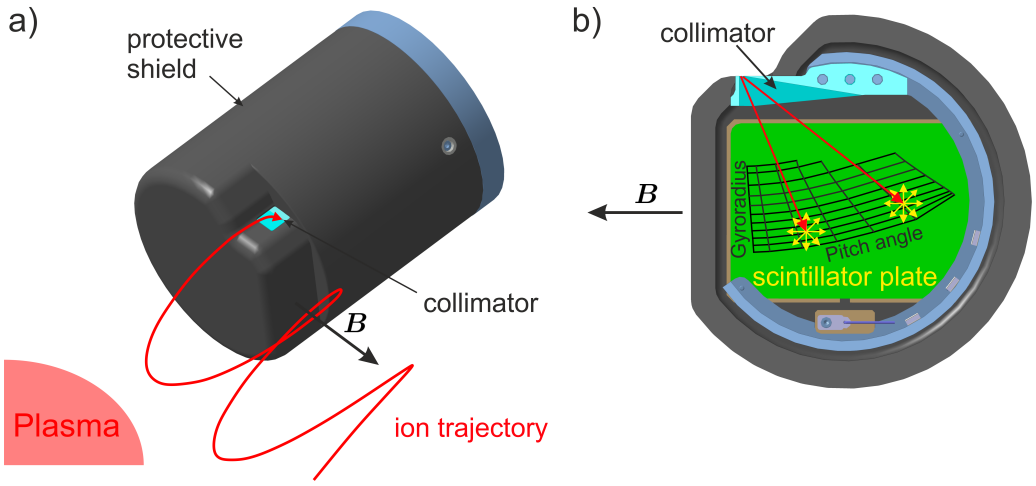

Figure 3.2: (a) FILD probe head and escaping fast-ion orbit reaching the aperture. (b) Scintillator plate where the collimated ions are dispersed using the tokamak magnetic field.

FILDSIM simulates ion trajectories started at the detector pinhole with a range of fixed gyroradii and pitch angles and a random distribution of gyrophase and position in the pinhole. The code assumes that the local magnetic field in the volume of the probe head is constant, and therefore the orbits are traced as geometrical helices. FILDSIM provides the location where each particle hits the scintillator plate, showing that orbits with equal gyroradius and pitch angle form a Gaussian distribution on the plate, due to the finite resolution of the detector. The strike map is computed using the centroid of these distributions. The size and shape of the distribution also provides numbers of the collimator factor and the signal resolution. Other codes like EfipDesign [125] have previously followed this same method to construct the strike map of the W7-AS [125] and the JET [126] detectors. Besides, FILDSIM carries out backward tracing to estimate the velocity-space range that would be self-obstructed by the probe external geometry.

The finite detector resolution will provoke the FILD signal to be a distortion of the fast-ion loss velocity space reaching the detector pinhole. FILDSIM uses the orbit tracing to develop a weight function that relates the fast-ion loss distribution at the pinhole and the distorted distribution at the scintillator plate. With this, FILDSIM applies tomographic inversion techniques [127] to the FILD signal and infers the undistorted fast-ion loss distribution, similarly to that obtained in other fast-ion diagnostics [128, 129, 130, 131, 132]. In particular, the 0^{th} order Tikhonov regularization is implemented in FILDSIM. The weight function can be used oppositely to generate a syn-

thetic signal, distorting a fast-ion loss distribution on the pinhole that can be provided by orbit following codes like ASCOT. A synthetic noise due to the camera efficiency or the background emission can be added to the synthetic signal. This has been essential in the comparison of simulated and measured fast-ion loss distributions [33] and the design of future FILD detectors, such as the ITER lost alpha monitor [133].

The FILDSIM code assumes an uniform magnetic field in the FILD probe, thus avoiding to integrate ion orbits and tracing them as geometrical helices. This approximation must be revised for spherical tokamaks, where the mayor radius is usually significantly lower and thus the magnetic field gradient is larger ($\nabla B \propto 1/R^2$). Moreover, the magnetic field is generally lower, which results in larger fast-ion gyroradii. To verify the approximation, the FILDSIM and the ASCOT codes are combined to produce a strike map using the fast-ion orbits integrated in an axisymmetric magnetic field [134]. The comparison is carried out for a scintillator plate placed at R = 1.50 m and 109 mm above the midplane in MAST-U, where a FILD detector is envisaged. The markers are followed from the pinhole aperture onto a scintillator plate and the strike points are employed to construct the strike map. Besides, a strike map using the uniform magnetic field approximations is also constructed. The strike-maps made with the uniform and the non-uniform magnetic field can be observed in figure 3.3(a). Figure 3.3(b) shows that the difference between the two strike maps in the gyroradius direction is negligible. The difference in the pitch angle direction, shown in figure 3.3(c), is larger at lower pitch angle values. This might be caused by the implicit consideration of straight magnetic field lines in the uniform magnetic field approximation, whereas the non uniform field accounts for the magnetic field curvature. Nonetheless, the difference in pitch angle is within 2.5°. Larger differences can be observed in the strike map borders, due to slight mismatches in the limits that cause the misrepresentation of the difference. Therefore, it is concluded that the uniform approximation is still valid for spherical tokamaks like MAST-U. In the case of AUG, the difference in the strike-points on the scintillator is in the order of 0.3 mm, well below the detector resolution.

3.1.3 Magneto-Hydro Dynamics Codes

The ASCOT5 code solves the equation of motion of minority species in electromagnetic fields and is generally used to investigate the fast-ion behaviour due to electromagnetic perturbations. However, ASCOT cannot compute the electromagnetic perturbations by itself. The perturbations can be due to different natures, such as the ripple caused by a finite number of toroidal field coils [135], externally applied resonant magnetic perturbations (RMP)

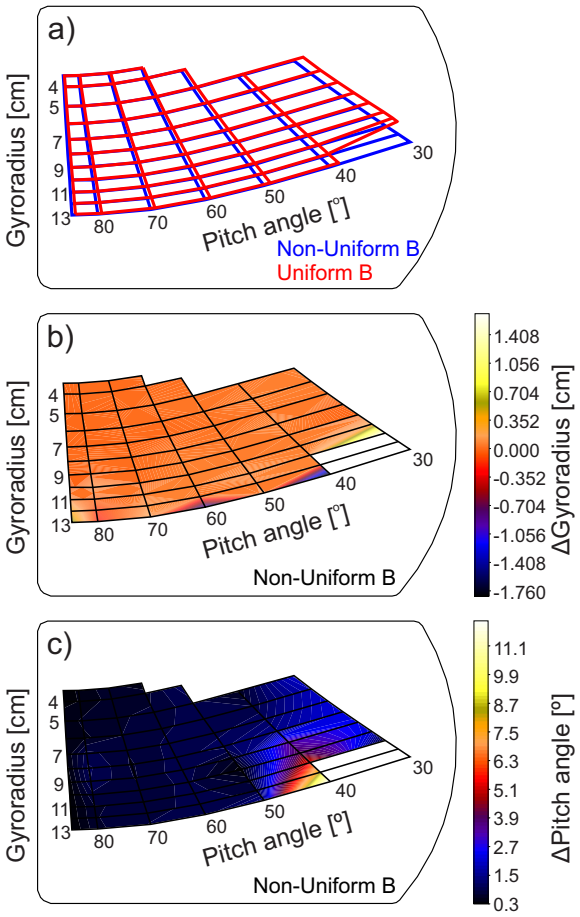

Figure 3.3: (a) Comparison between the non-uniform magnetic field strike map (blue) and the uniform magnetic field strike map (red). Difference in gyroradius (b) and pitch angle (c) between the uniform magnetic field and the non-uniform magnetic field strike maps, mapped over the non-uniform magnetic field strike map.

or MHD perturbations. In the latter case, an MHD code must be used to compute the perturbed electromagnetic perturbation. The resulting perturbation is then given to ASCOT as an input. Two MHD codes are used in this thesis: MEGA and JOREK. MEGA [48, 136] is an hybrid kinetic-MHD code. It describes the bulk plasma by the single-fluid nonlinear MHD equations, coupled with the energetic particle kinetic equations via the energetic particle current density. It evaluates the Ohm's law accounting for the plasma resistivity but it does not include neoclassical flows. MEGA uses 3D cylindrical coordinates to simulate the plasma volume and the SOL up to the first wall. The effect of energetic particles on the MEGA simulation is disabled in this thesis. JOREK [46, 137] is a non-linear MHD code particularly designed to simulate ELMs. It solves the visco-resistive single-fluid MHD equations including resistive wall effects, two-fluid effects and neoclassical flows. The full poloidal geometry up to the first wall is modelled in a 2D Bezier finite-elements grid and extended along the toroidal direction using a Fourier expansion.

3.2 Code development

3.2.1 3D Electric Perturbation

The existing orbit following codes do not generally support electric perturbations in the three spatial coordinates, which is essential to analyse the fast-ion acceleration due to a electric perturbation parallel to the magnetic field. For instance, ASCOT5 only accounts for a 1D electric field derived from the electric potential in a direction perpendicular to the magnetic field surface. To overcome this, a full orbit code called Fast-Ion Orbit Simulator (FIOS) was developed in this thesis. The code solves the Lorentz equation for charged particles, using the Boris leap-frog integration method [108] and a 2D (R, z) wall collision based on the efficient ray-polygon intersection algorithm [109]. Besides, the code accounts for a magnetic ($\boldsymbol{B}$) and a electric ($\boldsymbol{E}$) grid in cilindrical coordinates (R, φ, z) that are linearly interpolated and fed to the Lorentz equation, thus enabling simulations with a full 3D electric perturbation. The code was employed to assess for the first time the fast-ion acceleration caused by an electric perturbation parallel to the magnetic field lines. The results showed a resonant fast-ion acceleration above a few tens of keV, as it can be observed in figure 3.4(a), which shows the energy variation of fast-ions in 50 μs with the initial conditions given by the presented grid. This suggests that a parallel electric field arisising during magnetic reconnection events could be an acceleration mechanism of the ELM-induced fast-ion

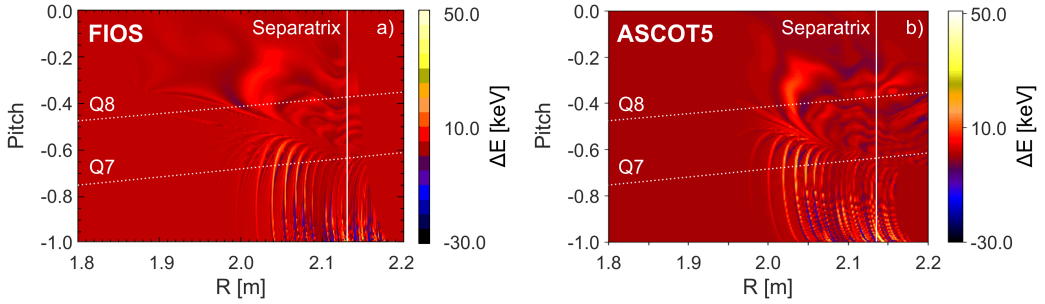

Figure 3.4: Fast-ion energy variation of test particles with a given R and pitch angle due to a parallel electric field in AUG [56, 57, 58], simulated with (a) FIOS and (b) ASCOT5 splines. The initial energy is 80 keV. The separatrix and the Q7-8 beams are marked with white lines.

losses [56, 57, 58]. Besides, this code has made it possible to perform a viability study for the imaging heavy-ion beam probe (i-HIBP) in AUG [138, 139]. The viability study estimated that the diagnostic would successfully detect density and electric potential perturbations in the plasma. The diagnostic is now installed in AUG and it is currently being commissioned.

Eventually, the 3D electric perturbation module was added to ASCOT5 as a new interface, using either linear interpolation or splines. The electric and the magnetic perturbations are given in separate grids because they are part of different ASCOT interfaces. Thus, it is the user responsability that the electric and the magnetic perturbations are coherent with the Maxwell equations [140]. A comparison between FIOS and ASCOT5 splines was carried out using the electric perturbation parallel to the magnetic field lines, described previously. The results are almost identical with the two codes, as it can be observed in figures 3.4(a) and 3.4(b), which shows the energy variation of the fast ions in 50 μs. Both codes depict the same magnitude and structures, which can be correlated to the orbit geometrical resonances [141, 142].

3.2.2 Time-Dependent Electromagnetic Perturbation

With regards to time-evolving perturbations, ASCOT may only account for field-aligned electromagnetic perturbations that rotates along the magnetic field surfaces with a constant frequency and amplitude using Fourier series [117]. This enables the modelling of field aligned perturbations such as TAEs or NTMs. However, ASCOT lacks for a general-purpose interface that accounts for time-evolving electromagnetic fields. A new module has been coded up in this thesis to include time-dependent magnetic and electric per-

turbations in ASCOT5, similarly to the static 3D perturbations described in section 3.1.1 and 3.2.1. The perturbations are described with temporal-cylindrical coordinates (R, φ, z, t), in separate 4D matrices for each component of the magnetic field (δB_R, δB_φ, δB_z) and the electric field (δE_R, δE_φ, δE_z). The inputs contain the position of each knot in a uniform 4D grid and the value of the perturbation as:

$$f_{ijkm} \begin{cases} R_i & i = 1, \dots, N_R \\ \varphi_j & j = 1, \dots, N_\varphi \\ z_k & k = 1, \dots, N_z \\ t_m & m = 1, \dots, N_t \end{cases} \tag{3.5}$$

The time-dependent perturbation is computed in ASCOT with a 4D spline interpolation. In a 1D domain, the spline interpolation is described as piecewise cubic polynomials twice continuosly differentiable, C^2, that pass through the set of given data points [143]. It is constructed so that the interval polynomials limit values coincide with the given values at the knots:

$$\left.\begin{array}{l} f_i(x_i) = f_i \\ f_i(x_{i+1}) = f_{i+1} \end{array}\right\} \quad i = 1, \dots, N_x - 1 \tag{3.6}$$

where $f_i(x)$ is the spline function in the interval $[x_i, x_{i+1}]$ and f_i is the given value at x_i. Besides, consecutive interval polynomials coincide at their first two derivatives at the interior knots so that the spline is C^2:

$$\left.\begin{array}{l} f_i(x_i) = f_{i-1}(x_i) \\ f_i'(x_i) = f_{i-1}'(x_i) \\ f_i''(x_i) = f_{i-1}''(x_i) \end{array}\right\} \quad i = 2, \dots, N_x - 1 \tag{3.7}$$

A simple way of satisfying this is a linear interpolation along the second derivative [144]:

$$f_i''(x) = M_i^x q_x + M_{i+1}^x p_x \quad x_i \leq x \leq x_{i+1} \tag{3.8}$$

where $q_x = \frac{x_{i+1} - x}{h_x}$ is the relative distance to the x_{i+1} knot; $p_x = \frac{x - x_i}{h_x}$ is the relative distance to the x_i knot; and $h_x = x_{i+1} - x_i$ is the interval between knots, which is constant in an uniform grid. M_i^x are the second derivative values at the knots, also called moments, which are unknowns. Equation (3.8) can be integrated and, by forcing the spline function to pass through the knots (equation (3.6)), it results in:

$$f_i(x) = f_i q_x + f_{i+1} p_x + \frac{h_x^2}{6} \left(M_i^x s_x + M_{i+1}^x r_x \right); \quad x_i \leq x \leq x_{i+1} \tag{3.9}$$

where $s_x = q_x^3 - q_x$ and $r_x = p_x^3 - p_x$. Therefore, this construction has N_x unknowns, – i.e., the moments at each knot –. The imposition of continuity of the first derivative at the interior knots (equation (3.7)) yields $N_x - 2$ equations. Thus, 2 boundary conditions must be imposed to solve the moments at each knot. The boundary conditions may be of different nature [145] but, in general, three are employed:

Natural It results from setting the second derivatives to zero at both ends, thus resulting in an effective reduction of the number of unknown moments:

$$M_1^x = M_{N_x}^x = 0. \tag{3.10}$$

Not-a-knot It consists of forcing continuity in the third derivative of the cubic spline near the boundary. Note that since the third derivative of a cubic spline is a step function, it is generally not continuous on the knots:

$$\begin{aligned} f_1'''(x_2) &= f_2'''(x_2) \\ f_{N_x-2}'''(x_{N_x-1}) &= f_{N_x-1}'''(x_{N_x-1}) \end{aligned} \tag{3.11}$$

Periodic It consists of imposing the same values and derivatives at both ends:

$$\begin{aligned} f_1(x_1) &= f_{N_x-1}(x_{N_x}) \\ f_1'(x_1) &= f_{N_x-1}'(x_{N_x}) \\ f_1''(x_1) &= f_{N_x-1}''(x_{N_x}) \end{aligned} \tag{3.12}$$

The existence and uniqueness of a solution, given a set of values and some boundary conditions, is demonstrated in section 2.4.1 of reference [143]. Once the moments are solved, the evaluation of the spline polynomials is carried out using equation (3.9), which only requires the data and moment at each knot. Thus, the total memory consumption of this method in $2 \times N_x$. The 2D splines can be constructed as a nested interpolation in a second dimension, y, of the given values and second derivatives on the first coordinate:

$$f_{ij}(x,y) = f_i(y)q_x + f_{i+1}(y)p_x + \tfrac{h_x^2}{6}\left(M_i^x(y)s_x + M_{i+1}^x(y)r_x\right) \tag{3.13}$$

$$f_i(y) = f_{ij}q_y + f_{ij+1}p_y + \frac{h_y^2}{6}\left(M_{ij}^y s_y + M_{ij+1}^y r_y\right) \tag{3.14}$$

$$M_i^x(y) = M_{ij}^x q_y + M_{ij+1}^x p_y + \frac{h_y^2}{6}\left(M_{ij}^{xy} s_y + M_{ij+1}^{xy} r_y\right) \tag{3.15}$$

$$q_y = \tfrac{y_{j+1}-y}{h_y}; \quad p_y = \tfrac{y-y_j}{h_y}; \quad h_y = y_{j+1} - y_i \tag{3.16}$$

$$x_i \le x \le x_{i+1}; \quad y_j \le y \le y_{j+1} \tag{3.17}$$

Now, each knot is comprised of 4 coefficients. Namely, the given data, f_{ij}; the second derivative along the x coordinate, M^x_{ij}; the second derivative along the y coordinate, M^y_{ij}; and the cross fourth derivative, $M^{xy}_{ij} = \frac{d^4(f_{ij}(x_i,y_j))}{dx^2dy^2}$. The existence and uniqueness of a solution of the derivatives can be demonstrated as an extension of the 1D spline [112]. Since the interpolation is continuously twice differentiable in the x and y coordinates, it is clear that $f_{ij}(x,y)$ is continuously twice differentiable in its entire domain. Equations (3.13), combined with (3.14) and (3.15), can be expressed as follows:

$$f_{ij}(x,y) = \sum_{\iota_y=1}^{4} \left(\boldsymbol{\phi_y}(\iota_y) \sum_{\iota_x=1}^{4} (\boldsymbol{\phi_x}(\iota_x)\boldsymbol{C}(\iota_x,\iota_y)) \right) \tag{3.18}$$

where $\boldsymbol{\phi_\chi} = \left[q_\chi, p_\chi, \frac{h_\chi}{6} s_\chi, \frac{h_\chi}{6} r_\chi \right]$ for $\chi \in \{x,y\}$ and $\boldsymbol{C}$ is the coefficient matrix:

$$\boldsymbol{C} = \begin{bmatrix} f_{ij} & f_{ij+1} & M^y_{ij} & M^y_{ij+1} \\ f_{i+1j} & f_{i+1j+1} & M^y_{i+1j} & M^y_{i+1j+1} \\ M^x_{ij} & M^x_{ij+1} & M^{xy}_{ij} & M^{xy}_{ij+1} \\ M^x_{i+1j} & M^x_{i+1j+1} & M^{xy}_{i+1j} & M^{xy}_{i+1j+1} \end{bmatrix} \tag{3.19}$$

Equation (3.18) minimizes the computational effort of the multi-dimensional splines evaluation. Note that this construction is commutative and therefore, the order in which the coordinates are interpolated is indifferent. The same extension may be carried out for a third dimension, z, and a fourth dimension, t, resulting in the following 4D spline evaluation:

$$f_{ijkm}(x,y,z,t) = \sum_{\iota_t=1}^{4} \left(\boldsymbol{\phi_t}(\iota_t) \sum_{\iota_z=1}^{4} \left(\boldsymbol{\phi_z}(\iota_z) \sum_{\iota_y=1}^{4} \left(\boldsymbol{\phi_y}(\iota_y) \sum_{\iota_x=1}^{4} (\boldsymbol{\phi_x}(\iota_x)\boldsymbol{C}(\iota_x,\iota_y,\iota_z,\iota_t)) \right) \right) \right) \tag{3.20}$$

where, similarly to the 2D splines, $\boldsymbol{\phi_\chi} = \left[q_\chi, p_\chi, \frac{h_\chi}{6} s_\chi, \frac{h_\chi}{6} r_\chi \right]$ for $\chi \in \{x,y,z,t\}$ and $\boldsymbol{C}$ is a 4D coefficient matrix that follows the same construction criteria as (3.19). In the same way, the existence and uniqueness of a solution of the derivatives can be demonstrated and the resulting piecewise polynomials are continuously twice differentiable on the entire domain. In this case, each knot stores 16 different coefficients, corresponding to the given value and the cross derivatives of the different coordinates. This results in a total data storage of $16 \times N_x \times N_y \times N_z \times N_t$. As an example, a typical grid of

$N_R = 100$, $N_\varphi = 320$, $N_z = 100$, $N_t = 50$ would consume 25 GB of memory for each component of the perturbation.

The 4D spline evaluation is implemented inside the Single Instruction Multiple Data (SIMD) vectorized loop in ASCOT. Thus, it can be technically considered that it will be executed in serial. For this reason, the minimized computational effort of equation (3.20), an operation that is repeated in ASCOT more than 3 times every integration step, is of paramount importance. In fact, it has been observed that the 4D splines evaluation using equation (3.20) is faster ($3.3\,\mathrm{ms}/(\mathrm{marker}\cdot\mu\mathrm{s})$) than the conventional 3D spline evaluation ($3.7\,\mathrm{ms}/(\mathrm{marker}\cdot\mu\mathrm{s})$). Besides, in contrast to Fourier series, a grid refinement would not affect the evaluation speed, even though it would have a drastic effect in memory consumption. The boundary conditions employed in ASCOT are natural in the R, z and t coordinates and periodic in the φ coordinate.

This new ASCOT5 interface enables the study of fast ions in the presence of fast MHD events in which the perturbed electromagnetic field changes on the fast-ion orbital time-scales. The module has been tested against a perturbation described with Fourier series that rotates along the field lines. The two methods were compared, showing equivalent results of the given values. Besides, the divergence, which must be zero according to Maxwell's equation [140], showed undetectable magnification due to numerical errors. The new time-dependent interface has been crucial for the investigation of fast-ion transport and acceleration during ELMs, presented in chapter 6.

Chapter 4

The Fast-Ion Loss Detector

FILD is a unique diagnostic in the detection of MHD-induced fast-ion losses [146, 147, 148, 149, 56, 57, 58] and it is crucial in the detection of fusion-product α-particle losses in D-T experiments [150]. It has been used in most large tokamaks, such as TFTR [55], JET [126], ASDEX Upgrade [151, 152, 153, 154], or DIII-D [155, 156]; spherical tokamaks like NSTX [157]; and stellarators like W7-SA [125]. The goal of this thesis, among others, is the development and analysis of a fast-ion loss detector in MAST Upgrade [158], at the Culham Centre for Fusion Energy, United Kingdom. However, due to several delays in the MAST Upgrade restart, the experiments of this thesis are carried out in ASDEX Upgrade, at the Max Planck Institute for Plasma Physics in Garching, Germany. A description of the two devices is presented here, together with a description of the main diagnostic employed in this thesis, the Fast-Ion Loss Detector.

4.1 The ASDEX Upgrade Tokamak

The Axially Symmetric Divertor Experiment Upgrade tokamak (ASDEX Upgrade or AUG) [20, 159, 160, 38] is a conventional medium size tokamak with an approximate aspect ratio of $A = \frac{R}{a} \approx 3.0$. It is renowned for discovering the H-mode regime in tokamak plasmas [37]. AUG is mainly conditioned for divertor-limited, lower single-null, D-shape plasmas but allows for a wide variety of alternative configurations. An upcoming upgrade of its upper divertor will enable the investigation of alternative magnetic configurations in divertor physics [161]. The maximum toroidal field is 3.1 T near the magnetic axis ($R = 1.65\,\mathrm{m}$), and the maximum plasma current is 1.6 MA. The typical plasma electron density and temperature in AUG are $\sim 1.0 \times 10^{19}\,\mathrm{m}^{-3}$ and $\sim 7\,\mathrm{keV}$, respectively. A total external heating of 30 MW is provided using

the following systems:

- 20 MW of NBI heating, provided by 8 beams [162]. The beams are organized into two boxes with a different operating voltage, 60 kV (Q1-Q4) and 93 kV (Q5-Q8). The injection geometry of each beam can be observed in figure 4.1.

- 4 MW of ICRH power with 4 ICRH antennas toroidally distributed around the low field side wall [163].

- 6 MW of ECRH power, fed through 8 gyrotrons [164]. The ECRH systems are fitted with movable mirrors that enable localized heating and current drive (ECCD).

AUG holds 16 RMP coils distributed in two rows (8 up and 8 down). The plasma facing components are made of Tungsten (W) with frequent boronization coating to reduce the tungsten impurity released into the plasma [165]. AUG experiments use deuterium and hydrogen as fuel. The main AUG parameters are summarised in table 4.1.

Parameter		AUG
Major radius	(m)	1.65
Minor radius	(m)	0.5
Plasma current	(MA)	1.6
Magnetic field at $R = 0.85\,\mathrm{m}$	(T)	3.1
NBI power	(MW)	20.0
ICRH power	(MW)	4.0
ECRH power	(MW)	6.0
Pulse length	(s)	10

Table 4.1: AUG key parameters.

AUG is equipped with an extensive range of diagnostics, including Charge Exchange Recombination Spectroscopy (CXRS) [63, 166], Fast-Ion Deuterium-α (FIDA) [51], Neutral Particle Analiser (NPA) [53], Visible and IR cameras. The most relevant in the scope of this thesis are the following:

Magnetic diagnostics An extensive range of magnetic coils are placed around the vacuum vessel. The current induced by magnetic fluctuations across these coils is used to infer many plasma parameters, such as the plasma current and position, halo currents, diamagnetic flows, high-frequency magnetic fluctuations, etc.

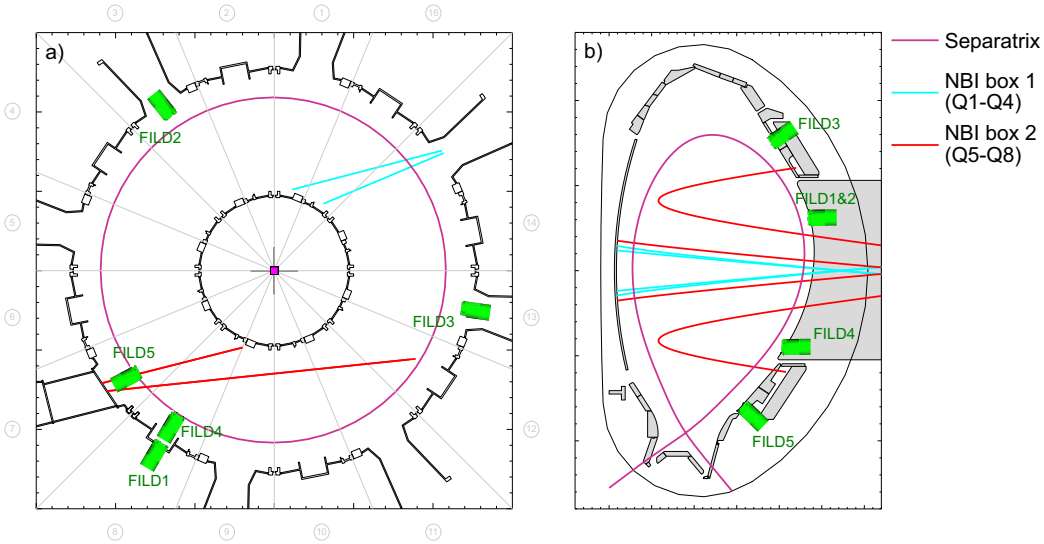

Figure 4.1: Top (a) and poloidal (b) view of the ASDEX Upgrade vacuum vessel.

Density and temperature profiles AUG employs Thomson Scattering (TS) [167], lithium beam emission spectroscopy (LIS) [168], deuterium cyanide laser interferometry (DCN) [169] and electron cyclotron emission (ECE) [170]. These heterogeneous diagnostics are combined to coherently estimate the electron temperature and density profiles through integrated data analysis (IDA) using Bayesian probability theory [171].

Divertor current The use of shunts in the AUG divertor makes possible to measure the current flowing through the divertor tiles [172].

FILD poloidal array AUG is fitted with 5 FILD diagnostics [151, 152, 153, 154] distributed around the AUG wall, as it can be seen in figure 4.1. Their different poloidal and toroidal positions make it possible to resolve the poloidal distribution of the fast-ion losses [173]. A fast reciprocating system in FILD4 makes it possible to adapt the radial position of the detector during the discharge, allowing for radial resolution of the fast-ion losses [174]. All the detectors are equipped with high resolution and high sampling frequency sensors.

4.2 The MAST Upgrade Tokamak

The Mega Amp Spherical Tokamak (MAST) [175, 176] was built in 1999, motivated by the favourable properties of low aspect ratio tokamaks ($A = \frac{R}{a} \leq$

Parameter		MAST	MAST-U
Major radius	(m)	0.85	0.85
Minor radius	(m)	0.65	0.65
Plasma current	(MA)	1.3	2.0
Magnetic field at $R = 0.85\,\mathrm{m}$	(T)	0.52	0.75
On-axis NBI power	(MW)	3.8	2.5
Off-axis NBI power	(MW)	0.0	2.5
Total NBI power	(MW)	3.8	5.0
Pulse length	(s)	0.6	5

Table 4.2: MAST and MAST-U key parameters.

1.5) observed in its predecessor, START [177], where record breaking high-β plasmas ($\beta_T \geq 30\%$) were achieved. In addition, MAST provides a larger plasma cross section, similar to other conventional medium size tokamaks, like ASDEX Upgrade or DIII-D, thus enabling cross-machine aspect ratio scaling of tokamak phenomena. In 2013, MAST stopped its operation to undergo a major upgrade (MAST-U) [178, 179] that would improve its overall performance, enable new exhaust physics and equip it with state-of-the-art diagnostics. The key parameters of MAST and MAST-U can be observed in table 4.2.

The MAST-U vacuum vessel consists of an up-down symmetric cylinder with an aspect ratio $A \approx 1.3$, as it can be observed in figure 4.2. It is equipped with 21 poloidal coils and 12 RMP coils distributed in two rows (4 up and 8 down). It contains two symmetric closed divertor chambers fitted with cryopumps. The plasma facing component and divertor tiles are protected by fine grain graphite. The toroidal field coils will provide toroidal magnetic fields up to 0.75 T near the magnetic axis ($R = 0.85\,\mathrm{m}$). Its upgraded solenoid makes it possible to sustain pulse durations up to 5 s and plasma currents up to 2 MA, although not concurrently. The solenoid will provide a maximum ohmic heating of 1 MW. Additionally, 2.5 MW on-axis and 2.5 MW off-axis NBI heating will be provided, also contributing to non-inductive current drive. The core plasma electron density and temperature will be $\sim 1.5 \times 10^{20}\,\mathrm{m}^{-3}$ and $\sim 3\,\mathrm{keV}$, respectively. MAST-U will use deuterium and hydrogen as fuel.

MAST-U is equipped with a wide variety of diagnostics, especially dedicated to plasma control and divertor physics, such as ~ 600 magnetic coils, Thomson Scattering (TS) near the midplane and in the divertor chamber [180], Charge Exchange Recombination Spectroscopy (CXRS) with unique resolution at the plasma edge [181], Visible and Infra-red (IR) cameras, etc.

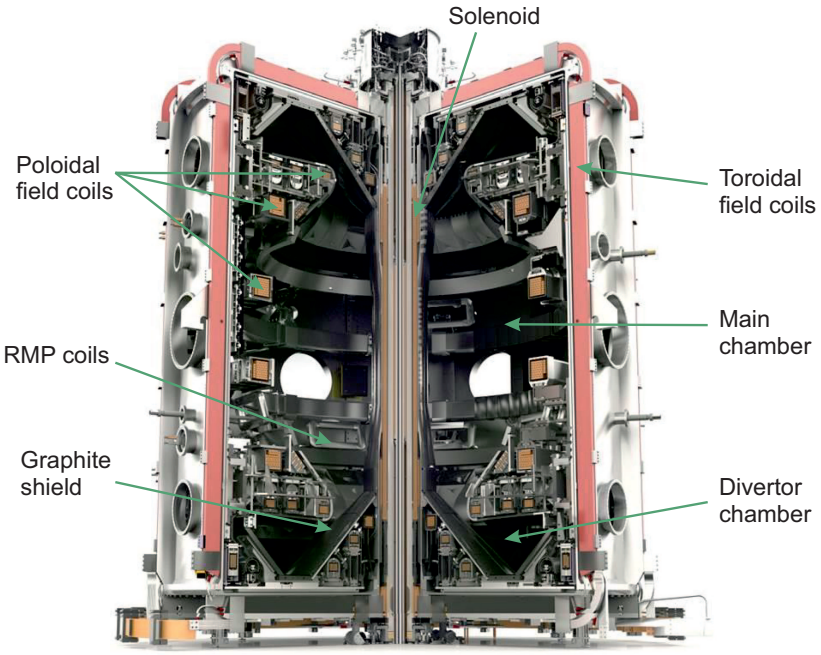

Figure 4.2: Cross section of MAST-U.

The confined fast-ion profile is measured with the Fast-Ion Deuterium α (FIDA) spectrometer [182] and the solid-state Neutral Particle Analyser (ss-NPA) [183]. The first MAST-U FILD is designed in the scope of this thesis and described in the following sections.

The MAST-U research plan [25, 184] will aim to explore the viability of spherical tokamaks as future fusion devices. Foremost, it will be focused on the investigation of alternative divertor configurations, which are illustrated in figure 4.3; such as the super-X configuration [185], which aims to extend the divertor legs, thus increasing the magnetic field lines connection length; or the snowflake configuration [186], which by means of achieving a second-order X-point, will spread the heat loads onto a larger wall surface. On the fast-ion physics, the MAST-U research plan will focus on optimizing fast-ion confinement in spherical tokamaks and investigate non-inductive current drive for non-pulsed tokamak operation.

The MAST Upgrade project endeavours further enhancements that will be combined with the upcoming experimental campaigns. These enhancements cover the installation of two additional NBIs, achieving a total neutral beam power of 10 MW; new diagnostic upgrades and the installation of a cryoplant to service the divertor cryopump and improve the solenoid cooling. RF heating based on Electron Bernstein Waves [187] is also envisaged.

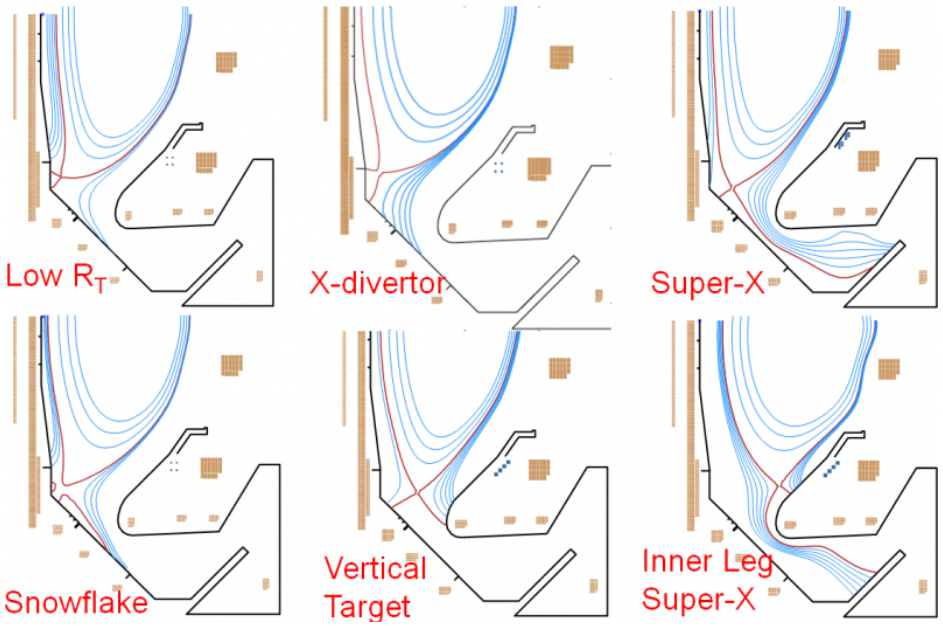

Figure 4.3: All the alternative divertor configurations in MAST-U (single and double-null).

4.3 The MAST-U FILD Design

The MAST-U FILD is designed to measure the NBI born fast-ion population in a wide variety of plasma scenarios, with the distinctive spatial and temporal resolution of the scintillator-based detectors. As it is mentioned in section 3.1.2, FILD works as a magnetic spectrometer, collimating the escaping ions from the plasma that reaches its probe head. Thus, the FILD probe is generally installed in regions where the fast-ion orbit drifts benefit the detection of escaping fast ions from the plasma, usually the scrape-off layer at the low field side, near the plasma edge. The MAST-U FILD is allocated in one of the main diagnostic ports, 109 mm above the midplane. Its design enables the adaptation of its radial position $[1.40\,\mathrm{m}, 1.60\,\mathrm{m}]$ and orientation with respect to the horizontal plane $[0°, 90°]$.

4.3.1 Probe Design

As it was mentioned in section 3.1.2, the main components of the FILD probe are the protective shield, the collimator and the scintillator plate. The geometry and relative position of these parts strongly affect the FILD measurement range and resolution, so they require a careful design and signal

Species	Energy (keV)	Gyroradius (mm)
D (1^{st} energy)	75	101
D (2^{nd} energy)	37.5	72
D (3^{rd} energy)	25	58
H (1^{st} energy)	75	72
H (2^{nd} energy)	37.5	51
H (3^{rd} energy)	25	41

Table 4.3: Energy and gyroradius ($B = 0.55\,\mathrm{T}$) of the fast-ion population in MAST-U.

mock-up with FILDSIM. The measurement range must be so that it covers the fast-ions gyroradii while it blocks the thermal ions from the bulk plasma. The fast ions in MAST-U are produced by the two neutral beams. The maximum beam voltage is 75 kV and thus, they inject hydrogen or deuterium at a main energy of 75 keV and half and third energies of 37.5 keV and 25 keV, respectively. Considering that the local magnetic field on the FILD probe will be approximately 0.55 T, the different fast-ion energies and gyroradii in MAST-U are summarised in table 4.3. The thermal ions gyroradii are considered to be below 20 mm ($< 3\,\mathrm{keV}$). Thus, the MAST-U FILD measurement range is aimed to be above 40 mm gyroradius.

Forward modelling with FILDSIM makes it possible to calculate the strike map and the synthetic signal for different collimator geometries and relative positions of the scintillator plate, with the aim to find a compromise between signal resolution, intensity and range. As an example, figure 4.4 illustrates the strike maps and the synthetic signals for three different collimator heights. The modelled fast-ion distribution is an artificial distribution that covers the three NBI energies in the entire pitch angle range. The results show that a larger height restricts the ion entrance, reducing the signal intensity and measurement range, but it improves the resolution. A height of 12 mm is chosen, because it allows to measure gyroradii above 35 mm and provides enough resolution to distinguish the three NBI energies, as it can be observed in figure 4.4(b). The same logic can be followed with the remaining geometrical parameters, whose final design is shown in figure 4.5(a). Figure 4.5(b) shows the detector resolution for different gyroradii. It can be observed that the resolution lessens at larger gyroradius values, which is geometrically caused by the collimator finite dimensions and is difficult to avoid. On the contrary, the resolution in pitch angle remains almost constant for the entire velocity-space range, $\Lambda = \pm 2^{\circ}$. Gyroradii above the maximum shown in the strike map of figure 4.4(b) may be measured, only limited by the plate size.

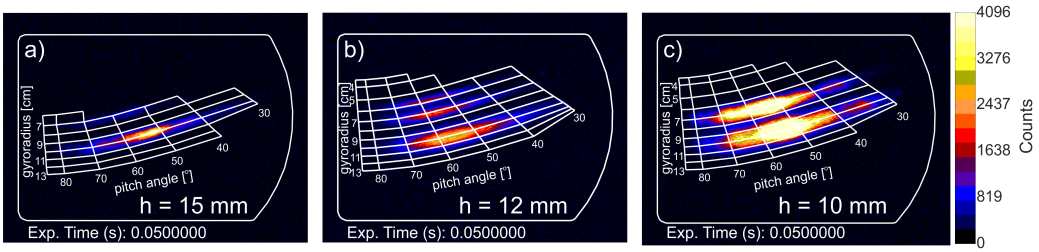

Figure 4.4: Strike map and synthetic frame for different collimator heights, (a) h = 15 mm, (b) h = 12 mm and (c) h = 10 mm. An artificial distribution of deuterium at the three injection energies (B = 0.55 T) covering the entire pitch angle range is used. (b) Corresponds to the strike map and synthetic signal of the final probe design.

The protective shield outer diameter is 15 cm to enclose the $5 \times 10\,\mathrm{cm}$ scintillator plate. This constitutes an important challenge in the design and manufacture of the probe head and the FILD mechanism. The protective shield is designed with a D-shape to avoid self-obstruction of particles reaching the collimator entrance, based on the ASDEX FILD design [151]. To check this, backwards modelling with FILDSIM from the collimator entrance are carried out, showing that only particles with gyroradii $< 40\,\mathrm{mm}$ and pitch angle $> 85°$ are self-obstructed by the protective shield, thus having a negligible effect on the FILD signal.

4.3.2 Mechanical System

The MAST-U FILD is designed to measure co-current fast-ion losses in forward field operation (B_t clockwise, I_p counter-clockwise from top). Thus, FILD is located on the low field side wall, 109 mm above the midplane, where the fast-ion loss detection is favoured by the ∇B drift. The probe closeness to the plasma increases the FILD signal but exposes it to higher heat loads. Therefore, the MAST-U FILD needs to adapt its radial position to keep a compromise between signal intensity and heat load. Besides, the FILD detection uses the tokamak magnetic field to infer the fast-ion velocity space. The strike map reconstruction relies on the magnetic field perpendicularity to the protective-shield planar face for a maximum measurement range (when the magnetic field vector is in the plane of the collimator aperture). This is especially challenging in spherical tokamaks, where different plasma scenarios can perform a broad range of edge q, modifying the magnetic field orientation and drastically reducing the measurement range if the probe head is not conveniently oriented. Thus, the MAST-U FILD needs to adapt its

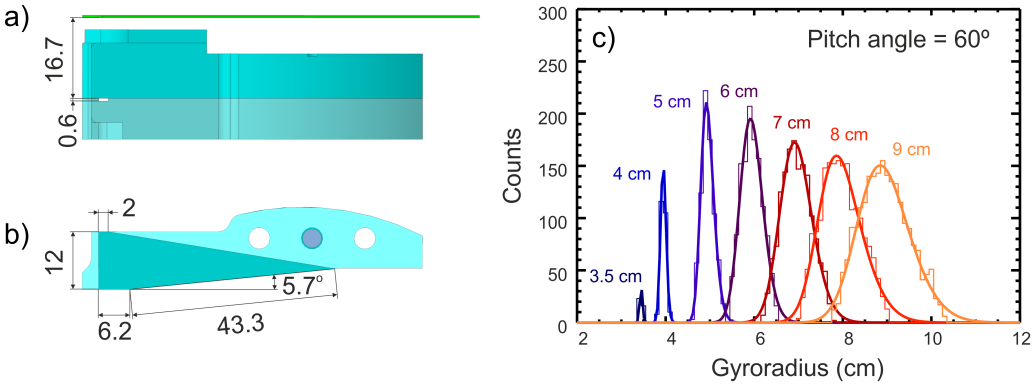

Figure 4.5: Collimator slit geometry and relative position of the scintillator plate (mm), top (a) and front (b) view. (c) Energy dispersion on the scintillator plate for several mono-energetic distributions on the pinhole. The broadening of these distributions give numbers of the signal resolution.

orientation to keep a good measurement range for a wide variety of plasma scenarios. The former feature is not required in conventional tokamaks, where the edge q range is narrower and a fixed probe orientation can be defined. As a result, the MAST-U FILD mechanism is able to independently adapt the probe head radial position $[1.40\,\mathrm{m}, 1.60\,\mathrm{m}]$ and longitudinal orientation $[0°, 90°]$ in a shot-to-shot basis. The mechanical system, shown in figure 4.6, is based on a telescopic design, where a support tube (blue) is axially driven by the push and pull of an axial drive (green) and its orientation is set by an outer tube (red) geared to a rotary actuator. The mechanical system is light-tight and provides direct sight to the scintillator plate from the bottom end of the axial drive.

Detailed Design

The FILD mechanical system is shown in figure 4.6 and 4.7. An outer shield is bolted to the vacuum side of a port plate, making a cantilever structure. The rotary drive rests inside the outer shield, supported by rotary bearings on its ends. The probe is supported inside the rotary drive by guide rails that, in turn, transmit the rotation to the probe. The rotation is externally controlled by a bellow-based rotary actuator, geared to the rotary drive. The linear motion is externally controlled using a bellow-based linear actuator that pushes and pulls the axial drive when it is compressed and stretched, respectively. The bellow compression is controlled by a worm gear in the vented side. In turn, the axial drive transmit this motion to the probe head,

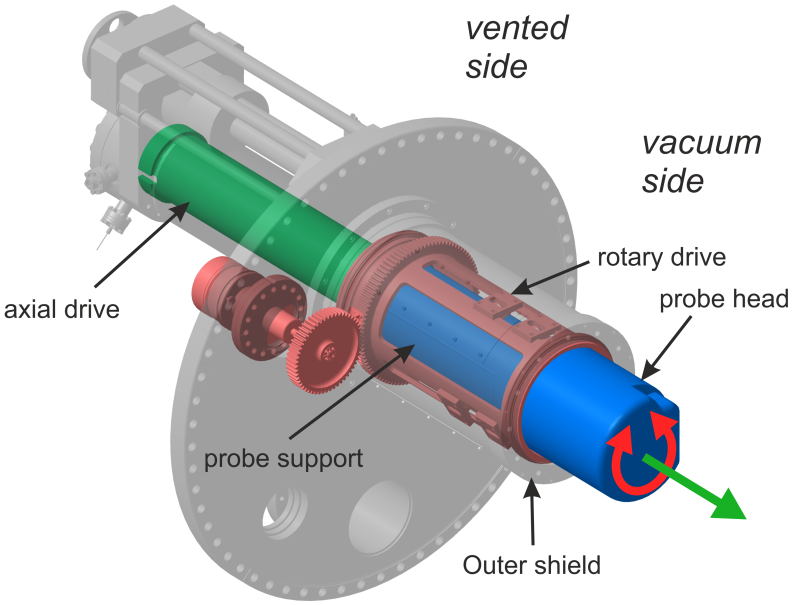

Figure 4.6: Rotary (red) and reciprocating (green) mechanisms which adapt the orientation and radial position of the FILD probe head (blue).

connected by a rotary bearing. A window port is placed at the bottom end of the mechanism, providing direct sight to the scintillator plate from the vented side. The FILD structural components are made of stainless steel 316L due to its high yield and tensile strengths while low magnetic permeability and low impurity emission to the plasma.

The mechanism is installed in an ultra-high vacuum (UHV) environment ($\sim 10^{-9}$ bar). Besides, no lubrication can be employed in the mechanism because they could lead to a release of undesired impurities in the plasma. For this reason, the moving parts in the FILD mechanism are low friction and vacuum compatible parts, such as the Franke® GmbH low-friction wire-race ball bearings, used to support the rotary drive and to connect the axial drive to the probe head. Special care has been taken in the material selection of moving parts to prevent cold welding [188]. For example, aluminium bronze and stainless steel have a low propensity to cold weld. Thus, the guide rail rollers are made of aluminium bronze 2.0966, while the guide rail races are milled on the stainless steel 316L probe support. The same material pairing is used for the gears, where the actuator gear is made of aluminium bronze 2.0966 and the rotary drive gear is made of stainless steel 303. The Franke GmbH bearing balls are made of silicon nitride, a ceramic material with a low probability to cold weld.

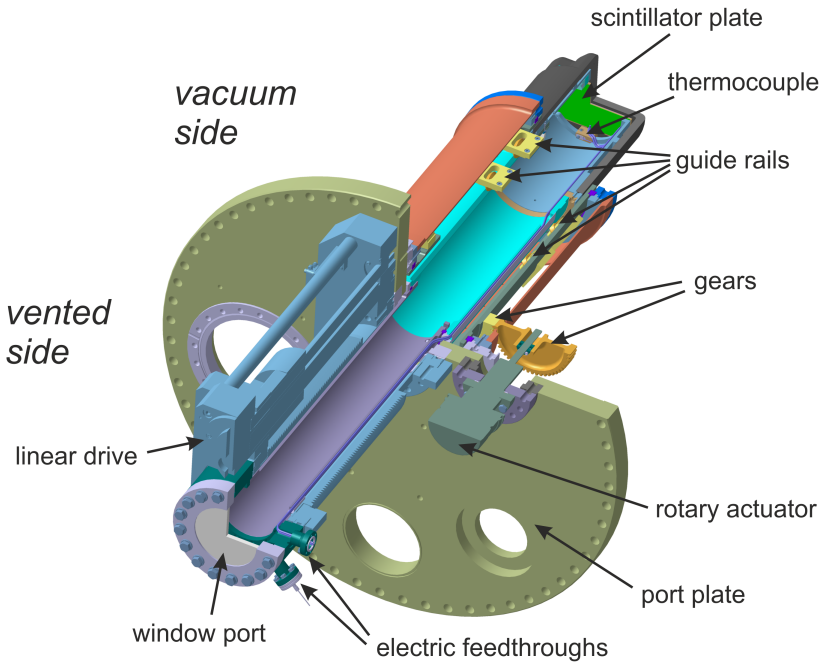

Figure 4.7: Detailed design of the MAST-U FILD.

The protective shield must withstand strong electromagnetic and thermal loads. It is made of Erodex Duragraph® fine grain graphite, with an average grain size of 15 μm. The graphite provides high heat load resistance and a rather high conductivity (90 $\frac{\mathrm{W}}{\mathrm{mK}}$). This makes the protective shield able to isolate the FILD inner components during operation, while allowing to safely evacuate the heat to other structural components between pulses. Erodex Duragraph® graphite is also employed in the poloidal limiters and divertor tiles, thus being an acquainted material in impurity emission and maintenance. The high temperatures on the protective shield during the shots are expected to be very localized and transient. Thus, a thermocouple monitors the protective shield temperature, whose information will be used to set a safe radial position of the probe. Besides, during the MAST-U conditioning, the entire vessel is baked up to 170 °C for tens of hours, producing a considerable thermal stress in the mechanical system. This is especially important for the graphite shield due to its brittle nature. The graphite low thermal expansion coefficient ($\alpha_{graph} = 2.9 \times 10^{-6} \frac{\mathrm{m}}{\mathrm{mK}}$), with respect to stainless steel ($\alpha_{st} = 16 \times 10^{-6} \frac{\mathrm{m}}{\mathrm{mK}}$) makes it necessary to add some clearance between the protective shield and its stainless steel inner support, allowing for thermal expansion of the inner support. The clearance at the protective shield inner

diameter ($\varnothing = 130\,\mathrm{mm}$) is:

$$\varnothing \cdot (T_{baking} - T_{RT}) \cdot (\alpha_{st} - \alpha_{graph}) = 0.255\,\mathrm{mm} \approx 0.3\,\mathrm{mm} \tag{4.1}$$

Structural Analysis

A thorough optimization of the structural components has been carried out to reduce the FILD mechanical system size and weight. Even though the structure weight has been drastically reduced, it is estimated to be $\sim 30\,\mathrm{kg}$, due to the large size of the probe head and the complexity of the mechanism. Moreover, as described in the previous section, the in-vessel assembly is bolted to a port plate, forming a cantilever structure. Therefore, the FILD structural performance must be assessed to guarantee the mechanism and the port plate integrity. Generally, the FILD structure is only affected by the gravitational load. But in disruption-likes events [189], a current may be induced through the FILD structural components, thus producing a sudden load on the system. The load is caused by the current flowing through the structure and the tokamak magnetic field following the Laplace force equation. Thus, the total downward force is:

$$\boldsymbol{F} = m\boldsymbol{g} + \boldsymbol{I}L \times \boldsymbol{B} \tag{4.2}$$

A finite element analysis (FEA) of the in-vessel structure has been carried out in ANSYS Workbench® to analyse the structural performance during a shock produced by a current of 2 kA, besides its own weight. The model is based on a simplified version of the three main structural components: the outer shield, the rotary drive and the probe support. The outer shield bottom face is bonded to the inertial reference frame, mimicking the bolted joint to the port plate. The contact between the three different bodies are modelled as frictionless contacts. Besides, to avoid rigid body motions, a single point of the rotary drive and the probe support are fixed (the nearest to the bolted joint). The external force in equation (4.2) is defined as a distributed load on each body. The probe head is not included in the model but its weight is added as an external load at the front end of the probe support. Figure 4.8 shows the resulting von Mises stress on the system, with highlighted stress concentration areas. The maximum von Misses stress is 5 times below the material yield stress. The force reactions on the rotary bearings are 6 times below the recommended value (8 times below the static load rating, $C_0 = 31\,\mathrm{kN}$). The bolted joint between the FILD outer shield and the port plate would experience a vertical force of 1295 N and a torque of 237 Nm. This result is used to dimension the bolted joint, with 12 bolts M6 × 20 distributed in a $\varnothing 248\,\mathrm{mm}$ circumference.

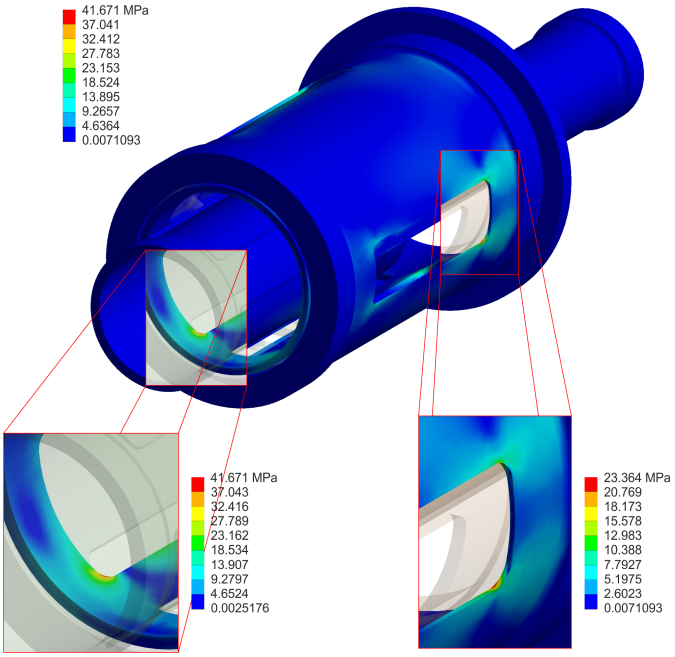

Figure 4.8: Equivalent von Mises stress on the in-vessel structural components. Stress concentration areas are highlighted.

4.3.3 Acquisition System

The scintillator plate can be directly observed from a window port at the rear end of the mechanical system. Thus, the optical system and cameras are placed outside the vacuum vessel supported by two X95 beams, as it is shown in figure 4.9(a). This provides full accessibility to the data acquisition system during the experimental campaign, enhancing its maintenability. To leverage the FILD measurements, the acquisition system must provide high resolution images of the scintillator plate, allowing for velocity-space resolution of the losses, and high sampling rates that enable the detection of high frequency fluctuations and Fourier analyses of the signal. In MAST-U, a coupled-charged device (CCD) [190] camera provides the high spatial resolution and an avalanche photodiode (APD) [191] camera provides the high sampling frequency. A 50:50 beam splitter is employed to divert the light to the two different sensors that measure the fast-ion losses simultaneously.

The CCD camera is a PCO Pixelfly QE camera, with a resolution of 1392×1024 px enclosed in a $9.0\,\text{mm} \times 6.6\,\text{mm}$ sensor. Its typical sampling frequency is 60 Hz and its maximum quantum efficiency is 65% near the 500 nm wavelength. The dynamic range of the PCO Pixelfly QE camera is 12 bits and its noise-to-signal ratio is 0.04 %. It is connected to the diag-

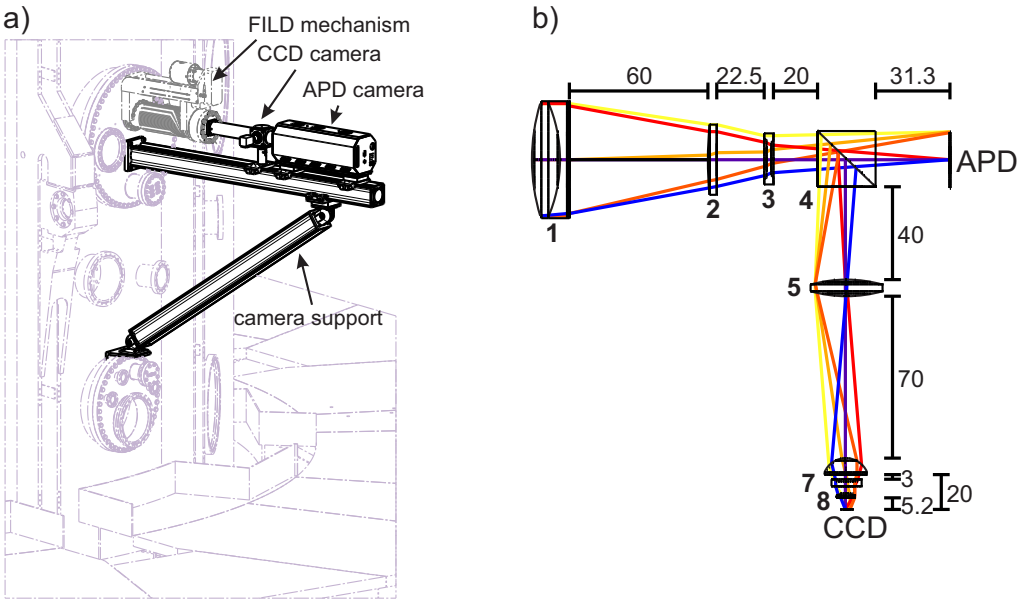

Figure 4.9: (a) Light acquisition and support system. (b) Optical system layout (mm) and ray tracing of the two branches. The numeration corresponds to table 4.4.

nostic PCs via an Ethernet connection. The APD camera is an APDCAM 10G [192] developed by Fusion Instruments® for high-frequency low-level light measurements. It consists of an 8×8 array of Hamamatsu avalanche photodiodes arranged in a $20\,\text{mm} \times 40\,\text{mm}$ sensor. Its maximum sampling frequency is 2 MHz, its typical quantum efficiency is 85% at 650 nm, higher than photomultiplier tubes, and unlike normal photodiodes, it has internal gain. It has a 14 bit resolution and a noise-to-signal ratio of 0.2 %. Due to its high sampling frequency, the data transmission of the APDCAM can reach up to 2.5 GB during a single shot. For this reason, a 10 Gigabit Ethernet connection with the control PC is used.

The two optical branches produced by the beam splitter are designed with the Qioptic Winlens® software. Winlens® is a ray tracing code that allows to dimension the optical system and calculate the resulting image magnification and Seidel aberrations with a large database of standard lenses. In the design, the scintillator plate is defined as a 100 mm object at 1.10 m from the first lens. Due to the different size of each sensor, the magnification of each optical branch is different: $m = 0.048$ for the CCD camera and $m = 0.25$ for the APD camera. The resulting optical system is shown in figure 4.9(b). Firstly, the APD branch has been produced based on the Tessar, Heliar or the Super-Dynarex lens designs [193], using an achromat, a plano-convex

Element	Type	Focal length (mm)	⌀ (mm)
1	Achromat	120	50
2	Plano-convex	300	31.5
3	Symmetric-concave	-50	22.4
4	Beam splitter		
5	Symmetric-convex	50	31.5
6	Aspheric	15	18
7	Plano-concave	-30	12.7
8	Plano-convex	12.5	8

Table 4.4: Lens description, according to the numeration in figure 4.9(b).

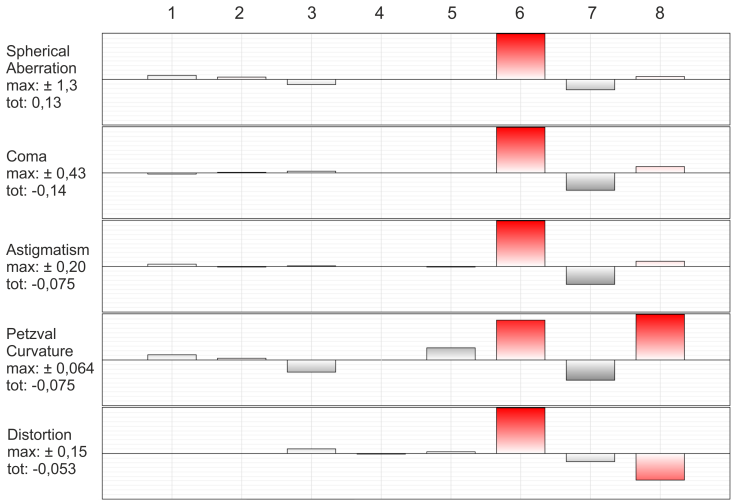

Figure 4.10: Seidel aberrations of each optical component. The numeration corresponds to table 4.4.

and a symmetric-concave lens. The beam splitter is allocated between the third lens and the APD sensor, introducing the CCD branch. Therefore, the first three lenses are common to the two branches. Further, in the CCD branch, a symmetric-convex lens works as a field lens and 3 additional lenses achieve the required magnification. The different lenses of the optical system are described in table 4.4. The two branches produce a very low Seidel aberration, as it can be observed in figure 4.10.

The scintillator plate consists of a stainless steel plate coated with a layer of ionoluminescent material powder ($< 0.1\,\mathrm{mm}$). The employed scintillator material is yttrium aluminum garnet activated by cerium ($Y_3Al_5O_{12}:Ce^{3+}$, YAG:Ce or P46). The P46 is characterized for a rather low yield ($\approx 10^3$ photons/ions) but fast decay time ($\approx 70\,\mathrm{ns}$) [194], which makes it possible

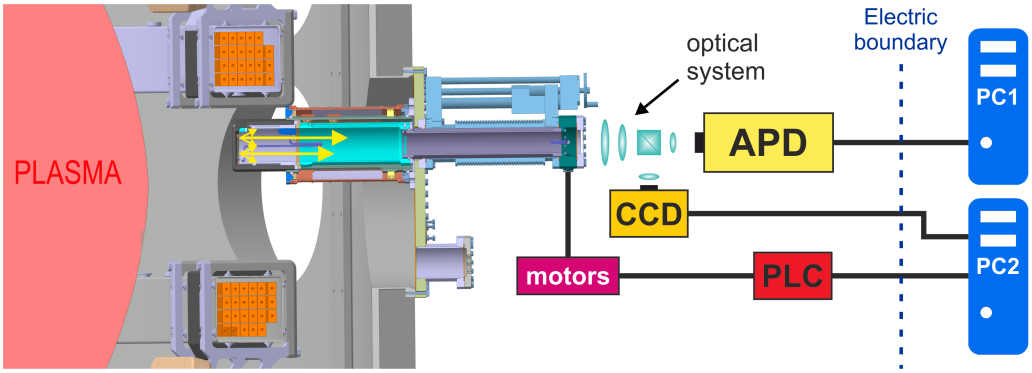

Figure 4.11: MAST-U FILD data acquisition and control system.

to detect fast-ion loss fluctuations up to the 1 MHz bandwidth of the APD camera. The P46 emits in a broad wavelength distribution within the visible spectrum, peaked at 550 ns, making it possible to use sensors in the visible range. The material has shown a very low degradation to ion fluence [195], thus providing a similar performance during long experimental periods.

An halogen lamp has been added to the probe head to light up the scintillator plate allowing to set up the cameras and calibrate the optical system. The two PCs that control and save the FILD data acquisition are placed in an electrically isolated area from the tokamak. One PC controls the APD camera and the other controls the CCD camera, the two stepper motors that drive the FILD mechanism and other auxiliary systems like the thermocouple or the halogen lamp. Electric/optical data converters are used at both ends of the isolation barrier. The FILD data acquisition layout can be seen in figure 4.11.

The absolute calibration of the MAST-U FILD is expected to be carried out in the next MAST-U opening. It is constructed using the scintillator material yield [195] and the collimator factor. It also requires to calibrate the optical system and sensors using an Ulbricht sphere [196, 197, 198]. With this, absolute measurements of the fast-ion flux, in terms of ions/s, can be provided.

Chapter 5

Experimental Results

This chapter aims to further investigate the experimental observations of ELM-induced fast-ion losses in ASDEX Upgrade, described in section 2.2.1. The aim of this chapter is to broaden the understanding of the interaction between ELMs and fast ions and provide some conclusions of the parameters that mostly affect this interaction. The investigated shots consist of lower single-null plasmas with $I_p = 800\,\mathrm{kA}$, $B_t^{axis} = 1.8 - 2.5\,\mathrm{T}$, low density ($n_e^{axis} \sim 6 \cdot 10^{19}\,\mathrm{m}^{-3}$, $T_e^{axis} \sim 5\,\mathrm{keV}$) and low collisionality ($0.4 < \nu_e^* < 1.4$) plasmas. The original shots presented in [56, 57, 58] used beams NBI7 and NBI8 to feed the FILD1 probe with passing and trapped particles, respectively. However, the most recent shots aim to populate a wider fast-ion velocity space, covering the measurable range of the entire FILD poloidal array. For this reason, a heating sequence of 0.2 s blips with NBI5, NBI6 and NBI8 is repeated during the entire shot. Additionally, 0.4 s of ICRH are added, completing a repetitive sequence of 1 s. The NBI3 is active during the entire discharge to enable FIDA/BES measurements. FIDA/BES measure the content of confined fast-ions based on charge exchange spectroscopy, using the intensity of the light emitted when a fast ion exchange charges with a neutral from NBI3. The heating scheme, which is shown in figure 5.1(a), is used in the four most recent shots dedicated to investigate ELM-induced fast-ion losses, providing a constant heating power and a varied fast-ion velocity-space distribution. The four dedicated shots, described in the following sections, aimed to investigate the resonant interaction between the ELM perturbation and the fast-ion orbits (#37700 and #37701) and to investigate the effect of varying the ELM stability with edge electron heating (#38020 and #38022).

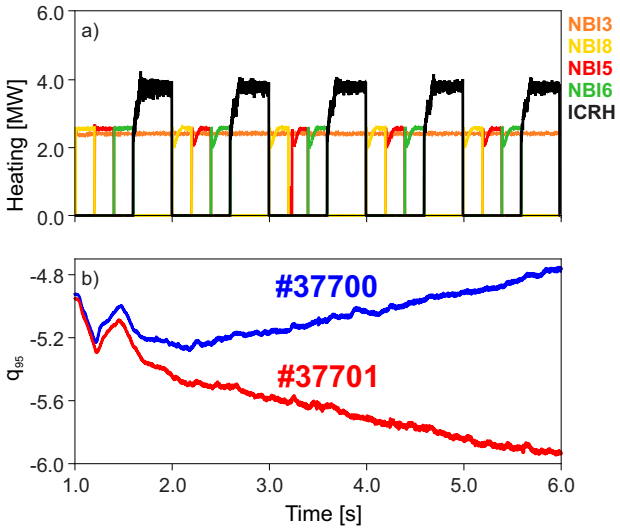

Figure 5.1: (a) Heating scheme used in discharge #37700, #37701, #38020 and #38022. (b) q_{95} scan covered in shots #37700 and #37701.

5.0.4 Scan in the Plasma Helicity

In the earliest reported shots, the accelerated distribution during the ELM perturbation in the FILD1 signal depicted a pitch-angle splitting, which was correlated with the plasma helicity [56, 57, 58]. In those shots (#34614 and #34615), a scan in the plasma q_{95}[1] depicted changes in the dominant pitch angle of the accelerated population. The affected fast ions were born in NBI7 and followed passing orbits, so it was suggested that the pitch-angle splitting was caused by a resonant interaction between the ELM perturbation and the fast-ion orbits. When the plasma q_{95} is modified, the geometrical resonances of passing particles change, as they depend on the plasma helicity [141, 142]. Consequently, the signal depicts the pitch angle of the resonant orbits for each q_{95}.

To deepen the understanding of the interaction between the fast-ion orbits and the ELM perturbation, shots #37700 and #37701 were prepared to investigate the pitch angle structure of the accelerated fast-ion losses with trapped orbits born in NBI8. An extended scan in the plasma q_{95} is performed by ramping the toroidal magnetic field from - 2.5 T to -2.25 T and from -2.5 T to -2.75 T, respectively, while keeping a constant toroidal current of 800 kA. Thus, the total q_{95} scan ranges from -4.8 to -6, as it can be observed in figure 5.1(b).

Figure 5.2(a) shows the divertor shunt current, used to monitor the ELMs,

[1]Safety factor, q, evaluated in the flux surface $\rho_{pol} = 0.95$.

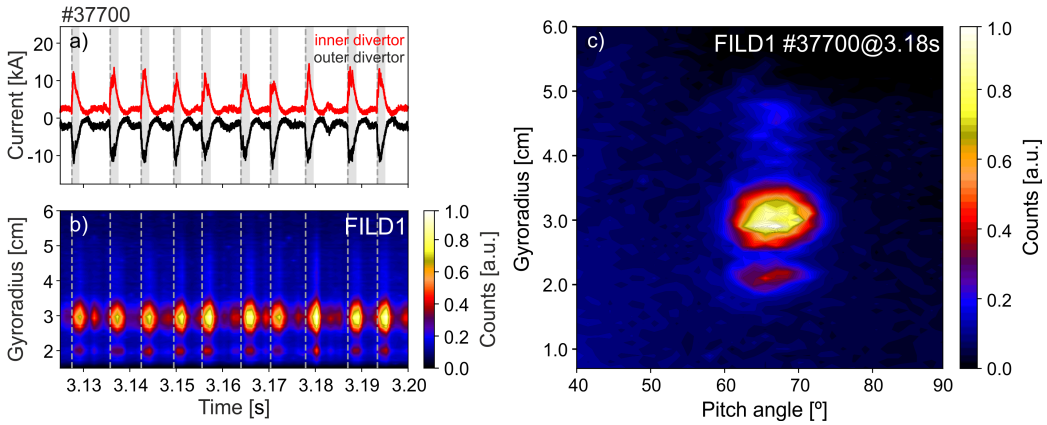

Figure 5.2: (a) Time trace of the inner and outer divertor current, used to monitor ELMs. The dashed grey lines mark the ELM onset and the shaded area mark the ELM duration. (b) Time trace of the FILD1 signal. The dashed grey lines mark the ELM onset. (c) Velocity-space of the FILD1 signal.

and figure 5.2(b) shows the gyroradius of the fast-ion losses resolved with the 1 kHz CMOS camera installed in FILD1. The vertical dashed lines mark the ELM onset, defined by the rise in the divertor current, while the shaded areas mark the ELM duration. The gyroradii above the injection energy can be observed to be well correlated with the ELM onset in figure 5.2(b), evidencing an ELM-induced accelerated population. Although the distribution is distorted due to the collimator finite resolution, the accelerated population is localized 1.5 cm ($\sim$ 60 keV) above the injection energy, as it can be observed in figure 5.2(c). No pitch-angle splitting was observed on the trapped particles signal during the q_{95} scans. Conversely, the accelerated population depicted a pitch angle centred with respect to the NBI prompt losses during the entire experiments. It must be noted that trapped orbits have geometrical resonances which are broader in phase space and do not depend on the plasma q. Thus, the absence of a pitch angle splitting on trapped orbits supports the hypothesis of a resonant interaction between the fast ions and the ELM perturbation.

5.0.5 Scan in Edge Electron Heating

Recent experiments have used ECRH applied on the edge to modify the pedestal pressure and current density profile, with the aim to test the peeling-balooning model [199, 200, 201]. In those experiments, the ECRH power was gradually directed from the plasma core up to $\rho_{pol} = 0.9$. It was observed,

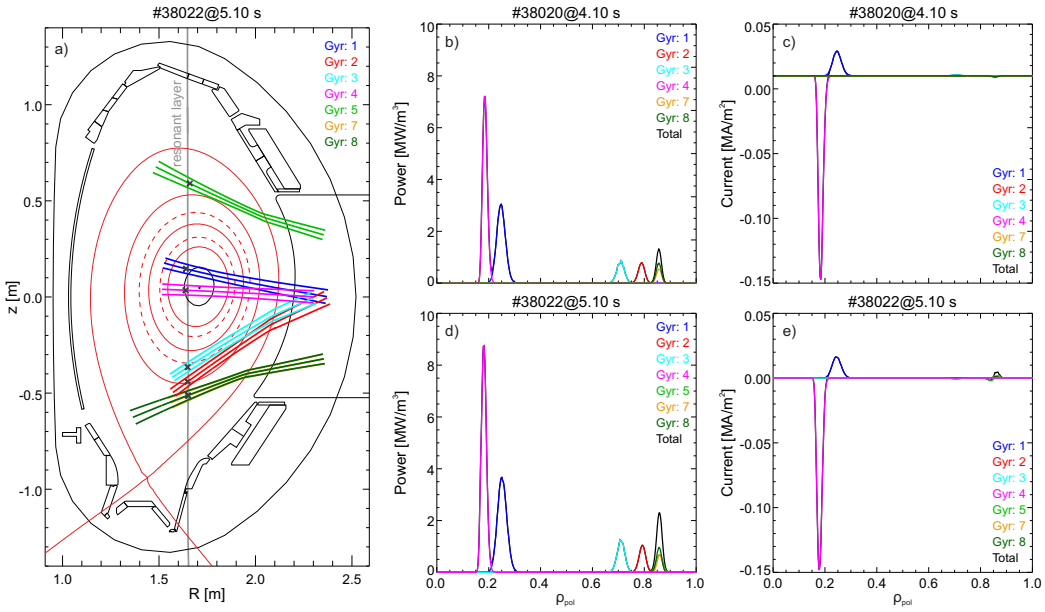

Figure 5.3: (a) Poloidal view of the EC waves from the different ECRH launchers. (b) Profile of the ECRH power deposition in shot #38020. (c) Current drive profile in shot #38020. (d) Profile of the ECRH power deposition in shot #38022. (e) Current drive profile in shot #38022.

that when the ECRH heating was directed towards the edge, the ELM repetition frequency increased above the values foreseen by the peeling-ballooning model. The ECRH waves can be oriented making use of their movable mirrors, whose toroidal and poloidal angles can be resolved with the TORBEAM code [202]. TORBEAM is a beam tracing code for electron-cyclotron (EC) waves that resolves the propagation and absorption of the wave in the plasma. It calculates the position and profiles of deposited power and current driven given a resonant layer, whose position depends on the plasma magnetic field, as the resonant condition occurs when the wave frequency matches the electron cyclotron frequency $\omega_e = \frac{eB}{m_e}$.

Motivated by the aforementioned results, two dedicated shots are designed to investigate the effect of ELM stability on the ELM-induced fast-ion losses. In these shots, a scan in the edge ECRH power is performed by sequentially starting the 8 ECRH launchers in steps of 1 s, matching the repetitive heating sequence in figure 5.1(a). Gyrotrons 1 and 4 were pointing toward the plasma core and were active during the entire shot to avoid impurity accumulation that would destabilize the plasma. The orientation of the remaining gyrotrons was optimized with TORBEAM to concentrate

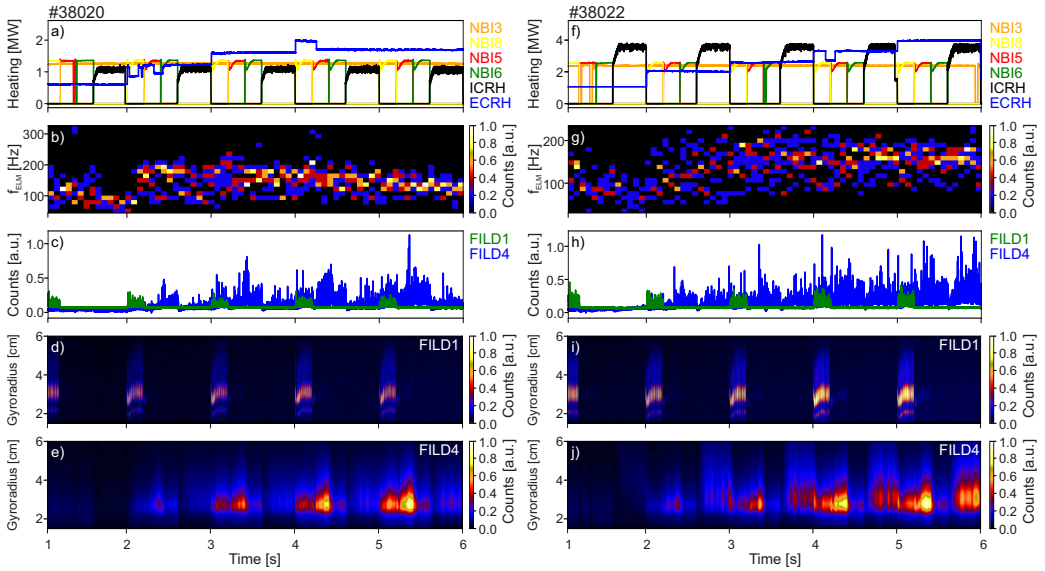

Figure 5.4: (a, f) External heating, (b, g) ELM repetition frequency, (c, h) time traces of FILD1 and FILD4, (d, i) histogram of FILD1 and (e, j) histogram of FILD4 in shots #38020 and #38022, respectively.

the power deposition within $\rho_{pol} = [0.8, 0.9]$. Besides, the toroidal angles of the edge gyrotrons were set to minimize the current driven in shot #38020 and maximize it in shot #38022. Yet, a fault in the mirror actuators slightly mismatched the desired configuration. The actual power and current deposition is simulated with TORBEAM and shown in figure 5.3, where it can be observed that the ECRH heating was deposited in a broader edge region ($\rho_{pol} = [0.65, 0.9]$) and the edge current drive in shot #38022 was drastically reduced. Moreover, gyrotron 6 was not available and gyrotron 5 failed during shot #38020. This reduced the maximum achieved ECRH power, reaching 2 MW in shot #38020 and 4 MW in shot #38022, as it can be observed in figures 5.4(a) and 5.4(f). The first edge gyrotron is started at $t = 2\,\mathrm{s}$. This caused a drastic increase in the ELM repetition frequency from 100 Hz to 200 Hz, as it can be observed in figure 5.4(b) and 5.4(g). Afterwards, the ELM repetition frequency remains stable and it even decreases at the latest stage of the discharge, when the edge ECRH power is maximum. This suggests that a small amount of edge ECRH power is sufficient to observe the reported changes in the ELM frequency while higher ECRH power does not cause any further effect.

The FILD signals, shown in figures 5.4(c) and 5.4(h), follow a gradual growth during the shots which drastically increases during the ELMs, especially in FILD4, suggesting that the ELM-induced fast-ion losses scale up

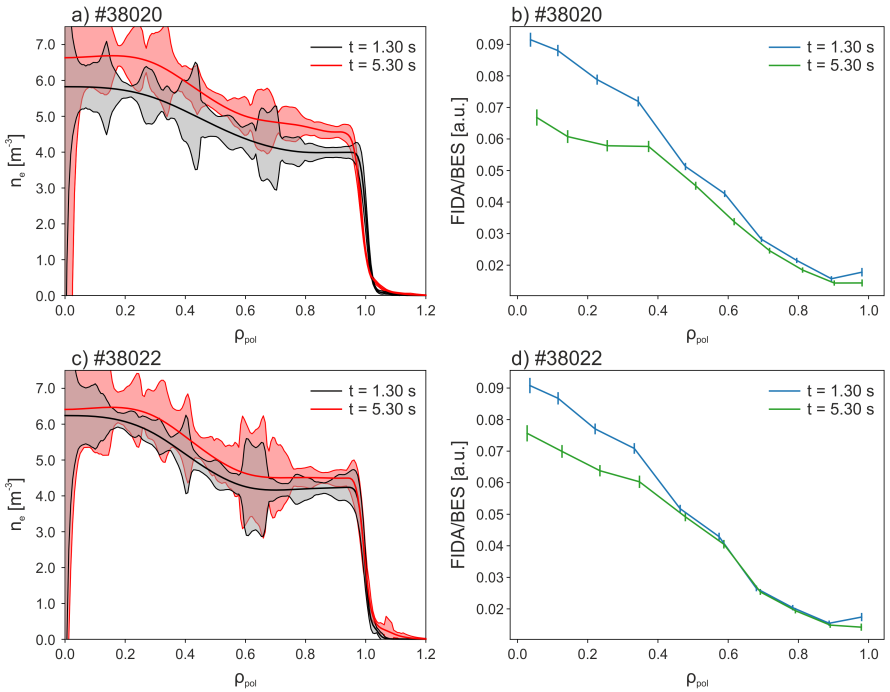

Figure 5.5: (a, c) Density profiles and (b, d) FIDA emission in shot #38020 and #38022, respectively.

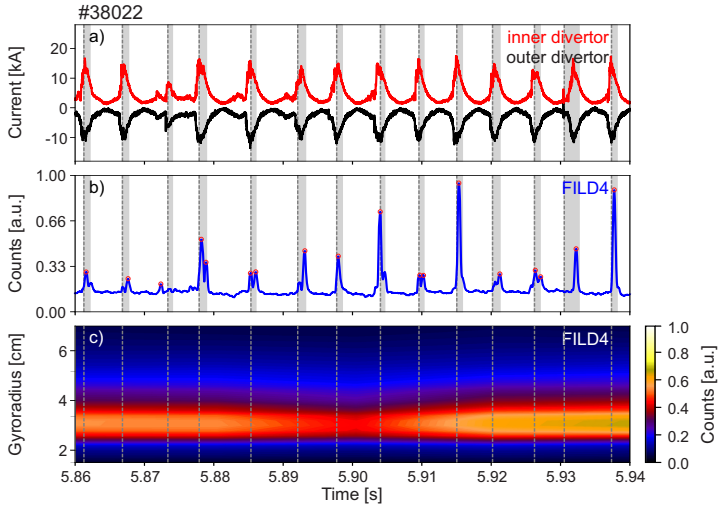

Figure 5.6: (a) Time trace of the inner and outer divertor current, (b) time trace of FILD4 and (c) histogram of FILD4 during an ICRH phase in shot #38022. The dashed lines mark the ELM onset and the shaded area mark the ELM duration. The red circles in (b) mark the detected peaks of fast-ion losses correlated with the ELM activity.

with the edge ECRH power. The enhancement of the fast-ion losses is caused by a gradual increase of the density profile during the shots, as it is shown in figures 5.5(a) and 5.5(c). The increased density alters the fast-ion deposition profile, reducing the fast-ion content on the core, as it can be observed in the FIDA emission (figures 5.5(b) and 5.5(d)), which can be correlated with the fast-ion content at the given poloidal coordinate. Consequently, a larger fast-ion population is expected to concentrate in the edge, available to interact with the ELM stability. As a matter of fact, the FIDA emission does not reveal a higher fast-ion content in the plasma edge, what suggests that the fast ions are being expelled. This is in line with the enhancement in the FILD signal. Therefore, an increase in the plasma density leads to more fast ions in the edge which ultimately results in larger ELM-induced fast-ion losses. The results motivate further investigations of the interaction between fast ions and ELMs using ELM pacing techniques that, in turn, enhance the plasma density, such as gas puffing [200] or pellet injection [203]. The enhancement of the ELM-induced fast-ion losses makes it possible to observe peaks correlated with the ELM activity from all the employed NBI sources, thus suggesting that the ELM enhances fast-ion losses in a wide range of velocity-space distributions. Besides, an enhancement of the fast-ion losses clearly correlated with the ELM onset can be observed during the ICRH phase in FILD4, as it is shown in figure 5.6(b). This suggests that the ELM activity also enhance the losses of ICRH fast ions. Nonetheless, the velocity-space of these losses cannot be distinguished, as it is illustrated in figure 5.6(c), because the 60 Hz CCD camera installed in FILD4 does not offer enough temporal resolution to resolve the intra-ELM velocity space of the fast-ion losses. Nonetheless the 64 px sensor of the APD camera reveals that the ELM-induced losses are localized in phase-space.

5.0.6 Statistical Analysis

Since the ELMs are quasi-periodic fluctuations with typical repetitive frequencies of $\sim$ 100 Hz, the number of ELMs during a 6 s discharge is enough to perform a statistical analysis of the FILD signal induced by ELMs. This makes it possible to achieve a more general understanding of the ELM-induced fast-ion losses and find the parameters that most strongly affect them. A dataset of AUG H-mode discharges with FILD data has been constructed, covering the original shots in reference [56, 57, 58], some shots dedicated to ELM mitigation with RMPs and the latest shots dedicated to the investigation of ELM-induced fast-ion losses presented in the previous sections. An overview of the included shots is given in table 5.1.

An algorithm has been developed to detect the several peaks appearing in

Shot	B_t^{axis} (T)	I_p (MA)	NBI	ICRH	RMP	FILD
33127	-1.8	0.8	3, 7, 8	Off	On	1, 2
34540	-1.8	0.9	3, 6, 7	Off	On	1, 2, 5
34584	-1.8	0.8	2, 3, 4, 7, 8	Off	On	1, 2
34587	-1.8	0.8	2, 3, 4, 7, 8	Off	On	1, 2
34597	-1.8	0.8	2, 3, 7, 8	Off	On	1, 2, 5
34598	-1.8	0.8	2, 3, 7, 8	Off	On	1, 2, 5
34599	-1.8	0.8	2, 3, 7, 8	Off	On	1, 2, 5
34601	-1.8	0.8	2, 3, 4, 7, 8	Off	On	1, 2, 5
34614	-1.9	0.8	3, 4, 7, 8	Off	Off	1, 2, 5
34615	-2.5	0.8	3, 4, 7, 8	Off	Off	1, 2, 5
37700	-2.5	0.8	3, 5, 6, 8	On	Off	1, 2, 4, 5
37701	-2.5	0.8	3, 5, 6, 8	On	Off	1, 2, 4, 5
38020	-2.5	0.8	3, 5, 6, 8	On	Off	1, 2, 4
38022	-2.5	0.8	3, 5, 6, 8	On	Off	1, 2, 4

Table 5.1: Main parameters of the AUG shots included in the dataset.

the FILD signal correlated with the ELM activity, which are marked in red in figure 5.6(b). The algorithm stores the peaks above a certain threshold and prominence, whose limits are optimized with a convergence test. Additional information related to the FILD peaks are also stored, such as the relative time to the nearest ELM onset, the number of peaks per ELM or their relative amplitude. The ELM magnetic perturbation is analysed with a tool that calculates the magnetic spectrograms and the perturbation toroidal mode number synchronized with the ELM onset [79]. An histogram of the peaks relative amplitude synchronized with the ELM onset is shown in figure 5.7(a) and compared against an ELM-synchronized spectrogram of the magnetic perturbations in figure 5.7(b). The FILD histogram is also shown in figure 5.7(b) for comparison. It can be observed that the largest peaks occur right after the ELM onset, in line with the highest magnetic perturbation. In fact, 70% of the total peaks in the FILD signal occur during the ELM crash. This suggests that ELM precursors [204, 205] have a rather low effect on the ELM-induced fast-ion losses in comparison to the ELM crash.

A more general comparison between the FILD signal and other ELM-relevant parameters was carried out, such as the pedestal pressure and density, the ELM toroidal mode numbers or the ELM repetition frequency, among others. A clear correlation between the amplitude of the divertor current and the amplitude of the FILD peaks is revealed, as it can be observed in figure 5.7(c). The correlation is observed with several NBI sources.

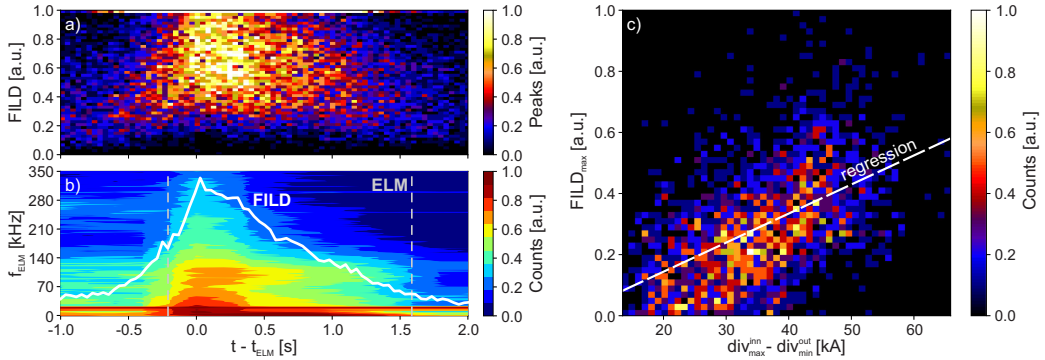

Figure 5.7: (a) Histogram of the FILD peaks and (b) spectrogram of the magnetic perturbation synchronized with the ELM onset. The ELM crash is marked with the grey dashed lines. The FILD histogram is shown in white. (c) Histogram of the maximum divertor current and maximum FILD amplitude of each ELM. The linear regression is shown with a white dashed line.

The same scale is observed between the FILD amplitude and the amplitude of the magnetic perturbation in the pick-up coils. This suggests that the ELM-induced fast-ion losses scale with the thermal particle losses during the ELM crash, through a common transport mechanisms closely related with the magnetic perturbation. The statistical analysis can be extended, adding more shots with FILD data to the dataset. Also, future experiments in other devices, like MAST-U or TCV, could be added. This will enable further analyses of ELM-synchronized FILD data and comparisons with multi-machine ELM parameters. Ultimately, it is envisaged to perform a scalability diagram that will enable to estimate the ELM-induced fast-ion losses in future fusion reactors.

Chapter 6

Numerical Results

The modelling addressed here follows three different objectives. The simulations in AUG aim to reproduce and understand the main experimental observations of fast-ion losses induced by ELMs, presented in section 2.2.1. The MAST-U simulations aim firstly to produce a synthetic FILD signal for a MAST-U baseline scenario, in preparation for the diagnostic commissioning during the experimental campaign. Then, the ELM-induced fast-ion transport and acceleration is modelled in MAST-U with the aim to compare the results with the AUG observations.

6.1 ELM-induced Fast-ion Transport and Acceleration in AUG

The AUG plasma is modelled with MEGA, described in section 3.1.3, with the aim to obtain the resulting electromagnetic perturbation during an ELM. This perturbation will be employed in ASCOT as an input to study the ELM-induced fast-ion transport and acceleration. The MEGA simulation is carried out under studies of the fast-ion kinetic effects on ELM stability [206, 207]. However, as this simulation seeks the electromagnetic perturbation during an ELM uncoupled from the fast-ions, their kinetic effect on the MHD equations is disabled in MEGA. The model is based on the AUG discharge #33616, a similar discharge in plasma shape and parameters to those discussed in chapter 5. It is based on a lower single-null plasma with $I_p = 800\,\mathrm{kA}$, $B_t^{axis} = 2.5\,\mathrm{T}$, $n_e^{axis} = 7.5 \cdot 10^{19}\,\mathrm{m}^{-3}$, $T_e^{axis} = 6.6\,\mathrm{keV}$. The plasma resistivity in the simulation is set to $\eta = 10^{-5}\,\Omega\mathrm{m}$, two orders of magnitiude above the Spitzer value at the edge. The simulation domain is limited to $\rho_{pol} \leq 1.07$ to avoid the growth of instabilities out of the plasma. Nonetheless, this limit is wide enough to cover the SOL up to the first wall.

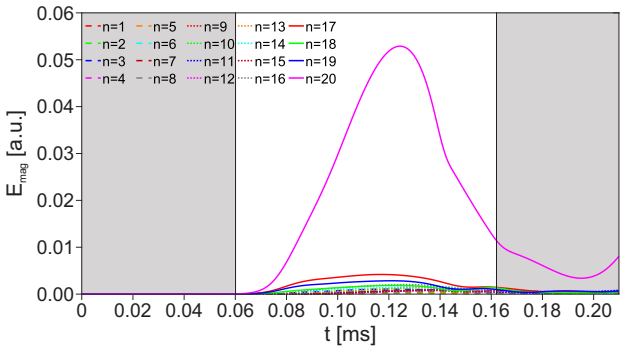

Figure 6.1: Magnetic energy of the perturbation decomposed in toroidal mode numbers.

The simulation in MEGA begins from an equilibrium state, where the initial MHD force is balanced. Then, an initial perturbation is applied in the form of a $\nabla \times \boldsymbol{B}$ perturbation localized at the edge ($0.90 < \rho_{pol} < 1.05$). The result successfully reproduces a high n ballooning mode, with a fast growth of low n modes due to non-linear coupling. It results in the relaxation of the pressure gradient and a filamentary structure of the electromagnetic perturbation, thus mimicking the main features of an ELM [46]. The perturbation is dominantly $n = 20$, as it can be observed in figure 6.1. This is well above the dominant $n = 3$ and $n = 5$ observed experimentally [79]. Besides, the growth rate of the perturbation is $\gamma = 10^5\,\mathrm{s}^{-1}$, an order of magnitude above that observed experimentally [80]. These two differences should be addressed in a comparison between the numerical and experimental results. The electric perturbation can be derived from the Ohm's law:

$$\boldsymbol{E} = -\boldsymbol{v} \times \boldsymbol{B} + \eta \boldsymbol{J} + \frac{1}{e n_e} \left(\boldsymbol{J} \times \boldsymbol{B} - \nabla p_e \right) - \frac{m_e}{e} \frac{d \boldsymbol{u}_e}{dt} \tag{6.1}$$

which in MEGA it is computed as:

$$\boldsymbol{E} = -\boldsymbol{v} \times \boldsymbol{B} + \eta \left(\boldsymbol{J} - \boldsymbol{J}_{eq} \right) \tag{6.2}$$

where η is the plasma resistivity, $\boldsymbol{J}$ is the plasma current density and $\boldsymbol{J}_{eq}$ is the plasma current density at the equilibrium. Thus, MEGA neglects the electrons inertia, the Hall and the diamagnetic effects in the resolution of the electric perturbation. The latter is believed to be important in the stabilization of high n modes and to reduce the overall growth rate [208] due to the stabilizing effect of the associated radial electric field, E_r [209, 210]. This may explain the two main discrepancies between the MEGA results and the experiments. Nonetheless, the Ohm's law in MEGA accounts for the

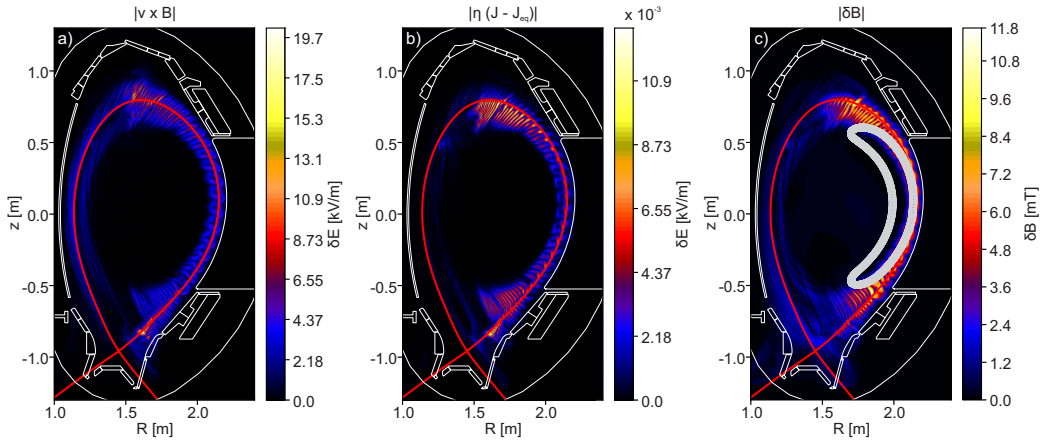

Figure 6.2: (a) $\boldsymbol{v} \times \boldsymbol{B}$ term of the electric perturbation. (b) Resistive term of the electric perturbation. (c) Magnetic field perturbation and fast-ion orbit.

resistive process during the magnetic reconnection, whose parallel electric field is believed to cause the fast-ion acceleration during an ELM [56, 57, 58]. Conversely, the results have shown that the $\boldsymbol{v} \times \boldsymbol{B}$ term is dominant with respect to the resistive term, as it can be observed in figure 6.2(a) and 6.2(b). As a result, the electric perturbation resulting from the MEGA code is mainly perpendicular to the magnetic field.

The electromagnetic perturbation ($\delta\mathbf{B}$, $\delta\mathbf{E}$) from MEGA is given as an input to ASCOT, using a grid in temporal-cylindrical coordinates (R, φ, z, t), as it is described in section 3.2.2. The fast-ion transport and acceleration during the ELM perturbation is assessed by tracking the constants of motion and adiabatic invariant introduced in section 2.1.5, where the variation of the toroidal canonical momentum (ΔP_φ) is associated with the particle radial transport, the variation of the kinetic energy (ΔT) is implicitly associated with the particle acceleration and the variation of the magnetic moment ($\Delta\mu$) is associated with a variation of the perpendicular velocity in the cyclotron time scale. To explore the fast-ion behaviour, a set of markers is used as a representation of the particle phase-space. The markers are distributed in a grid with initial conditions $\varphi = 0$, $z = 0$, $T = 80\,\text{keV}$ and ranged over the initial radial position, $R = [1.90, 2.20]$ m, and the initial pitch angle, $\Lambda = [-1.0, -0.2]$. The markers are followed during 10 poloidal turns, proven sufficient to reveal the transport and acceleration patterns. The variation of the toroidal canonical momentum, the kinetic energy and the magnetic moment of the markers are shown in figures 6.3(a), 6.3(b) and 6.3(c), respectively. The figures show that the particle transport and acceleration are localized at the edge, from $R = 2.05\,\text{m}$ ($\rho_{pol} = 0.85$) and beyond the separa-

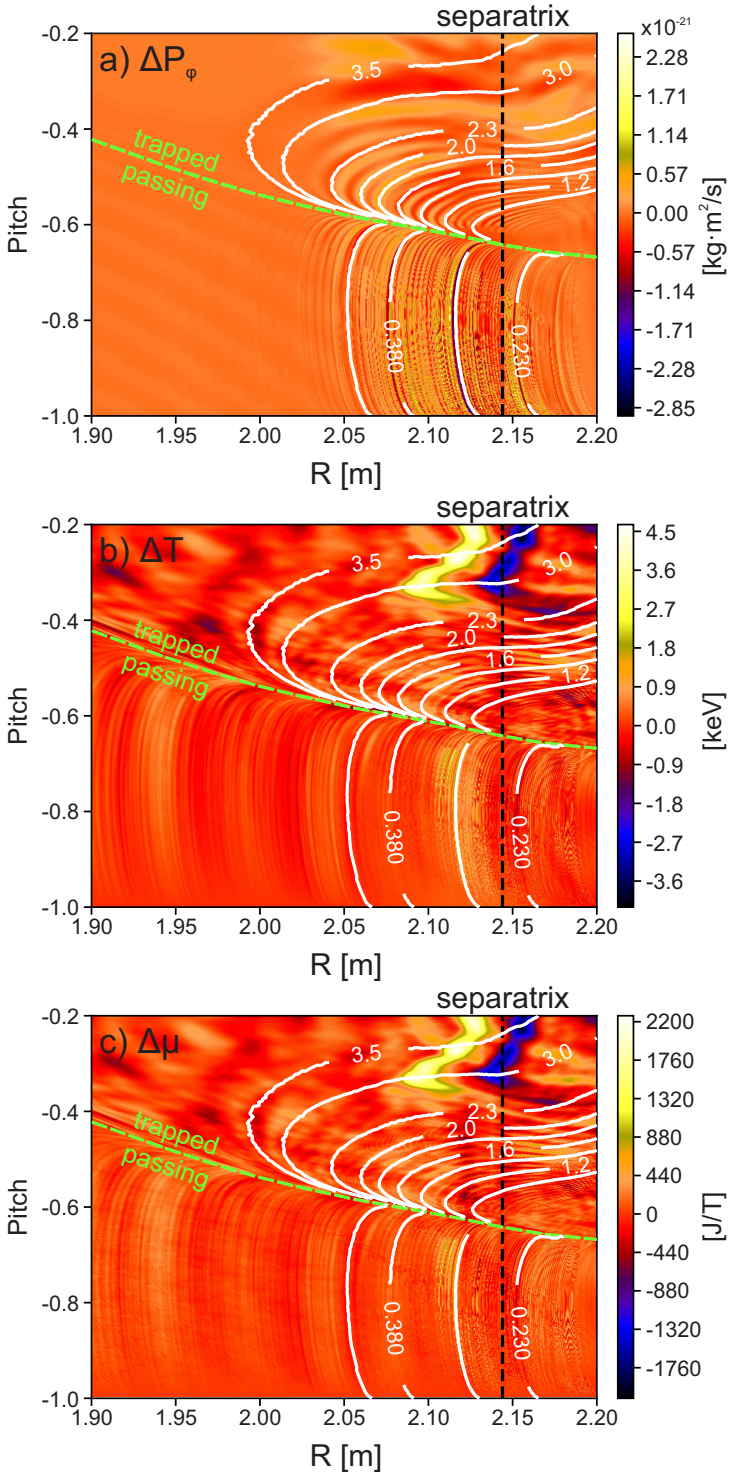

Figure 6.3: (a) Variation of the toroidal canonical momentum and $\omega_{pol}/\omega_{tor}$ contour lines. (b) Variation of the kinetic energy and $\omega_{pol}/\omega_{tor}$ contour lines. (c) Variation of the magnetic moment and $\omega_{pol}/\omega_{tor}$ contour lines.

trix, where the electromagnetic perturbation is stronger. Besides, it can be seen that the transport and acceleration does not reveal the same patterns in the phase-space. This indicates that the transport and the acceleration are decoupled, being $\delta\mathbf{B}$ the dominant responsible for the particle transport and $\delta\mathbf{E}$ the dominant responsible for the acceleration, independently. As a consequence, particles with both transport and acceleration will occur in the narrow phase-space regions where the two effects overlap.

To evaluate a resonant interaction, the orbits resonance condition is expressed in terms of the fraction $\omega_{pol}/\omega_{tor}$, having different expressions depending on the orbit nature [141, 142]. As an example, for an electromagnetic perturbation with a toroidal mode number n, the linear resonance condition of a trapped orbit is:

$$\frac{\omega_{pol}}{\omega_{tor}} = \frac{n}{p} \tag{6.3}$$

where ω_{pol} is the orbit poloidal frequency, ω_{tor} is the orbit precession frequency and p is the bounce harmonic, an arbitrary integer. A clear correlation between the high $|\Delta P_\varphi|$ lines and the $\omega_{pol}/\omega_{tor}$ contour lines can be observed in figure 6.3(a). This clearly suggests a resonant interaction between the fast-ion orbits and the magnetic perturbation, which produces the fast-ion transport. The patterns in figures 6.3(b) and 6.3(c) do not follow the $\omega_{pol}/\omega_{tor}$ contour lines. Nonetheless, they are analogous to each other, depicting that the energy variation is associated with a variation of the perpendicular velocity component in the cyclotron time scale. It can be demonstrated that the energy variation is mainly produced by the $\boldsymbol{v} \times \boldsymbol{B}$ term of the electric field, while the resistive term has a negligible effect. Thus, the fast-ion acceleration is caused by the enhanced transport during the ELM, which produces high electric fields in the plasma edge, as it is shown in figure 6.4(a). Due to the high electric field gradients in the scale of the fast-ion gyroradii, the conservation of the magnetic moment is lost, thus producing a net energy variation. Figure 6.4(b) shows the energy variation of a set of markers distributed with $z = 0$, $\varphi = 0$, $\Lambda = -0.3$ and ranged over the initial radial position, $R = [1.90, 2.20]$ m, and the initial energy, $T = [30, 150]$ keV. Lines of high energy variation can be observed, highlighting the phase-space where this effect occurs resonantly. The lines extend toward energies above 60 keV, which suggests that particles can resonantly increase their energy for a few tens of keV, while they cannot lose energy below 60 keV. In addition to the variation in the constants of motion, a poloidal Poincaré plot has been made. The Poincaré plot depicts the intersections of the magnetic field lines with a poloidal angle ($\varphi = 0$). Thus, the Poincaré plots can reveal structures such as magnetic islands or chaotic field lines [211]. Figure 6.5 shows the resulting Poincaré plot of the ELM perturbation, where it can be observed

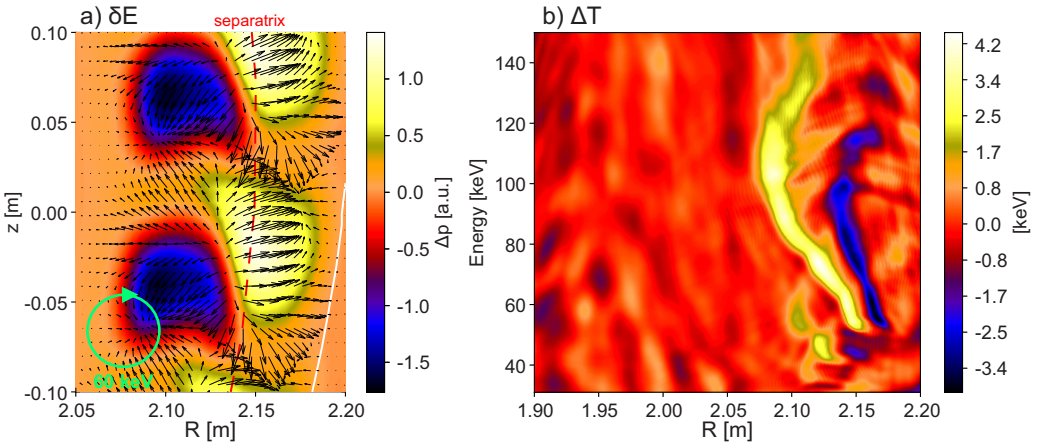

Figure 6.4: (a) Poloidal $\delta\boldsymbol{E}$ vector field. (b) Variation of the kinetic energy in a $R-T$ grid.

that magnetic field lines become chaotic beyond $\rho_{pol} > 0.81$. Thus, besides the discussed transport and acceleration mechanisms, particle transport is also affected by the chaotic field lines beyond $\rho_{pol} > 0.81$. The chaotic effect is mostly visible in the passing region of figure 6.3(a), breaking the lines of high $|\Delta P_\varphi|$.

The results above foresee a maximum fast-ion acceleration of 4.5 keV per 10 poloidal turns. Considering that the orbital time scale ranges between 3 - 8 μs, the necessary time to accelerate fast ions over 50 keV is in the order of the ms. However, the duration of the MEGA simulation, marked by the unshaded region in figure 6.1, is only 0.1 ms. No wonder, the growth rate in MEGA is an order of magnitude higher than the observed experimentally. Consequently, the duration of the MEGA perturbation has been artificially extended up to 1 ms with the aim to observe relevant fast-ion acceleration. This effectively reduces the growth rate to $\gamma = 10^4\,\mathrm{s}^{-1}$. In turn, since the growth rate is proportional to the plasma resistivity ($\gamma \propto \eta^{1/3}$) [212], it must be noted that the resistive effects will be overestimated in the results. Nonetheless, it has been discussed already that its effects are negligible in the fast-ion transport and acceleration.

The transport and acceleration of the NBI-born fast-ion distribution in AUG are assessed by modelling the 8 beams with BBNBI, using the updated data from the beam calibration in 2017. BBNBI produces a distribution of 6 million markers for each beam, that will be treated in ASCOT independently. The markers are first tracked in an unperturbed field to filter out the NBI prompt losses. Then, the orbits of the confined fast ions are tracked during the ELM perturbation. Table 6.1 shows the fraction of the

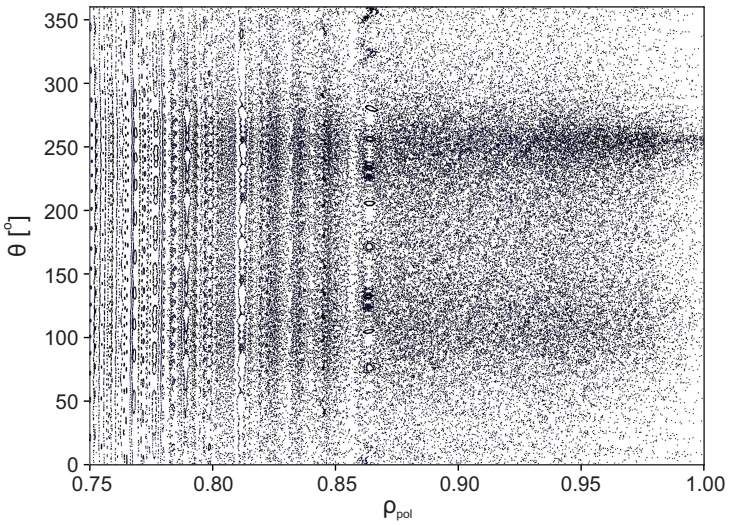

Figure 6.5: Poloidal Poincaré map of the perturbed magnetic field lines during the ELM.

NBI#	1	2	3	4	5	6	7	8
% ELM losses	0.24	0.27	0.31	0.24	0.36	0.63	0.59	0.36
Λ_{main}	-0.2	-0.4	-0.45	-0.25	-0.35	-0.55	-0.7	-0.45

Table 6.1: Fraction of lost fast ions during an ELM and main pitch angle of the NBI distribution of each beam.

fast-ion distribution lost during the ELM perturbation. In total, a 0.37% of the fast ions are lost during the ELM. The patterns of the ELM-induced losses on the AUG wall are shown in figure 6.6(a). It can be observed that the ELM-induced losses are concentrated on the limiters at the LFS and the FILD probes. Simulations carried out with an axisymmetric wall, thus removing the protruding elements, show that the ELM-induced losses, follow the high-n, field-aligned patterns of the ELM perturbation, as it can be observed in figure 6.6(b). This illustrates the strong impact of the ballooning perturbation on the fast-ion confinement. Table 6.1 also shows the main pitch angle of the beams, – i.e., the pitch angle corresponding to the maximum of the fast-ion distribution –. The beams with pitch angles near the high ΔT regions in figure 6.3(b), – i.e., NBI1 and NBI4 –, depict a fast-ion energy distribution that spreads over high energies during the ELM, forming a local maximum at 30 keV above the injection energy, as it can be observed in figure 6.7. As a result, an accelerated population can be distinguished. The velocity space of the fast ions colliding with the FILD probes can be

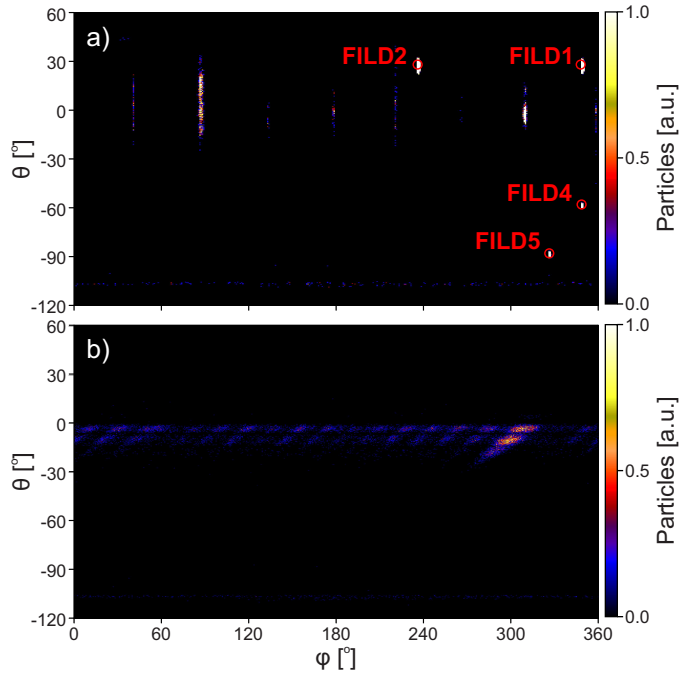

Figure 6.6: ELM-induced fast-ion losses on the AUG 3D wall (a) and 2D wall (b) projected in the toroidal and poloidal angles.

used as an estimate of the FILD signal. Figure 6.8 shows the velocity space of the NBI1 and NBI4 distributions colliding with FILD1 and FILD2. A high energy component, 40 keV above the injection energy, that converges to a narrow pitch angle range, can be observed in the velocity space of the fast ions impinging on FILD1 and FILD2. This high-energy feature is only observed with the distributions from NBI1 and NBI4, since the accelerated population is larger in these distributions, as it was discussed before. The high energy feature is not observed in FILD3, FILD4 or FILD5. This might be explained by the strong effect of the ballooning perturbation, as it was mentioned before, expelling fast ions near the midplane, where only FILD1 and FILD2 are located.

6.2 FILD Signal for the MAST-U Baseline Scenario

The numerical models described in section 3.1 are used to estimate the FILD signal in a MAST-U baseline scenario [213]. BBNBI calculates the NBI ionization profile that is then traced with the ASCOT code. Subsequently,

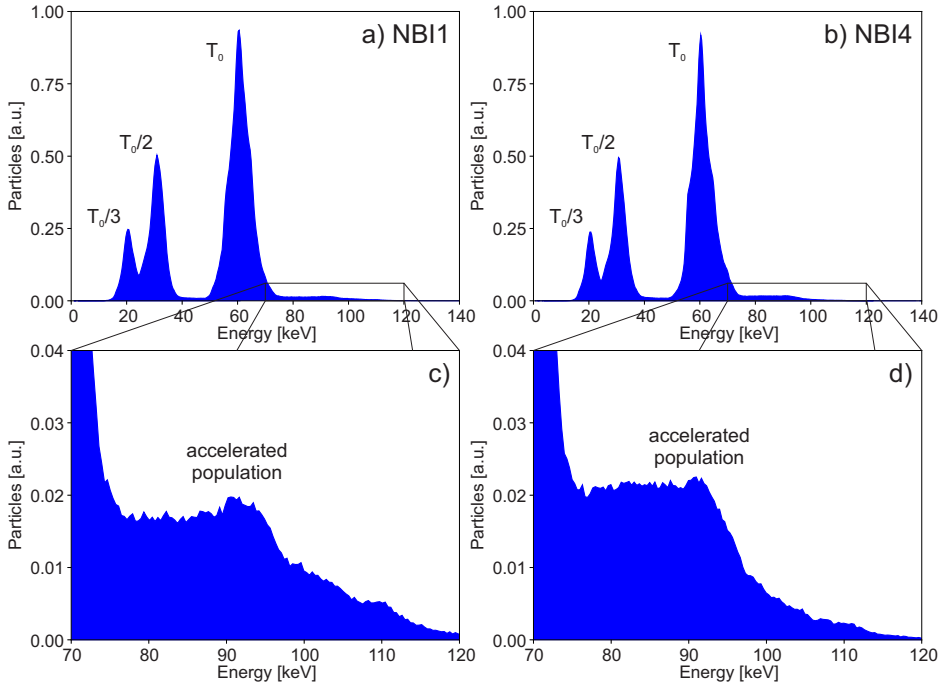

Figure 6.7: (a, b) Energy distribution of NBI1 and NBI4 after the ELM perturbation. (c, d) Magnification of the NBI distributions, where an accelerated population can be seen.

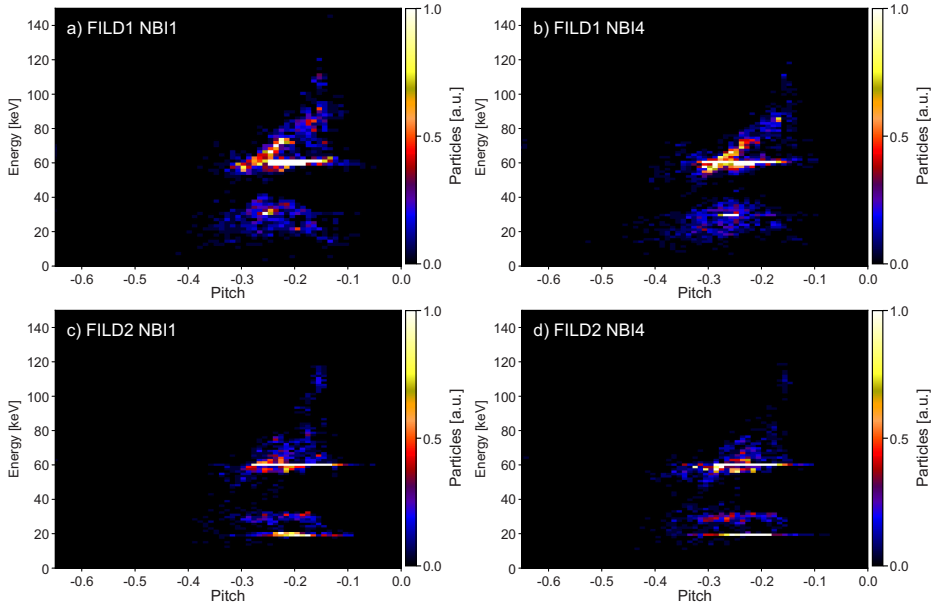

Figure 6.8: Velocity space distribution of the ELM-induced fast-ion losses reaching FILD1 and FILD2 from NBI1 and NBI4.

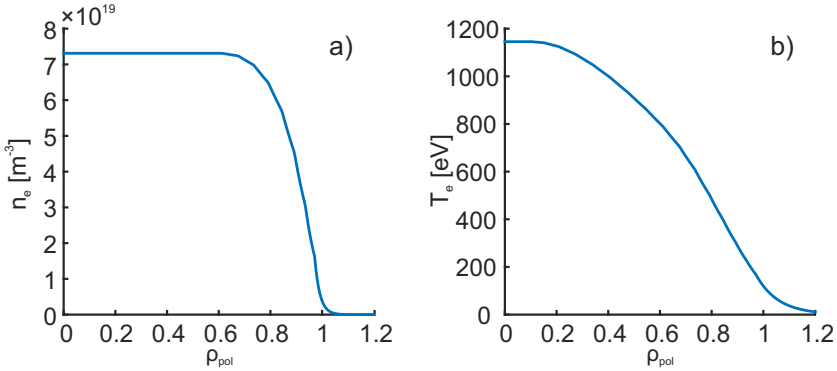

Figure 6.9: Electron density (a) and temperature (b) profiles for the MAST-U baseline scenario.

the fast-ion distribution that collides with the FILD probe is computed by FILDSIM, which creates a synthetic frame of the FILD plate. The baseline scenario consists of a MHD-quiescent plasma with a conventional double-null divertor configuration. The plasma current and toroidal magnetic field are $I_p = 2\,\text{MA}$, $B_t = 0.75\,\text{T}$ at the magnetic axis. The target kinetic profiles can be observed in figure 6.9 and the plasma shape is shown in figure 6.10(a).

The MAST-U NBI ionization profile is modelled with BBNBI. The NBI main injection energy is 75 keV. The 2.5 MW power of each NBI is injected in a proportion of 62 % at the main energy, 27 % at the half energy (37.5 keV) and 11 % at the third energy (25 keV). The MAST-U beamlines have been implemented in BBNBI based on the construction models, whose poloidal and toroidal geometries can be observed in figure 6.10(a) and 6.10(b), respectively. The on-axis NBI (South, SS) is placed on the midplane ($z = 0\,\text{mm}$) and the off-axis NBI (South-West, SW) is placed at $z = 650\,\text{mm}$ above the midplane, both with horizontal beamlines. The NBI beamlets are evenly distributed in a diamond-shaped rectangular grid with an horizontal focal length of 14 m and a vertical focal length of 6 m. The beamlets divergence is 0.6°. Figures 6.10(a) and 6.10(b) show the estimated beam deposition of the SS and the SW NBI. Figure 6.10(c) illustrates the ionization profile of each injector as a function of the radial coordinate ρ_{pol}. It can be observed that the off-axis injector increases the fast-ion density at the edge of the plasma ($\rho_{pol} > 0.6$) while the on-axis injector provides a more evenly distributed ionization profile up to the plasma core. The fraction of neutrals that goes through the plasma without ionizing, so-called shine-through, is estimated to be 695 W from the SS injector and 7120 W from the SW injector. Therefore, the shine-through power is a 0.16 % of the total injected power, suggesting a good NBI absorption. The shine-through creates hot spots on the tokamak

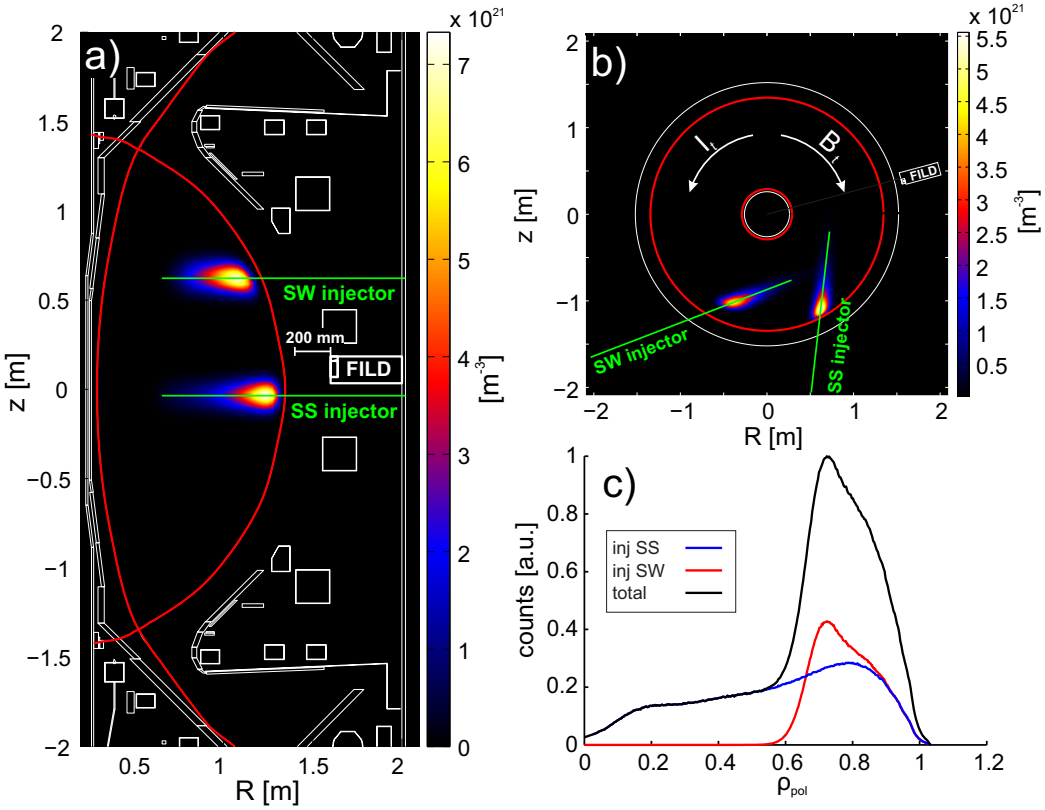

Figure 6.10: (a) Poloidal and (b) toroidal cross-section of the beam deposition in MAST-U. NBI beamlines are marked in green. (c) Densities of ionized beam neutrals from the on-axis (blue) and the off-axis (red) NBI and total fast-ion profile (black).

wall, mainly in sector 2 and the upper part of sector 4, as it is shown in figure 6.11(a), where further reinforcements are installed to guarantee the vessel integrity. It can be observed that FILD is out of the range of the hot spots.

BBNBI produces an ensemble of 5 million test particles following the distributions in figure 6.10. The particle orbits are traced with ASCOT, using the baseline magnetic field and a 3D model of the tokamak wall, including the FILD probe. The particles are followed for 10^{-4} s. If the test particle does not collide with the wall during this period, the particle is considered confined. The distribution of lost particles allows to estimate the power load on the wall. The simulation is repeated for different FILD radial positions along its operating range, $R = [1.40, 1.60]$ m. It is observed that FILD intersects fast-ion orbits in a range between $[1.40, 1.50]$ m, thus suggesting a wide operating

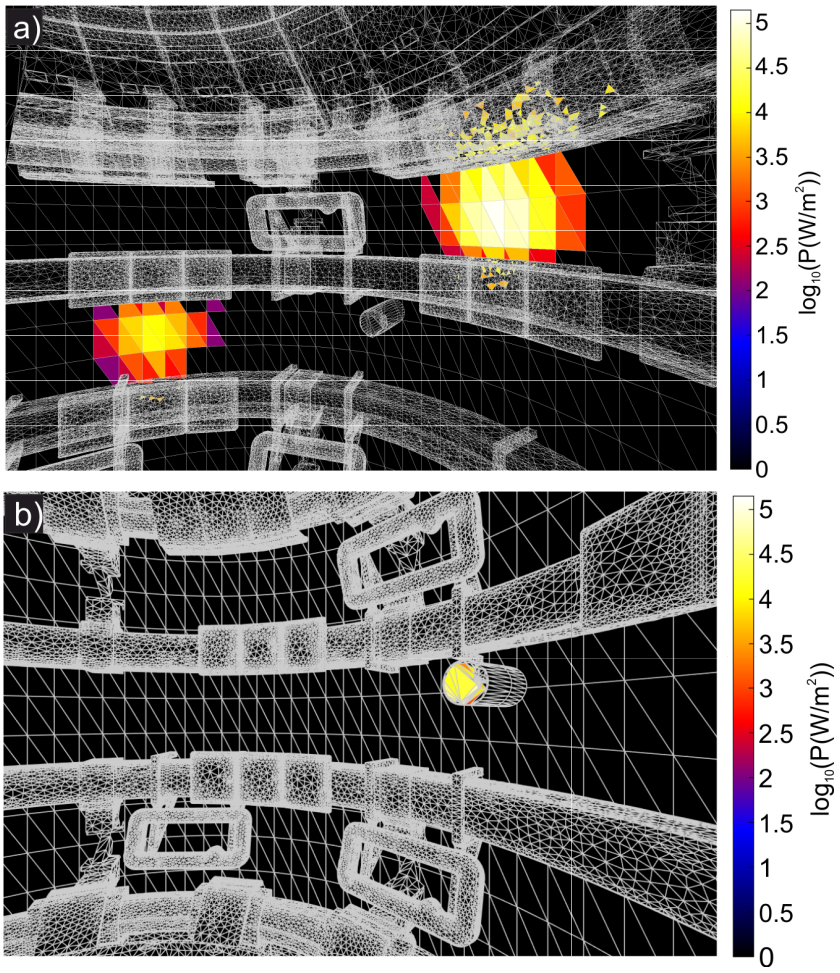

Figure 6.11: (a) Power deposition of the NBI shine-through in MAST-U. (b) Fast-ion power load on the FILD probe (R = 1.4 m).

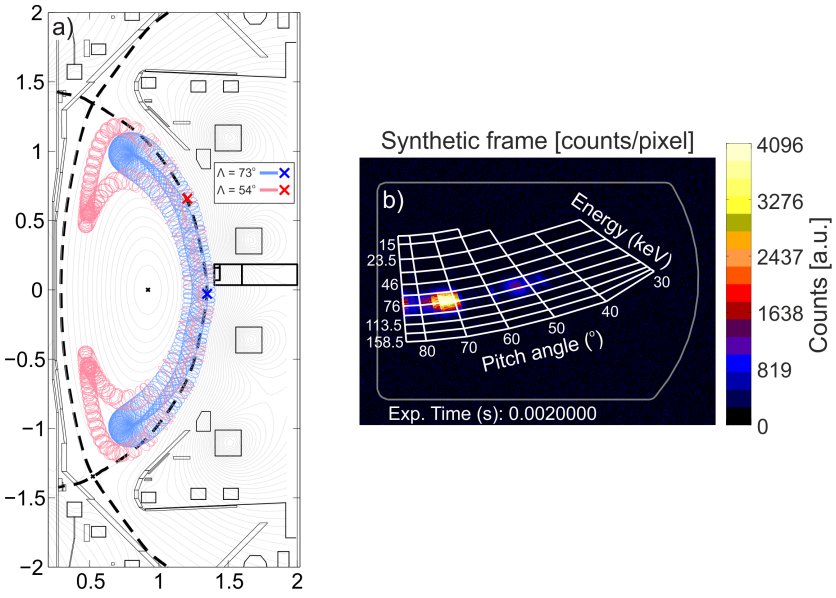

Figure 6.12: (a) Poloidal view of the two orbit topologies reaching the FILD probe. (b) Synthetic FILD frame for the fast ions impinging on the FILD probe.

range while a good shielding in its retracted position. The fast-ion power impinging on the FILD probe is 357 W when it is fully inserted, as it is shown in figure 6.11(b). The fast ions reaching the FILD head can be considered an estimation of the NBI prompt losses. Each NBI produces a different fast-ion distribution that impinges on the FILD probe. The fast ions from the SS injector have a pitch angle of $\Lambda = 73°$ when they collide with the FILD probe, whereas the fast ions from the SW injector are $\Lambda = 54°$. The orbit topologies of the different fast-ion distributions reaching the FILD probe are shown in figure 6.12(a).

The FILDSIM code uses a weighting function that takes into account the finite resolution in velocity space of the FILD detector. It is used to distort the fast-ion distribution on the FILD probe and project it onto a synthetic scintillator plate, where a strike map is also constructed using a field-aligned B = 0.63 T. The synthetic frame, illustrated in Fig. 6.12(b), shows two separate spots on the strike map, each corresponding to a different NBI distribution. This shows that the MAST-U FILD is designed with enough velocity space resolution to distinguish the fast-ion distributions coming from each NBI. This result is aimed to be reproduced during the upcoming diagnostic commissioning.

6.3 ELM-induced Fast-ion Transport and Acceleration in MAST-U

The MAST-U ELM is modelled with the JOREK code under studies of ELM burn-through [214]. The resulting electromagnetic perturbation will be used in ASCOT to study the fast-ion transport and acceleration, similarly to section 6.1. The model is based on the MAST pulse #24763 with an extended outer leg, mimicking a super-X divertor. It consists of a double-null plasma with $I_p = 1\,\mathrm{MA}$, $B_t^{axis} = 0.64\,\mathrm{T}$, $n_e^{axis} = 5.2 \cdot 10^{19}\,\mathrm{m}^{-3}$, $T_e^{axis} = 1.8\,\mathrm{keV}$. The plasma resistivity is a factor 200 above the Spitzer value ($\eta = 5.4 \times 10^{-6}\,\Omega\mathrm{m}$). The diamagnetic terms are not included in the MHD equations. The effect of neutrals are accounted for using a neutral diffusive coefficient ($D_n = 200\,\mathrm{m}^2/\mathrm{s}$). The simulation is run for 8 ms with equilibrium flows only ($n = 0$) to attain divertor detachment. Afterwards, an initial perturbation is introduced in the form of multiple toroidal mode numbers at the noise level, which triggers the ELM. The ELM perturbation is dominantly $n = 10$, which is within the toroidal numbers observed experimentally ($5 \leq n \leq 15$) [215]. Since diamagnetic flows are not accounted, it is believed that higher mode numbers are stabilized by the neutrals effect. The growth rate of the perturbation is $\gamma = 3.45 \times 10^4\,\mathrm{s}^{-1}$ and the development of the dominant mode perturbation lasts around 1.5 ms. The JOREK simulations estimate an energy loss of 10.4% and a particle loss of 12.8%. The electric perturbation is resolved using the Ohm's law accounting for the $\boldsymbol{v} \times \boldsymbol{B}$ and the resistive term only, analogously to equation (6.2). It is observed that both terms are present within similar order of magnitudes ($|\delta \boldsymbol{E}| \sim 8\,\mathrm{kV/m}$).

The ELM perturbation is given as an input to ASCOT, which traces the fast-ion orbits, as it can be observed in figure 6.13(a). Due to the finite Larmor radius effects, the interaction between the fast ions and the ELM perturbation could not be clearly observed in a $R - \Lambda$ grid like in section 6.1. Nonetheless, it could be noted that the transport and acceleration patterns are coupled, – i.e., the transport has a strong effect on the energy variation patterns and viceversa –, thus making it necessary to account for the magnetic and the electric perturbation simultaneously. Both the parallel and the perpendicular component of the electric perturbation have shown to participate in the fast-ion acceleration thus suggesting a sub-gyroradius acceleration similar to the one discussed in section 6.1. The NBI-born fast-ion distribution of the two beams in MAST-U is modelled with BBNBI, as in section 6.2, producing a distribution of 5 million markers for both beams. The fast-ion prompt losses are filtered out and the confined fast-ion orbits are tracked during the MAST-U ELM perturbation. It is estimated that 8.9% of

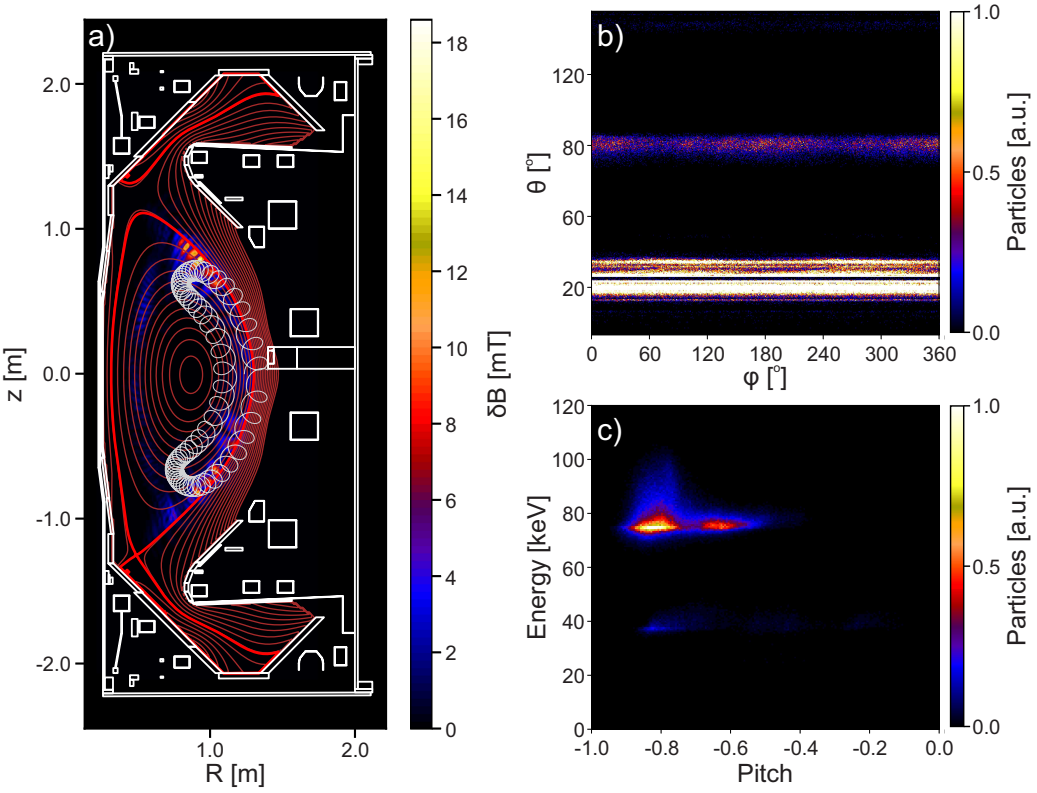

Figure 6.13: (a) Fast-ion orbit and ELM perturbation in MAST-U. (b) ELM-induced fast-ion losses on the MAST-U 2D wall. (c) Velocity space distribution of the ELM-induced fast-ion losses on the MAST-U FILD.

the fast ions are lost during the ELM. This is below the estimated thermal particle and energy losses. The distribution of the fast-ion losses in a 2D wall are illustrated in figure 6.13(b), showing that the ELM-induced fast-ion losses are expelled to the midplane at the LFS and to the lower divertor tiles. This asymmetric distribution of the losses on the upper and lower divertor is caused by the disconnected double-null separatrix, as it can be observed in figure 6.13(a), which effectively behaves like a lower single-null plasma. Figure 6.14 shows the ELM-induced fast-ion loss distribution on the 3D wall. The asymmetric distribution on the upper and lower divertor is clearly seen. Besides, the fast-ion losses collide with the lower poloidal limiters at the LFS and the FILD probe, depicting a coherent result with the 2D distribution of the fast-ion losses. The velocity space of the fast ions colliding with the FILD probe is shown in figure 6.13(c). The distribution shows a broad accelerated population that spreads over the 75 - 100 keV range. This accelerated population is only observed for the SS beam distribution ($\Lambda = -0.81$) while

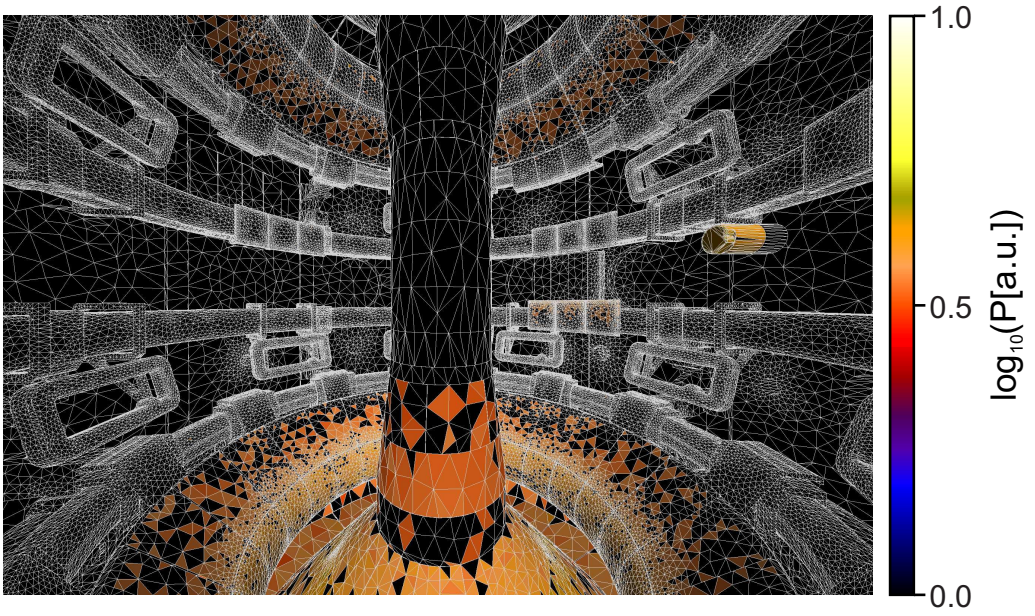

Figure 6.14: ELM-induced fast-ion losses on the MAST-U 3D wall.

it is not observed for the SW beam distribution ($\Lambda = -0.62$). The result reinforces the hypothesis of an ELM-induced acceleration mechanism that is highly sensitive to the fast-ion phase-space, in line with the numerical and experimental observations in AUG.

Chapter 7

Conclusion

7.1 Discussion

The magnetically confined nuclear fusion is the most promising energy source to achieve the goal of zero emissions worldwide. It will be safe, mass-producible and virtually inexhaustible. Tokamaks are only a few decades far from achieving ignited plasmas in ITER. Nowadays, a vivid research in medium size tokamaks like ASDEX Upgrade aims to solve the scientific and technical challenges of ITER and future nuclear plants. In MAST-U, the viability of lower aspect ratio tokamaks, – so called, spherical tokamaks –, and new exhaust physics, like the super-X divertor, are being explored. In tokamaks, ions above the plasma energy, – i.e., fast ions –, are employed to heat up the plasma to fusion relevant temperatures. Therefore, a good fast-ion confinement is essential to achieve fusion power. Besides, fast-ion losses may damage the plasma facing components, posing a risk to the reactor integrity. Thus, the fast-ion losses and their driving mechanisms are an important topic in fusion research. This thesis has been focused on the investigation of the ELM-induced fast-ion losses and acceleration, whose first experimental observations were reported in ASDEX Upgrade [56, 57, 58].

This thesis has encompassed the development of numerical tools that would allow to model the fast-ion orbits and estimate the fast-ion transport and acceleration. A numerical tool called FIOS was built, which solves the Lorentz equation of fast ions in a fully 3D electromagnetic perturbation. This made it possible, for the first time, to estimate the fast-ion acceleration due to the parallel electric field arising during magnetic reconnection events [56, 57, 58], which could be the mechanism that accelerates fast ions during ELMs. FIOS has also made it possible to assess the viability of a new diagnostic in ASDEX Upgrade, the Imaging Heavy-Ion Beam Probe (i-HIBP) [138, 139],

which is now installed in AUG. The 3D electric perturbation module was then merged to the Monte-Carlo full-orbit code, ASCOT5. Besides, in this thesis, a new general-purpose module was introduced in ASCOT5 to account for the time-evolving electromagnetic perturbations in the fast-ion kinetic modelling. The module is based on a multi-dimensional spline interpolation, whose evaluation is optimized to reduce the processing time of the evaluation. The module was employed in the numerical results presented in this thesis.

To investigate the fast-ion losses in MAST-U, the first scintillator-based Fast-Ion Loss Detector (FILD) has been designed and installed in MAST-U during this thesis [158]. The diagnostic is mounted on an axially and angularly actuated telescopic mechanism that makes it possible to independently adapt the orientation [0°, 90°] and radial position [1.40 m, 1.60 m] of the FILD head. The rotary drive adds a unique feature to the diagnostic, allowing it to operate in wider range of plasma q_{95}. The mechanical design required weight optimization and finite-element analysis to guarantee the diagnostic integrity. Besides, the material selection was essential to avoid cold welding of moving components. The probe design and the light acquisition system will provide enough resolution to distinguish fast-ion losses in the energy range of 15 keV to 160 keV. Due to several delays in the MAST-U restart, the MAST-U FILD has not been put in operation yet. Therefore, this thesis has followed different approaches, experimentally and numerically, to solve the lack of experimental data in MAST-U.

Experimentally, the goal was to progress on the experiments in AUG dedicated to the interaction between ELMs and fast ions and find the dominant parameters that affect the interaction. Four dedicated shots have been carried out in the latest experimental campaigns. These shots aimed to populate a wider velocity-space fast-ion distribution, using different NBIs to achieve measurements with the newly installed FILD poloidal array. The resonant interaction between the fast ions and the ELMs was investigated with a q_{95} scan. It was observed that trapped particles do not reveal a pitch-angle splitting, in contrast to passing particles. This observation is in line with the proposed resonant interaction, as the geometrical resonances only depend on the plasma q for passing particles. The correlation between the ELM stability and the fast-ion losses was investigated with a power scan of edge ECRH. A drastic increase of the ELM-induced fast-ion losses was observed during the ECRH power scan. However, this was caused by an increase in the density profiles, which moved the fast-ion content towards the edge, making it more sensitive to interact with the ELMs. Ultimately, an statistical analysis was carried out using a dataset of 14 shots in AUG with similar plasma shape and paramenters. This made it possible to correlate the ELM-syncronized FILD signal and the magnetic perturbation during an ELM, revealing that

the highest fast-ion losses occur during the ELM crash. The correlation of the fast-ion losses with the divertor current and the magnetic perturbation suggests that the fast-ion losses are proportional to the plasma particle losses, governed by the magnetic activity.

Numerically, the aim was to reproduce the main observations of ELM-induced fast-ion losses in AUG and investigate the fast-ion transport and acceleration mechanisms. The fast-ion modelling uses the electromagnetic perturbations simulated with MEGA. The main results of the fast-ion modelling in AUG are the following:

- The ELM-induced transport is dominantly affected by a resonant interaction between the particle orbits and the magnetic perturbation. The chaotic magnetic field lines near the plasma edge also contribute to the fast-ion transport. The results are in line with the experimental correlation between fast-ion losses and magnetic activity.

- The acceleration is caused by a resonant cyclotron acceleration in the particles perpendicular velocity. This is produced by the electric perturbation topology, whose scale is smaller than the fast-ion gyroradii.

- The ELM-induced fast-ion losses are estimated to be 0.37 % of the total fast-ion population, in line with recent estimations using FIDA measurements in AUG [99].

- The simulated ELM-induced losses depict field-aligned patterns near the midplane on the tokamak wall, suggesting a strong effect of the ballooning structure of the perturbation.

- The temporal shifts of toroidally displaced FILD signals during ELMs observed experimentally may be explained by the field-aligned pattern of the losses observed numerically and the toroidal rotation of the perturbation.

- The FILD synthetic signal reveals an accelerated population localized in velocity-space, agreeing with the tomographic inversion of the FILD experimental data.

- The pitch angle of the accelerated population is shifted with respect to the injection geometry due to the dominant acceleration in the perpendicular direction. The opposite effect occurred in the FIOS results, when only a parallel electric field was used.

- The drift in pitch angle is not observed experimentally. This suggests that an electric field with both parallel and perpendicular component should be causing the fast-ion acceleration, as it was proposed by Marchenko et al. [104].

The simulations in AUG have qualitatively reproduced the main experimental observations. However, the important differences between the ELM perturbation simulated with MEGA and the experimental data must be considered, such as the higher dominant toroidal mode numbers and the higher growth rate of the simulated perturbation. Besides, the actual experimental observation of ELM-induced fast-ion acceleration with NBI7 and NBI8 in FILD1 could not be reproduced, probably because of the different topologies of the ELM perturbation. In place, the numerical results are obtained with NBI1 and NBI4, which populates the most resonant regions in the modelled perturbation.

The fast-ion simulations in MAST-U aim to foresee the effect of ELMs on the fast-ion population using an ELM perturbation modelled with JOREK. The MAST-U simulations show ELM-induced losses near the midplane on the low field side of the tokamak wall, depicting the strong effect of the ballooning perturbation. They reveal an acceleration mechanism very sensitive to the fast-ion velocity space, similarly to AUG. Besides, the synthetic FILD signal shows accelerated fast-ion losses spread in energy rather than localized, in contrast to the tomographic inversion of the FILD signal in AUG. This could be caused by the larger rate of fast-ion losses during the ELM in MAST-U, that increases the losses along a larger range of energies. The pitch angle of the accelerated losses is aligned with the NBI pitch angle, in agreement with the AUG experiments. As the electric field parallel and perpendicular components are of the same order of magnitude in the MAST-U model, it corroborates the need to invoke a parallel and a perpendicular electric perturbation to keep the pitch-angle structure.

7.2 Outlook

MAST-U achieved its first plasma in October 2020. After the commission of the main systems, the first experimental campaign is starting in 2021. During the experimental campaign, FILD will be commissioned, providing measurements of the fast-ion losses for many experiments in MAST-U and testing the design presented in this thesis. Dedicated experiments on the interaction between ELMs and fast ions are being organized in MAST-U. With regards to AUG, further experiments are being planned to compare the fast-ion losses during ELM-mitigated regimes and to investigate the effect on

the fast-ion losses of ELM-pacing techniques that enhance the plasma density, such as gas puffing [200] or pellet injection [203]. The dataset presented in this thesis will allow for more statistical analyses, such as the comparison of ELM-synchronized FILD data from different poloidal and toroidal positions. MAST-U, TCV and JET data of ELM-induced fast-ion losses is expected to be added to the dataset, enabling multi-machine studies that will make it possible to construct a scalability diagram of the ELM-induced fast-ion losses. This will help to estimate the fast-ion losses in future devices. Alternative acceleration mechanisms will be investigated, such as wave-particle energy transfer between the fast ions and high-frequency magnetic perturbations ($\sim$ MHz). In this hypothesis, the accelerated fast ions would be merely expelled by the ELMs. High-frequency Alfvén eigenmodes have already been observed in ASDEX Upgrade with the Ion-Cyclotron Emission (ICE) diagnostic in the presence of beam-injected ions RF-accelerated at the third cyclotron harmonic [216]. Nonetheless, these high frequency modes are suspected to be shear waves, localized in the plasma core near the magnetic axis, thus being very unlikely correlated with the accelerated fast-ion losses during ELMs.

The great differences between the ELMs observed experimentally and the ELM perturbation simulated in MEGA motivate the modelling of the fast-ion transport and acceleration with an ELM perturbation closer to the experiments. It is believed that the main differences would be overcome adding diamagnetic effects to the MHD simulations, as it has proven to lower the dominant mode number and growth rate in the ELM simulations [208]. Besides, the effect of fast ions on the ELM stability is currently being adressed with MEGA hybrid kinetic-MHD simulations [206, 207] and will be experimentally investigated in AUG.

List of Publications

List of publications as main author

- J.F. Rivero-Rodriguez et al. Investigation of beam-ion transport and acceleration during edge localized modes in ASDEX Upgrade. *in preparation.*
- J.F. Rivero-Rodriguez et al. Upgrade and absolute calibration of the JET scintillator-based Fast-Ion Loss Detector. *Rev. Sci. Instrum.*, 92:043553, 2021.
- J.F. Rivero-Rodriguez et al. A fast model to resolve the velocity-space of fast-ion losses detected in ASDEX Upgrade and MAST Upgrade. *J. Instrum.*, 14:C09015, 2019.
- J.F. Rivero-Rodriguez et al. A rotary and reciprocating scintillator based fast-ion loss detector for the MAST-U tokamak. *Rev. Sci. Instrum.*, 89:10I112, 2018.

List of additional publications

- J. Gonzalez-Martin et al. Self-Adaptive Diagnostic of Radial Fast-Ion Loss Measurements on the ASDEX Upgrade Tokamak. *Rev. Sci. Instrum.*, 92:053538, 2021.
- P. Oyola et al. Implementation of synthetic fast-ion loss detector and imaging heavy ion beam probe diagnostics in the 3D hybrid kinetic-MHD code MEGA. *Rev. Sci. Instrum.*, 92:043558, 2021.
- J. Galdon-Quiroga et al. Observation of accelerated beam ion population during edge localized modes in the ASDEX Upgrade tokamak. *Nucl. Fusion*, 59:066016, 2019.
- J. Gonzalez-Martin et al. First measurements of a magnetically driven fast-ion loss detector on ASDEX Upgrade. *J. Instrum.*, 14:C11005, 2019.

- G. Birkenmeier et al. Beam modelling and hardware design of an imaging heavy ion beam probe for ASDEX Upgrade. *J. Instrum.*, 14:C10030, 2019.
- J. Ayllon-Guerola et al. Determination of the Fast-Ion Phase-Space Coverage for the FILD Spatial Array of the ASDEX Upgrade Tokamak. *J. Instrum.*, 14:C10032, 2019.
- H. Meyer et al. Overview of physics studies on ASDEX Upgrade. *Nucl. Fusion*, 59:112014, 2019.
- E. Joffrin et al. Overview of the JET preparation for deuterium-tritium operation with the ITER like-wall. *Nucl. Fusion*, 59:112021, 2019.
- B. Labit et al. Dependence on plasma shape and plasma fueling for small edge-localized mode regimes in TCV and ASDEX Upgrade. *Nucl. Fusion*, 59:086020, 2019.
- M. Garcia-Munoz et al. Active control of Alfvén eigenmodes in magnetically confined toroidal plasmas. *Plasma Phys. Control. Fusion*, 61:054007, 2019.
- L. Sanchis et al. Characterisation of the fast-ion edge resonant transport layer induced by 3D perturbative fields in the ASDEX Upgrade tokamak through full orbit simulations. *Plasma Phys. Control. Fusion*, 61:014038, 2019.
- J. Galdon-Quiroga et al. Beam-Ion Acceleration during Edge Localized Modes in the ASDEX Upgrade Tokamak. *Phys. Rev. Lett.*, 121:025002, 2018.
- J. Gonzalez-Martin et al. First measurements of a scintillator based fast-ion loss detector near the ASDEX Upgrade divertor. *Rev. Sci. Instrum.*, 89:10I106, 2018.
- J. Galdon-Quiroga et al. Velocity-space sensitivity and tomography of scintillator-based fast-ion loss detectors. *Plasma Phys. Control. Fusion*, 60:105005, 2018.
- V. Kiptily et al. Fusion product losses due to fishbone instabilities in deuterium JET plasmas. *Nucl. Fusion*, 58:014003, 2018.
- J. Galdon-Quiroga et al. Conceptual design of a scintillator based Imaging Heavy Ion Beam Probe for the ASDEX Upgrade tokamak. *J. Instrum.*, 12:C08023, 2017.

- M. Rodriguez-Ramos et al. First absolute measurements of fast-ion losses in the ASDEX Upgrade tokamak. *Plasma Phys. Control. Fusion*, 59:105009, 2017.

- J. Ayllon-Guerola et al. Dynamic and thermal simulations of a fast-ion loss detector for ITER. *Fusion Eng. Des.*, 123:807-810, 2017.

- M. Kocan et al. The impact of the fast ion fluxes and thermal plasma loads on the design of the ITER fast ion loss detector. *J. Instrum.*, 12:C12027, 2017.

- J. Ayllon-Guerola et al. A fast feedback controlled magnetic drive for the ASDEX Upgrade fast-ion loss detectors. *Rev. Sci. Instrum*, 87:11E705, 2016.

- M. Garcia-Munoz et al. Conceptual design of the ITER fast-ion loss detector. *Rev. Sci. Instrum*, 87:11D829, 2016.

Bibliography

[1] Intergovernmental Panel on Climate Change. Global warming of 1.5° C. Technical report, Intergovernmental Panel on Climate Change, 2018.

[2] World Health Organization. *Air Quality Guidelines Global Update*, 2005.

[3] Maddison Project Database. *Rebasing 'Maddison': new income comparisons and the shape of long-run economic development*, 2018.

[4] BP. BP statistical review of world energy. Technical report, BP, 2019.

[5] International Nuclear Safety Advisory Group. The Chernobyl accident: Updating of INSAG-1. Technical report, International Atomic Energy Agency, 1992.

[6] International Atomic Energy Agency. The Fukushima Daiichi accident. Technical report, International Atomic Energy Agency, 2015.

[7] J. A. Wesson. *Tokamaks*. Clarendon Press, 1997.

[8] J. D. Lawson. Some criteria for a useful thermonuclear reactor. Technical report, Atomic Energy Research Establishment, 1955.

[9] F. G. Rimini et al. High fusion performance from deuterium-tritium plasmas in JET. *Nucl. Fusion*, 39:209, 1999.

[10] J. L. Johnson. Stellarator and heliotron devices. *Nucl. Fusion*, 39(2):293, 1999.

[11] S. Li et al. Optimal Tracking for a Divergent-Type Parabolic PDE System in Current Profile Control. *Abstract and Applied Analysis*, 2014:940965, 2014.

[12] J. M. Moret et al. Influence of plasma shape on transport in the TCV tokamak. *Phys. Rev. Lett.*, 79:2057–2060, 1997.

[13] R. Kleiber, R. Bilato, et al. IPP summer university for plasma physics 2011. Course book.

[14] Y-K. M. Peng. Spherical torus, compact fusion at low field. Technical report, Oak Ridge National Laboratory, 1985.

[15] Y-K. M. Peng and D.J. Strickler. Features of spherical torus plasmas. *Nucl. Fusion*, 26:769, 1986.

[16] J. P. Freidberg. *Plasma Physics and Fusion Energy.* Cambridge University Press, 2007.

[17] J. D. Strachan et al. TFTR DT experiments. *Plasma Phys. Controlled Fusion*, 39:103–114, 1997.

[18] J. Jacquinot et al. Overview of ITER physics deuterium-tritium experiments in JET. *Nucl. Fusion*, 39:235, 1999.

[19] W. Yuanxi et al. First engineering commissioning of EAST tokamak. *Plasma Sci. Technol.*, 8:253, 2006.

[20] H. Vernickel et al. ASDEX upgrade: A poloidal divertor tokamak adapted to reactor requirements. *J. Nucl. Mater.*, 128-129:71–77, 1984.

[21] K. H. Burrell et al. Overview of recent experimental results from the DIII-D advanced tokamak program. *Nucl. Fusion*, 43:1555, 2003.

[22] K. Ikeda. Progress in the ITER physics basis. *Nucl. Fusion*, 47(6), 2007.

[23] H. Zohm. On the physics guidelines for a tokamak DEMO. *Nucl. Fusion*, 53:073019, 2013.

[24] M. Ono et al. Progress toward commissioning and plasma operation in NSTX-U. *Nucl. Fusion*, 55:073007, 2015.

[25] J. R. Harrison et al. Overview of new MAST physics in anticipation of first results from MAST Upgrade. *Nucl. Fusion*, 59:112011, 2019.

[26] E. Gibney. UK hatches plan to build world's first fusion power plant. *Nature*, 2019.

[27] B. V. Sumov. *Plasma Astrophysics*, chapter The Generalized Ohm's Law in Plasma, pages 193–204. Springer New York, 2007.

[28] E. Speth. Neutral beam heating of fusion plasmas. *Rep. Prog. Phys.*, 52(1):57–121, 1989.

[29] R. A. Cairns. *Radiofrequency heating in plasmas.* CRC Press, 1991.

[30] A. Fasoli et al. Chapter 5: Physics of energetic ions. *Nucl. Fusion*, 47(6):S264, 2007.

[31] W. W. Heidbrink and G.J. Sadler. The behaviour of fast ions in tokamak experiments. *Nucl. Fusion*, 34(4):535–615, 1994.

[32] J. Sheffield. Options for an ignited tokamak. Technical report, ORNL, 1984.

[33] J. Galdon-Quiroga et al. Velocity space resolved absolute measurement of fast ion losses induced by a tearing mode in the ASDEX Upgrade tokamak. *Nucl. Fusion*, 58(3):036005, 2018.

[34] V. G. Kiptily et al. Recent progress in fast ion studies on JET. *Nucl. Fusion*, 49:065030, 2009.

[35] W. W. Heidbrink and R. B. White. Mechanisms of energetic-particle transport in magnetically confined plasmas. *Phys. Plasmas*, 27:030901, 2020.

[36] K. G. McClements and E. D. Fredrickson. Energetic particles in spherical tokamak plasmas. *Plasma Phys. Controlled Fusion*, 59(5):053001, 2017.

[37] F. Wagner et al. Regime of improved confinement and high beta in neutral-beam-heated divertor discharges of the ASDEX tokamak. *Phys. Rev. Lett.*, 49:1408–1412, 1982.

[38] H. Meyer et al. Overview of physics studies on ASDEX Upgrade. *Nucl. Fusion*, 59:112014, 2019.

[39] H. Risken and T. Frank. *The Fokker-Planck Equation.* Springer-Verlag Berlin Heidelberg, 1996.

[40] A. Snicker. *Towards realistic orbit following simulations of fast ions in ITER.* PhD thesis, Aalto University, 2014.

[41] J. Varje, K. Sarkimaki, et al. High-performance orbit-following code ASCOT5 for Monte Carlo simulations in fusion plasmas, 2019.

[42] S. H. Ward et al. Verification and validation of the high-performance lorentz-orbit code for use in stellarators and tokamaks (LOCUST).

[43] R.V. Budny et al. Simulations of deuterium-tritium experiments in TFTR. *Nucl. Fusion*, 32(3):429–447, 1992.

[44] H. Zohm. *Magnetohydrodynamic Stability of Tokamaks*. Wiley-VCH, 2014.

[45] S. P. Hirshman and J. C. Whitson. Steepest-descent moment method for three-dimensional magnetohydrodynamic equilibria. *The Physics of Fluids*, 26(12):3553–3568, 1983.

[46] G. T. A. Huysmans and O. Czarny. MHD stability in X-point geometry: simulation of ELMs. *Nucl. Fusion*, 47(7):659, 2007.

[47] Y. Q. Liu et al. Feedback stabilization of nonaxisymmetric resistive wall modes in tokamaks. I. electromagnetic model. *Phys. Plasmas*, 7(9):3681–3690, 2000.

[48] Y. Todo and T. Sato. Linear and nonlinear particle-magnetohydrodynamic simulations of the toroidal alfvén eigenmode. *Phys. Plasmas*, 5(5):1321–1327, 1998.

[49] C. Sommariva et al. Test particles dynamics in the JOREK 3d non-linear MHD code and application to electron transport in a disruption simulation. *Nucl. Fusion*, 58(1):016043, 2017.

[50] D. C. van Vugt et al. Kinetic modeling of ELM-induced tungsten transport in a tokamak plasma. *Phys. Plasmas*, 26(4):042508, 2019.

[51] B. Geiger. *Fast-ion transport studies using FIDA spectroscopy at the ASDEX Upgrade tokamak*. PhD thesis, Max-Planck-Institut für Plasmaphysik, 2013.

[52] A. R. Field et al. Beam emission spectroscopy for density turbulence measurements on the MAST spherical tokamak. *Rev. Sci. Instrum.*, 80(7):073503, 2009.

[53] P. A. Schneider et al. A new compact solid-state neutral particle analyser at ASDEX upgrade: Setup and physics modeling. *Rev. Sci. Instrum.*, 86(7):073508, 2015.

[54] P. J. Bonofiglo et al. Improvements to the faraday cup fast ion loss detector and magnetohydrodynamic induced fast ion loss measurements in joint european torus plasmas. *Rev. Sci. Instrum.*, 91(9):093502, 2020.

[55] S. J. Zweben. Pitch angle resolved measurements of escaping charged fusion products in TFTR. *Nucl. Fusion*, 29(5):825–833, 1989.

[56] J. Galdon-Quiroga et al. Beam-ion acceleration during edge localized modes in the ASDEX upgrade tokamak. *Phys. Rev. Lett.*, 121:025002, 2018.

[57] J. Galdon-Quiroga et al. Observation of accelerated beam ion population during edge localized modes in the ASDEX upgrade tokamak. *Nucl. Fusion*, 59(6):066016, 2019.

[58] J. Galdon-Quiroga. *Velocity-space resolved measurements of fast-ion losses due to magnetohydrodynamic instabilities in the ASDEX Upgrade tokamak*. PhD thesis, Universidad de Sevilla, 2019.

[59] J. A. Bittencourt. *Fundamentals of Plasma Physics*. Springer, 2004.

[60] R. G. Littlejohn. Variational principles of guiding centre motion. *J. Plasma Phys.*, 29(1):111125, 1983.

[61] R. B. White. *The Theory of Toroidally Confined Plasmas*. Imperial College Press, 2001.

[62] T. G. Northrop. The guiding center approximation to charged particle motion. *Ann. Phys.*, 15(1):79–101, 1961.

[63] E. Viezzer. *Radial electric field studies in the plasma edge of ASDEX Upgrade*. PhD thesis, Max-Planck-Institut für Plasmaphysik, 2012.

[64] H. Goldstein. *Classical Mechanics*. Addison-Wesley, 1980.

[65] L. Sanchis. *Fast-ion transport induced by externally applied Resonant Magnetic Perturbations in the ASDEX Upgrade tokamak*. PhD thesis, Universidad de Sevilla, 2019.

[66] W. W. Heidbrink. Basic physics of Alfvén instabilities driven by energetic particles in toroidally confined plasmas. *Phys. Plasmas*, 15(5):055501, 2008.

[67] M. Rodriguez-Ramos. *Calibración absoluta y aplicación de los detectores de pérdidas de iones rápidos basados en materiales centelleadores para dispositivos de fusión nuclear*. PhD thesis, Universidad de Sevilla, 2017.

[68] F. Ryter et al. Experimental studies of electron transport. *Plasma Phys. Controlled Fusion*, 43(12A):A323–A338, 2001.

[69] E. J. Doyle et al. Chapter 2: Plasma confinement and transport. *Nucl. Fusion*, 47(6):S18–S127, 2007.

[70] H. Zohm. Edge localized modes (ELMs). *Plasma Phys. Controlled Fusion*, 38(2):105, 1996.

[71] J. W. Connor. Edge-localized modes - physics and theory. *Plasma Phys. Controlled Fusion*, 40(5):531–542, 1998.

[72] W. Suttrop. The physics of large and small edge localized modes. *Plasma Phys. Controlled Fusion*, 42(5A):A1–A14, 2000.

[73] H. Wilson. Edge localized modes in tokamaks. *Fusion Sci. Technol.*, 53(2T):161–169, 2008.

[74] A. Kirk et al. Comparison of the spatial and temporal structure of type-I ELMs. *J. Phys. Conf. Ser.*, 123:012011, 2008.

[75] C. Ham et al. Filamentary plasma eruptions and their control on the route to fusion energy. *Nat. Rev. Phys.*, 2:150–167, 2020.

[76] T. Eich et al. Type-I ELM substructure on the divertor target plates in ASDEX upgrade. *Plasma Phys. Controlled Fusion*, 47(6):815–842, 2005.

[77] A. Loarte et al. Characteristics of type I ELM energy and particle losses in existing devices and their extrapolation to ITER. *Plasma Phys. Controlled Fusion*, 45(9):1549–1569, 2003.

[78] E. Viezzer et al. Dynamics of the pedestal transport during edge localized mode cycles at ASDEX upgrade. *Plasma Phys. Controlled Fusion*, 62(2):024009, 2020.

[79] F. Mink et al. Toroidal mode number determination of ELM associated phenomena on ASDEX upgrade. *Plasma Phys. Control. Fusion*, 58(12):125013, 2016.

[80] F. Mink et al. Nonlinear coupling induced toroidal structure of edge localized modes. *Nucl. Fusion*, 58(2):026011, 2018.

[81] J. Stober et al. Type II ELMy H modes on ASDEX upgrade with good confinement at high density. *Nucl. Fusion*, 41(9):1123–1134, 2001.

[82] Y. Kamada et al. Disappearance of giant ELMs and appearance of minute grassy ELMs in JT-60U high-triangularity discharges. *Plasma Phys. Controlled Fusion*, 42(5A):A247–A253, 2000.

[83] R. Maingi et al. Characterization of small, type V edge-localized modes in the national spherical torus experiment. *Phys. Plasmas*, 13(9):092510, 2006.

[84] H. R. Wilson et al. Ideal magnetohydrodynamic stability of the tokamak high-confinement-mode edge region. *Phys. Plasmas*, 6(5):1925–1934, 1999.

[85] P. B. Snyder et al. Edge localized modes and the pedestal: A model based on coupled peeling-ballooning modes. *Phys. Plasmas*, 9(5):2037–2043, 2002.

[86] P. B. Snyder et al. Progress in the peeling-ballooning model of edge localized modes: Numerical studies of nonlinear dynamics. *Phys. Plasmas*, 12(5):056115, 2005.

[87] M. R. Wade et al. Edge-localized-mode–induced transport of impurity density, energy, and momentum. *Phys. Rev. Lett.*, 94:225001, 2005.

[88] G. Federici et al. Plasma-material interactions in current tokamaks and their implications for next step fusion reactors. *Nucl. Fusion*, 41(12):1967–2137, 2001.

[89] A. Loarte et al. Characterization of pedestal parameters and edge localized mode energy losses in the joint european torus and predictions for the international thermonuclear experimental reactor. *Phys. Plasmas*, 11(5):2668–2678, 2004.

[90] T. Eich et al. ELM divertor peak energy fluence scaling to ITER with data from JET, MAST and ASDEX upgrade. *Nuclear Materials and Energy*, 12:84–90, 2017. Proceedings of the 22nd International Conference on Plasma Surface Interactions.

[91] W. Suttrop et al. Experimental conditions to suppress edge localised modes by magnetic perturbations in the ASDEX upgrade tokamak. *Nucl. Fusion*, 58(9):096031, 2018.

[92] P. T. Lang et al. ELM pace making and mitigation by pellet injection in ASDEX upgrade. *Nucl. Fusion*, 44(5):665–677, 2004.

[93] E. de la Luna et al. Understanding the physics of ELM pacing via vertical kicks in JET in view of ITER. *Nucl. Fusion*, 56(2):026001, 2015.

[94] E. Viezzer. Access and sustainment of naturally ELM-free and small-ELM regimes. *Nucl. Fusion*, 58(11):115002, 2018.

[95] K. H. Burrell et al. Quiescent double barrier high-confinement mode plasmas in the DIII-D tokamak. *Phys. Plasmas*, 8(5):2153–2162, 2001.

[96] D. G. Whyte et al. I-mode: an H-mode energy confinement regime with L-mode particle transport in Alcator C-Mod. *Nucl. Fusion*, 50(10):105005, 2010.

[97] N. Oyama et al. Pedestal conditions for small ELM regimes in tokamaks. *Plasma Phys. Controlled Fusion*, 48(5A):A171–A181, 2006.

[98] M. García-Muñoz et al. Fast-ion losses induced by ELMs and externally applied magnetic perturbations in the ASDEX upgrade tokamak. *Plasma Phys. Controlled Fusion*, 55(12):124014, 2013.

[99] A. Jansen van Vuuren et al. Experimental study of ELM induced fast-ion transport using passive FIDA spectroscopy at the ASDEX upgrade tokamak. *Nucl. Fusion*, 61(4):046001, 2021.

[100] S. J. Freethy et al. Electron kinetics inferred from observations of microwave bursts during edge localized modes in the mega-amp spherical tokamak. *Phys. Rev. Lett.*, 114:125004, 2015.

[101] A. W. Leonard. Edge-localized-modes in tokamaks. *Phys. Plasmas*, 21(9):090501, 2014.

[102] P. Helander et al. Ion acceleration during reconnection in MAST. *Phys. Rev. Lett.*, 89:235002, 2002.

[103] K. G. McClements et al. Particle acceleration during merging-compression plasma start-up in the mega amp spherical tokamak. *Plasma Phys. Controlled Fusion*, 60(2):025013, 2017.

[104] V. S. Marchenko and S. N. Reznik. Cyclotron acceleration of energetic ions by plasma blobs. *Phys. Plasmas*, 25(8):084502, 2018.

[105] J. A. Heikkinen and S. K. Sipila. Power transfer and current generation of fast ions with large-$k\theta$ waves in tokamak plasmas. *Phys. Plasmas*, 2(10):3724–3733, 1995.

[106] E. Hirvijoki et al. Monte carlo implementation of a guiding-center Fokker-Planck kinetic equation. *Phys. Plasmas*, 20(9):092505, 2013.

[107] E. Hirvijoki et al. ASCOT: Solving the kinetic equation of minority particle species in tokamak plasmas. *Comput. Phys. Commun.*, 185(4):1310–1321, 2014.

[108] J. P. Boris. Relativistic plasma simulation - optimization of a hybrid code. In *Conference of the Numerical Simulation of Plasmas*, 1971.

[109] D. Badouel. *Graphic Gems*, chapter An Efficient Ray-Polygon Intersection, pages 390–393. Academic Press Professional, Inc., USA, 1990.

[110] O. Asunta et al. Modelling neutral beams in fusion devices: Beamlet-based model for fast particle simulations. *Comput. Phys. Commun.*, 188:33–46, 2015.

[111] O. Sauter and S.Yu. Medvedev. Tokamak coordinate conventions: COCOS. *Comput. Phys. Commun.*, 184(2):293 – 302, 2013.

[112] *NTCC PSPLINE Module.*

[113] T. Kurki-Suonio et al. ASCOT simulations of fast ion power loads to the plasma-facing components in ITER. *Nucl. Fusion*, 49(9):095001, 2009.

[114] S. Akaslompolo et al. Armoring of the Wendelstein 7-X divertor-observation immersion-tubes based on nbi fast-ion simulations. *Fusion Eng. Des.*, 146:862–865, 2019.

[115] L. Sanchis et al. Characterisation of the fast-ion edge resonant transport layer induced by 3D perturbative fields in the ASDEX upgrade tokamak through full orbit simulations. *Plasma Phys. Controlled Fusion*, 61(1):014038, 2018.

[116] T. Kurki-Suonio et al. Fast ion power loads on ITER first wall structures in the presence of NTMs and microturbulence. *Nucl. Fusion*, 51(8):083041, 2011.

[117] E. Hirvijoki et al. Alfvén Eigenmodes and Neoclassical tearing modes for orbit-following implementations. *Comput. Phys. Commun.*, 183(12):2589–2593, 2012.

[118] A. Snicker et al. Power loads to ITER first wall structures due to fusion alphas in a non-axisymmetric magnetic field including the presence of MHD modes. *Nucl. Fusion*, 53(9):093028, 2013.

[119] O. Asunta et al. Simulations of fast ion wall loads in ASDEX upgrade in the presence of magnetic perturbations due to ELM-mitigation coils. *Nucl. Fusion*, 52(9):094014, 2012.

[120] J. Varje et al. ASCOT-AFSI simulations of fusion products for the main operating scenarios in JT-60SA. In *46th EPS Conference on Plasma Physics*, 2019.

[121] S. Sipila et al. ASCOT orbit-following simulations of ion cyclotron heating with synthetic fast ion loss diagnostic: a first application to ASDEX upgrade. 2021.

[122] J. A. Heikkinen et al. Monte carlo simulation of runaway electrons in a toroidal geometry. *Comput. Phys. Commun.*, 76(2):215–230, 1993.

[123] J. Miettunen et al. The effect of non-axisymmetric wall geometry on ^{13}C transport in ASDEX upgrade. *Nucl. Fusion*, 52(3):032001, 2012.

[124] J. Galdon-Quiroga et al. Velocity-space sensitivity and tomography of scintillator-based fast-ion loss detectors. *Plasma Phys. Controlled Fusion*, 60(10):105005, 2018.

[125] A. Werner et al. Fast ion losses in the W7-AS stellarator. *Rev. Sci. Instrum.*, 72(1):780–783, 2001.

[126] S. Baeumel et al. Scintillator probe for lost alpha measurements in JET. *Rev. Sci. Instrum.*, 75(10):3563–3565, 2004.

[127] A. S. Jacobsen et al. Inversion methods for fast-ion velocity-space tomography in fusion plasmas. *Plasma Physics and Controlled Fusion*, 58(4):045016, 2016.

[128] M. Salewski et al. Tomography of fast-ion velocity-space distributions from synthetic CTS and FIDA measurements. *Nucl. Fusion*, 52(10):103008, 2012.

[129] M. Salewski et al. Combination of fast-ion diagnostics in velocity-space tomographies. *Nucl. Fusion*, 53(6):063019, 2013.

[130] M. Salewski et al. Measurement of a 2D fast-ion velocity distribution function by tomographic inversion of fast-ion D-alpha spectra. *Nucl. Fusion*, 54(2):023005, 2014.

[131] M. Salewski et al. Fast-ion energy resolution by one-step reaction gamma-ray spectrometry. *Nucl. Fusion*, 56(4):046009, 2016.

[132] M. Salewski et al. MeV-range velocity-space tomography from gamma-ray and neutron emission spectrometry measurements at JET. *Nucl. Fusion*, 57(5):056001, 2017.

[133] M. Garcia-Munoz et al. Conceptual design of the ITER fast-ion loss detector. *Rev. Sci. Instrum.*, 87(11):1–5, 2016.

[134] J. F. Rivero-Rodriguez et al. A fast model to resolve the velocity-space of fast-ion losses detected in ASDEX Upgrade and MAST Upgrade. *J. Instrum.*, 14(09):C09015–C09015, 2019.

[135] R. B. White et al. Ripple-induced energetic particle loss in tokamaks. *Phys. Plasmas*, 3(8):3043–3054, 1996.

[136] Y. Todo et al. Comprehensive magnetohydrodynamic hybrid simulations of fast ion driven instabilities in a large helical device experiment. *Phys. Plasmas*, 24(8):081203, 2017.

[137] O. Czarny and G. Huysmans. Bézier surfaces and finite elements for MHD simulations. *J. Comput. Phys.*, 227(16):7423–7445, 2008.

[138] J. Galdon-Quiroga et al. Conceptual design of a scintillator based imaging heavy ion beam probe for the ASDEX upgrade tokamak. *J. Instrum.*, 12(08):C08023–C08023, 2017.

[139] G. Birkenmeier et al. Beam modelling and hardware design of an imaging heavy ion beam probe for ASDEX upgrade. *J. Instrum.*, 14(10):C10030–C10030, 2019.

[140] J. C. Maxwell. *A treatise on electricity and magnetism.* Clarendon Press, 1873.

[141] F. Zonca, L. Chen, et al. Nonlinear dynamics of phase space zonal structures and energetic particle physics in fusion plasmas. *New J. Phys.*, 17(1):013052, 2015.

[142] L. Chen and F. Zonca. Physics of Alfvén waves and energetic particles in burning plasmas. *Rev. Mod. Phys.*, 88:015008, 2016.

[143] J. Stoer and R. Bulirsch. *Introduction to Numerical Analysis*. Springer, 2002.

[144] D. García-Vallejo and W. Schiehlen. Three-dimensional simulation of human walking optimizing aesthetics and energy. Technical Report Institutsbericht IB-45, Institute of Engineering and Computational Mechanics, University of Stuttgart, 70569 Stuttgart, 2009.

[145] C. de Boor. *A Practical Guide to Splines*. Springer, 1978.

[146] M. García-Muñoz. *Fast Response Scintillator Based Detector for MHD Induced Energetic Ion Losses in ASDEX Upgrade*. PhD thesis, Max-Planck-Institut für Plasmaphysik, 2006.

[147] M. García-Muñoz et al. Fast-ion losses due to high-frequency MHD perturbations in the ASDEX upgrade Tokamak. *Phys. Rev. Lett.*, 100(5):1–4, 2008.

[148] M. Garcia-Munoz et al. MHD induced fast-ion losses on ASDEX Upgrade. *Nucl. Fusion*, 49:085014, 2009.

[149] M. García-Muñoz et al. Convective and diffusive energetic particle losses induced by shear Alfvén waves in the ASDEX upgrade tokamak. *Phys. Rev. Lett.*, 104:185002, 2010.

[150] D. S. Darrow et al. Measurement of loss of DT fusion products using scintillator detectors in TFTR (invited). *Rev. Sci. Instrum.*, 66:476, 1995.

[151] M. García-Muñoz et al. Scintillator based detector for fast-ion losses induced by magnetohydrodynamic instabilities in the ASDEX upgrade tokamak. *Rev. Sci. Instrum.*, 80(5):053503, 2009.

[152] J. Ayllon-Guerola et al. A fast feedback controlled magnetic drive for the ASDEX upgrade fast-ion loss detectors. *Rev. Sci. Instrum.*, 87(11):11E705, 2016.

[153] J. Gonzalez-Martin et al. First measurements of a scintillator based fast-ion loss detector near the ASDEX Upgrade divertor. *Rev. Sci. Instrum.*, 89(10):10I106, 2018.

[154] J. Gonzalez-Martin et al. First measurements of a magnetically driven fast-ion loss detector on ASDEX upgrade. *J. Instrum.*, 14(11):C11005–C11005, 2019.

[155] R. K. Fisher et al. Scintillator-based diagnostic for fast ion loss measurements on DIII-D. *Rev. Sci. Instrum.*, 81(10):10D307, 2010.

[156] X. Chen et al. Near midplane scintillator-based fast ion loss detector on DIII-D. *Rev. Sci. Instrum.*, 83(10):10D707, 2012.

[157] D. S. Darrow. Scintillator based energetic ion loss diagnostic for the national spherical torus experiment. *Rev. Sci. Instrum.*, 79(2):023502, 2008.

[158] J. F. Rivero-Rodriguez et al. A rotary and reciprocating scintillator based fast-ion loss detector for the MAST-U tokamak. *Rev. Sci. Instrum.*, 89(10):10I112, 2018.

[159] H. Zohm et al. Recent ASDEX Upgrade research in support of ITER and DEMO. *Nucl. Fusion*, 55:104010, 2015.

[160] A. Kallenbach et al. Overview of ASDEX upgrade results. *Nucl. Fusion*, 57(10):102015, 2017.

[161] A. Herrmann et al. A new upper divertor with internal coils for ASDEX upgrade status of the project. *Fusion Eng. Des.*, 146:920–923, 2019.

[162] O. Vollmer et al. Commissioning and first operation of the ASDEX upgrade neutral beam system. In *15th IEEE/NPSS Symposium. Fusion Engineering*, volume 1, pages 451–454 vol.1, 1993.

[163] V. Bobkov et al. First results with 3-strap ICRF antennas in ASDEX upgrade. *Nucl. Fusion*, 56(8):084001, 2016.

[164] D. Wagner et al. Extension of the multi-frequency ECRH system at ASDEX upgrade. *EPJ Web Conf.*, 149:03004, 2017.

[165] U. Schneider et al. Boronization of ASDEX. *J. Nucl. Mater.*, 176-177(C):350–356, 1990.

[166] M. Cavedon et al. A fast edge charge exchange recombination spectroscopy system at the ASDEX upgrade tokamak. *Rev. Sci. Instrum.*, 88(4):043103, 2017.

[167] B. Kurzan and H. D. Murmann. Edge and core thomson scattering systems and their calibration on the ASDEX upgrade tokamak. *Rev. Sci. Instrum.*, 82(10):103501, 2011.

[168] M. Willensdorfer et al. Characterization of the Li-BES at ASDEX upgrade. *Plasma Phys. Controlled Fusion*, 56(2):025008, 2014.

[169] A. Mlynek et al. Design of a digital multiradian phase detector and its application in fusion plasma interferometry. *Rev. Sci. Instrum.*, 81(3):033507, 2010.

[170] M. Willensdorfer et al. Plasma response measurements of external magnetic perturbations using electron cyclotron emission and comparisons to 3D ideal MHD equilibrium. *Plasma Phys. Controlled Fusion*, 58(11):114004, 2016.

[171] R. Fischer et al. Integrated data analysis of profile diagnostics at ASDEX upgrade. *Fusion Sci. Technol.*, 58(2):675–684, 2010.

[172] A. Kallenbach et al. Electric currents in the scrape-off layer in ASDEX upgrade. *J. Nucl. Mater.*, 290-293:639–643, 2001.

[173] J. Ayllon-Guerola et al. Determination of the fast-ion phase-space coverage for the FILD spatial array of the ASDEX upgrade tokamak. *J. Instrum.*, 14(10):C10032–C10032, 2019.

[174] J. Gonzalez-Martin et al. Self-adaptive diagnostic of radial fast-ion loss measurements on the ASDEX upgrade tokamak. *Rev. Sci. Instrum.*, 92(5):053538, 2021.

[175] M. Cox. The mega amp spherical tokamak. *Fusion Eng. Des.*, 46(2):397 – 404, 1999.

[176] A. Kirk et al. Overview of recent physics results from MAST. *Nucl. Fusion*, 57(10):102007, 2017.

[177] A. Sykes et al. High-β performance of the START spherical tokamak. *Plasma Phys. Control. Fusion*, 39:B247, 1997.

[178] A. W. Morris. MAST: Results and upgrade activities. *IEEE Trans. Plasma Sci.*, 40(3):682–691, 2012.

[179] J. Milnes et al. MAST upgrade - Construction status. *Fusion Eng. Des.*, 96-97:42–47, 2015.

[180] N. Peacock et al. Measurement of the electron temperature by thomson scattering in tokamak T3. *Nature*, 224:488–490, 1969.

[181] N. J. Conway et al. High-throughput charge exchange recombination spectroscopy system on MAST. *Rev. Sci. Instrum.*, 77(10):10F131, 2006.

[182] C. A. Michael et al. Dual view FIDA measurements on MAST. *Plasma Phys. Controlled Fusion*, 55(9):095007, 2013.

[183] D. Liu et al. Compact and multi-view solid state neutral particle analyzer arrays on national spherical torus experiment-upgrade. *Rev. Sci. Instrum.*, 87(11):11D803, 2016.

[184] Culham Centre for Fusion Energy. MAST upgrade research plan. Technical report, United Kingdom Atomic Energy Authority, 2019.

[185] M. Kotschenreuther et al. The super x divertor (SXD) and a compact fusion neutron source (CFNS). *Nucl. Fusion*, 50(3):035003, 2010.

[186] D. D. Ryutov. Geometrical properties of a snowflake divertor. *Phys. Plasmas*, 14(6):064502, 2007.

[187] J. Urban et al. A survey of electron Bernstein wave heating and current drive potential for spherical tokamaks. *Nucl. Fusion*, 51(8):083050, 2011.

[188] A. Merstallinger et al. Assessment of cold welding between separable contact surfaces due to impact and fretting under vacuum. *ESA Scientific & Technical Memoranda*, 279:57, 2009.

[189] A. H. Boozer. Theory of tokamak disruptions. *Phys. Plasmas*, 19(5):058101, 2012.

[190] A. J. Theuwissen. *Solid-State Imaging with Charge-Coupled Devices*. Springer Netherlands, 1995.

[191] Characteristics and use of si APD (avalanche photodiode). Technical report, Hamamatsu.

[192] D. Dunai et al. Avalanche photodiode based detector for beam emission spectroscopy. *Rev. Sci. Instrum.*, 81(10):103503, 2010.

[193] W. J. Smith. *Modern Optical Engineering*. McGraw-Hill, 2000.

[194] M. García-Muñoz et al. Characterization of scintillator screens for suprathermal ion detection in fusion devices. *J. Instrum.*, 6(04):P04002, 2011.

[195] M. C. Jimenez-Ramos et al. Characterization of scintillator materials for fast-ion loss detectors in nuclear fusion reactors. *Nucl. Instrum. Methods Phys. Res., Sect. B*, 332:216 – 219, 2014.

[196] R. L. Boivin et al. Calibration of the TFTR lost alpha diagnostic. *Rev. Sci. Instrum.*, 63(10):4418–4426, 1992.

[197] M. Rodriguez-Ramos et al. First absolute measurements of fast-ion losses in the ASDEX upgrade tokamak. *Plasma Phys. Controlled Fusion*, 59(10):105009, 2017.

[198] J. F. Rivero-Rodriguez et al. Upgrade and absolute calibration of the JET scintillator-based fast-ion loss detector. *Rev. Sci. Instrum.*, 92(4):043553, 2021.

[199] J. X. Rossel et al. Edge-localized mode control by electron cyclotron waves in a tokamak plasma. *Nucl. Fusion*, 52(3):032004, 2012.

[200] A. Burckhart. *Different ELM regimes at ASDEX Upgrade and their linear stability analysis*. PhD thesis, Max-Planck-Institut für Plasmaphysik, 2013.

[201] A. Burckhart et al. ELM behaviour and linear MHD stability of edge ECRH heated ASDEX upgrade plasmas. *Nucl. Fusion*, 56(5):056011, 2016.

[202] E. Poli et al. TORBEAM, a beam tracing code for electron-cyclotron waves in tokamak plasmas. *Comput. Phys. Commun.*, 136(1):90–104, 2001.

[203] P. T. Lang et al. ELM pacing and high-density operation using pellet injection in the ASDEX upgrade all-metal-wall tokamak. *Nucl. Fusion*, 54(8):083009, 2014.

[204] A. Kirk et al. Recent progress in understanding the processes underlying the triggering of and energy loss associated with type I ELMs. *Nucl. Fusion*, 54(11):114012, 2014.

[205] F. M. Laggner et al. High frequency magnetic fluctuations correlated with the inter-ELM pedestal evolution in ASDEX upgrade. *Plasma Phys. Controlled Fusion*, 58(6):065005, 2016.

[206] J. Dominguez-Palacios et al. Non-linear 3D hybrid kinetic-MHD simulations of ELMs in the ASDEX upgrade tokamak with MEGA. In *16th Technical Meeting on Energetic Particles in Magnetic Confinement Systems - Theory of Plasma Instabilities*, 2019.

[207] J. Dominguez-Palacios et al. Non-linear hybrid kinetic-MHD modeling of the interaction between ELMs and fast-ions using MEGA. In *1st Spanish HPC Fusion Workshop (Online)*, 2020.

[208] M. Hoelzl et al. Simulating tokamak edge instabilities: advances and challenges. In *45th EPS Conference on Plasma Physics*, 2018.

[209] J. A. Morales et al. Edge localized mode rotation and the nonlinear dynamics of filaments. *Phys. Plasmas*, 23(4):042513, 2016.

[210] A. Cathey et al. Non-linear extended MHD simulations of type-I edge localised mode cycles in ASDEX Upgrade and their underlying triggering mechanism. *Nucl. Fusion*, 60(12):124007, 2020.

[211] M. Lakshmanan and S. Rajasekar. *Nonlinear Dynamics*. Springer, 2003.

[212] M. Sato et al. Characteristics of MHD instabilities for high beta plasmas in inward shifted LHD configurations. *Nucl. Fusion*, 57(12):126023, 2017.

[213] J. F. Rivero-Rodriguez et al. Development and installation of a scintillator based detector for fast-ion losses in the MAST-U tokamak. In *45th EPS Conference on Plasma Physics*, 2018.

[214] S. F. Smith et al. Simulations of edge localised mode instabilities in MAST-U super-X tokamak plasmas. *Nucl. Fusion*, 60(6):066021, 2020.

[215] A. J. Thornton et al. The role of ELM filaments in setting the ELM wetted area in MAST and the implications for future devices. *Plasma Phys. Controlled Fusion*, 59(1):014047, 2016.

[216] R. Ochoukov et al. High frequency Alfvén eigenmodes detected with ion-cyclotron-emission diagnostics during NBI and ICRF heated plasmas on the ASDEX upgrade tokamak. *Nucl. Fusion*, 60(12):126043, 2020.

[217] A. de Saint-Exupéry. *Le Petit Prince*. 1943.

List of Figures

List of Tables

Agradecimientos

Son muchos los momentos que se vienen a la cabeza y que uno recuerda al escribir la tesis doctoral. Después de unos años tan intensos de trabajo en este proyecto, cualquier palabra de agradecimiento se queda corta. Probablemente esté olvidando en estos agradecimientos a personas que han pasado por esta bonita etapa pero sin duda les estaré eternamente agradecido. El recuerdo de las experiencias y los viajes vividos quedarán para siempre.

Quiero empezar agradeciendo a todo el grupo de fusión de la Universidad de Sevilla. A los profesores Manuel García Muñoz y Eleonora Viezzer, por traer el sueño de la energía de fusión a la Universidad de Sevilla y por ponernos a la vanguardia de la investigación a nivel mundial. A mi director de tesis Daniel García Vallejo, cuyos consejos siempre han sido como los de un amigo con más experiencia. También agradecezco a Juanma, por confiar en mí en los primeros momentos de mi vida investigadora. Quiero agradecer con especial cariño a todos los doctorandos del grupo. Aquellos que ya estaban cuando empecé, – Joaquín, Lucía y Mauri –, que fueron un apoyo incomparable, y aquellos que se quedan ahora, – Pilar, Diego, Jesús, Pablo, José, Javi, Alessio, etc. –. Seguro que se me olvida algún nombre pero eso es prueba de que el grupo no para de crecer. Y evidentemente no se me olvida mi compañero y amigo, Javi, con el que he compartido los mejores momentos de mi doctorado. Sin él, el doctorado hubiera sido definitivamente más aburrido.

I would also like to thank the MAST-U team, my supervisor during my stays in CCFE, Ken McClements, and those involved in the design of the MAST-U FILD, Richard Martin, Dan Harvey, Dave Croft, Sarah Elmore, Andrew Thornton, among many others. I would also like to thank all my friends in Culham, Michail, James, Cindy, Giovanni and all the CCFE student community. I would like to thank the IPP staff for their help in the analysis and preparation of the AUG experiments, Andreas Burckhart, Mike Dunne, Martin Schubert, Elisabeth Wolfrum, Roman Ochoukov, among many others. I would also like to thank the MST1 scientific coordinators, Philip Schneider and Yevgen Kazakov, for their help and patience preparing and reporting the

experiments. I thank Antti for showing me that a researcher's life is much richer than simply experiments and modelling.

Finalmente agradezco a mi familia, el gran pilar de mi vida. A mi madre por su paciencia y su coraje. Ella siempre tiene un oído para escuchar a sus hijos y con eso ya se ha sacado tres ingenierías y un doctorado. A mi padre por su esfuerzo incansable. A mis hermanos Pepe y Alejandra porque han sido un ejemplo a seguir y los mejores amigos que uno puede imaginar. A mi sobrina Paula, la niña de la familia, que con cada centímetro que crece, el resto nos sentimos un poco más viejitos. Y crece mucho. A Mari Carmen, que como le dije en su boda, lleva más tiempo siendo de la familia del que puedo recordar. Y por último a Ana, "He aquí mi secreto. Es muy simple: no se ve bien sino con el corazón. Lo esencial es invisible a los ojos." [217]. Te debo la portada de mi tesis doctoral.